INVESTIGATION OF MICROFLUIDICS IN CHANNELS AND TISSUES BY FLUORESCENCE CORRELATION SPECTROSCOPY (FCS)

PAN XIAOTAO

(B.Eng., USTC, China)

A THESIS SUBMITTED FOR THE DEGREE OF

DOCTOR OF PHILOSOPHY

GRADUATE PROGRAMME IN BIOENGINEERING

NATIONAL UNIVERSITY OF SINGAPORE

JUL 2008

I would like to dedicate this thesis to my loving parents ...

Acknowledgements

This doctoral thesis would not have been possible without the help from many people whom I would like to take this opportunity to acknowledge.

I would like to acknowledge my PhD supervisor Associate Professor Thorsten Wohland from the department of Chemistry for all the help and guidance he has offered in the past few years. I am grateful for his enlightening discussion, encouragement, and patience throughout the project. His firm attitude and passion in research gave me a deep impression and will definitely have a great impact on my future career.

I would like to thank my PhD co-supervisor Associate Professor Hanry Yu from the department of Physiology who first led me into the world of microscopy. His enthusiasm for research set a good example for me.

I am grateful to my colleagues in the Wohland lab, Yu Lanlan and Hwang Ling Chin for helpful FCS discussion; Liu Ping for first FCS alignment; Guo Lin, Shi Xianke, Liu Jun, Har Jia Yi and Foo Yong Hwee for the happy times during and after office hours; Kannan Balakrishnan, Lopamudra Homchaudhuri and Manna Manoj Kumar for the opportunity to learn a different culture; Diane Sophie Morgan for collaboration in 3D microfluidic flow measurement; and Jade Aw Cai Li, Marcus Fok Han Yew, Hong Yimian and Lim Wanrong for the work during their honors projects in the lab. I also would like to acknowledge all colleagues from the Yu lab, especially Khong Yuet Mei for her guidance in the liver perfusion system and Toh Yi-Chin for providing assistance on the microchannels.

I also appreciate the joyful time when the 2003 batch of GPBE students were sitting together for lectures and seminars. I will never forget the memorable moments in Singapore with my friends Liu Ying, Chen Fenghao and He Lijuan, who are now furthering their study in the United States.

Last but not least, I would like to thank my parents for their continuous love, concern and support in the past 26 years, my elder brother for his constant sharing of personal experience in life and studies, and my elder sister for her delicious homemade dishes in the holidays.

Contents

Summary

Fluorescence correlation spectroscopy is an optical technique with single-molecule sensitivity that measures diffusion, concentration and molecular interactions. It has also been applied to microfluidic flow measurements in microchannels, plant tissues and small animals. The method uses small molecules as a probe to avoid the possible obstruction of microchannels, and it has a higher spatial resolution than all the other well-established techniques. A spatial flow profile across the dorsal aorta was characterized as a verification of FCS flow measurements with high resolution in tissues. With a custom-built fluorescence correlation microscope system, the microfluidic flows in the isolated liver, liver slice, cell-culture microchannel perfusion system were measured. Next, blood flow measurement in zebrafish embryo by FCS was demonstrated. The work of this thesis consists of the following parts:

1. A multifunctional fluorescence correlation microscope (FCM) was custom built on a commercial confocal laser scanning microscope (FV300, Olympus). In addition to the capability of confocal imaging, the system can be used to do point FCS at the exact position specified by CLSM. The function of line scan FCS was developed for the measurement of 2D flow vectors. An extra piezo scanner was designed and mounted on the mechanical stage in order to provide fast line scanning in the z axis.
2. Line scan FCS was proposed as an effective method to measure the flow velocity in 2D. Using the above custom-built FCM, point FCS and line scan FCS can be performed sequentially, and the spatial resolution was improved to 0.5 μm by extracting photon counting data in the middle portion of line scans. The flow angle was calculated with the known parameters of flow speed, line scan speed and net speed. A proof of concept of the method was done by measuring flow velocity vectors in a microchannel and a dorsal aorta of developing zebrafish embryo.
3. The application of FCS flow measurement in liver tissue engineering and zebrafish developmental biology was demonstrated. Microfluidic flow was measured in the perfused cell-culture microchannel,

perfused liver slice and isolated perfused liver. Furthermore, it was possible to characterize the spatial flow profile across a blood vessel with high resolution in zebrafish embryos. The blood flow velocity was also found to be dependent on the diameter and penetrating depth of liver sinusoids.

4. It is difficult to measure the 3D flow velocity vector in micron scale. The current available stereo particle imaging velocimetry is able to measure the flow angle in 3D but with low spatial resolution. The piezo scanner on the FCM is developed for line scan in Z axis, thus extended the line scan FCS to the third dimension for the characterization of flow velocity vectors in 3D. Its spatial resolution was still kept to $0.5\mu m$ in the 3 dimensions. The feasibility of line scan FCS for 3D microfluidic flow was verified by the measurement in a microchannel and a small blood vessel of zebrafish embryos.

List of Tables

List of Figures

Abbreviations and Symbols

Abbreviations

ACF	Autocorrelation Function
APD	Avalanche Photodiodes
CCD	Charge-Coupled Device
CCF	Cross Correlation Function
CEF	Collection Efficiency Function
CHO	Chinese Hamster Ovary
CLSM	Confocal Laser Scanning Microscope
CMOS	Complementary Metal Oxide Semiconductor
DMSO	Dimethyl Sulfoxide
DNA	Deoxyribonucleic Acid
FCCS	Fluorescence Cross Correlation Spectroscopy
FCM	Fluorescence Correlation Microscope
FCS	Fluorescence Correlation Spectroscopy
FIDA	Fluorescence Intensity Distribution Analysis
GFP	Green Fluorescent Protein
hpf	Hour Post Fertilization
ICCS	Image Cross Correlation Spectroscopy
ICS	Image Correlation Spectroscopy

LSM	Laser Scanning Microscope
MEMS	Microelectromechanical Systems
NMR	Nuclear Magnetic Resonance
OPE	One Photon Excitation
PBS	Phosphate Buffered Saline
PCH	Photon Counting Histogram
PCR	Polymerase Chain Reaction
PDMS	Polydimethylsiloxane
PIV	Particle Image Velocimetry
PMT	Photomultiplier Tube
PSF	Point Spread Function
PTV	Particle Tracking Velocimetry
RBC	Red Blood Cell
RICS	Raster Image Correlation Spectroscopy
RSD	Relative Standard Deviation
SEC	Sinusoidal Endothelial Cell
SPCM	Single Photon Counting Module
STED	Stimulated Emission Depletion
TIR	Total Internal Reflection
TMR	Tetramethylrhodamine
TPE	Two Photon Excitation
TTL	TransistorCTransistor Logic
VEGF	Vascular Endothelial Cell Growth Factor

Symbols

α	Angle between two vectors

χ^2	Chi-square test for fitting goodness
δ	Fluctuation of signals
η	Fluorescence yield of molecules
I	Laser/light intensity
κ	Detection efficiency
∇	Vector differential operator
$\vec{v}$	Fourier transform of $\vec{r}$
ω	Laser focus radius
∂	Partial differential operator
ϕ	Quantum yield
ψ	Flow angle in Z axis
$\vec{r}$	Space vector
σ	Absorption cross section of molecules
τ	Variable of time shift
θ	Flow angle in XY plane
V	Microfluidic flow speed

Chapter 1

Introduction

The studies of liquid fluid, one of the phases of matter in nature, have been numerous in the past decades. One of these studies particularly focuses on fluid flow on the microscale, which pertains to the behavior and control of microliter and nanoliter volumes of fluids both *in vitro* and *in vivo*, including the microcirculation in both artificially fabricated microchannels and animal organs.

In the past decade, great attention has been paid to micro-scale miniaturized structures in the field of chemical analysis and biological sciences, e.g. tissue engineering. The development of microfabrication technologies for lab-on-a-chip devices has allowed the application of microfluidic systems in drug testing (1), cell sorting (2), DNA characterization (3), polymerase chain reaction (4), and biochemical analysis. Microfluidic devices have superior capabilities in reagent mixing, separation, detection and sample handling compared with large-scale devices: The multiplexing of these devices facilitates simultaneous measurements of a large array of samples for drug testing or pharmaceutical analysis; the miniaturized structures only require small volume of drug, reagents or cells; furthermore, micro-scale devices can now be fabricated

at an affordable cost. Currently, microchannels incorporating microfluidics have been reported to additionally assist *in vitro* cell culture in tissue engineering (5; 6). For liver tissue engineers, primary hepatocyte *in vitro* culture models are important to understand the effects of metabolism on the new drug discovery. To preserve the physiological functions of primary hepatocytes, it is crucial to provide a 3D culture microenvironment mimicking the original physicochemical environment *in vivo*. Therefore, dedicated microfluidic channels incorporating micropillars were proposed and used for 3D perfusion culture of primary rat hepatocytes (7; 8).

To understand the performance of the above-mentioned microchips, it is necessary to measure their flow velocity patterns which helps engineers improve the fabrication process of the fluidic systems as well as to allow the evaluation of their mass transport phenomenon due to limited reaction. Furthermore, In the microfluidic cell-culture channel, the quantitative measurement of flow velocity would be an advanced parameter for people to optimize the perfusion culture system. Similarly, flow velocity is a key parameter investigated to understand the microcirculation condition in small blood vessels of animals as well. Zebrafish embryo is one of these animal models. The investigation of blood flow *in vivo* can provide information about the environment of endothelial cells (9; 10; 11), the initiation of blood microcirculation, and shear stress on the wall of blood vessels.

The zebrafish *Danio rerio* is a widely accepted animal model to study the development and function of the vascular system (12). One of the reasons that zebrafish is a popular and powerful model organism is that it shares genetic similarity to the mammals. Furthermore, the small size and optical transparency of zebrafish make it possible to do experimental analysis of vascular system at different development stages. Thus, a normal pattern of vascular anatomy of developing zebrafish is obtained

using confocal microangiography (13). This can be used as a reference to detect mutation, genetic perturbation analysis, and cross-species comparison by observing severe abnormal morphology during development. However, it is still difficult to quantify the consequent functional defects in this case, and there is no information regarding the blood flow velocity in different sizes of vessels. Therefore, a non-invasive method is then required to measure the difference of blood flow as a quantitative indicator. The same requirement applies to zebrafish liver development, the measurement of blood flow in liver sinusoids initializes a better knowledge of liver formation in zebrafish. It is reported that zebrafish embryos homozygous for the closhe (clo) mutation without endothelial cells (14; 15) and embryos without blood circulation still survive for a long period of time with a sufficient amount of oxygen from passive diffusion. Thus, zebrafish liver represents useful and unique model to study both role of endothelia and circulation during liver vasculogenesis. During the liver development, the time point when the sinusoid microcirculation is connected to the main blood circulation is still unclear. Thus the detection of blood flow velocity is a valid method to demonstrate the existence of blood circulation in liver.

Currently, there have been various approaches proposed and applied to measure the fluid flow velocity in microscale systems and small animal blood vessels in the past decade including particle image velocimetry (PIV) (16), laser speckle imaging (17), optical Doppler tomography (18), NMR imaging (19), and laser line scanning velocimetry (20; 21). However, most of them are limited in either low spatial resolution or requirement of high concentration of larger probes. For example, PIV requires the use of a sufficient number of microbeads, which might cause severe obstruction of flow and distortion of the flow profile in these micron sized structures, the situation becomes worse when coming to nanometer-scale structures. An alternative for

microfluidic flow measurements is fluorescence correlation spectroscopy (FCS) which measures the dwelling time of fluorescent molecules when passing through a confocal observation volume (22; 23). FCS can work at very low concentrations of small fluorescent molecules ($\sim 1nm$) with high spatial resolution circumventing the problems of PIV. Its experimental validation particularly in microfluidic flow was demonstrated in the transport of large protein units in plant cells (24), EYFP-bacteria flowing in a capillary (25), and DNA molecules in a microfluidic channel (3). In this thesis, FCS is extended for the measurement of flow directions in both 2D and 3D with high spatial resolution of about 0.5 μm in 3 axes. In the next chapter, the principle of FCS and its application will be discussed in details, and the experimental setup of FCS will be addressed.

Chapter 2

Fluorescence Correlation Spectroscopy

2.1 Introduction

2.1.1 Applications

Fluorescence correlation spectroscopy (FCS) was initially developed in the early 1970s for the measurement of diffusion coefficients and chemical reaction constants in solutions (22; 26). Its principle will be introduced in section 2.2. With the introduction of sensitive detectors, stable laser lines, confocal microscope schemes (27; 28), and high-speed computers, the application of FCS has been extended to a wide range of scientific questions, especially in biological sciences. It was used to measure the concentration of molecules (29), translational (22) and rotational (30; 31) diffusion, microfluidic flow (23; 32), chemical kinetics (22), molecular interactions (33; 34), conformational change (35), and lipid diffusion on membranes (36). Due to its capability to character-

ize the above parameters, FCS has a large number of applications such as drug delivery (37; 38), gene delivery (39; 40; 41; 42), biological tissue (43; 44; 45; 46), model and cell membrane dynamics (47; 48; 49), intracellular dynamics (50; 51), and molecular thermal diffusion (52; 53; 54).

2.1.2 Methodologies

Cross Correlation In addition to single focus FCS, some other methodologies based on FCS have been developed for advanced single molecule analysis. A cross correlation scheme was introduced (55) and used for flow velocity measurement by incoherent laser scattering (56; 57). By focusing two lasers with different wavelengths at the same spot, dual-color fluorescence cross correlation spectroscopy (FCCS) was proposed to detect the binding of two fluorescence-labeled molecules (58). Single wavelength excitation FCCS circumvents the need of two different laser lines and the complicated alignment and, is hence a good alternative for high order molecular interactions (59; 60). Dual-beam FCCS is another scheme for the cross correlation of two close laser foci to determine the microfluidic flow direction (61; 62).

Two-Photon Excitation Two-photon fluorescence microscopy (63) has the inherent capability of 3D discrimination by laser excitation that is limited at the focus. With the advantage of less laser scattering, reduced photodamage, and relatively low autofluorescence, two-photon excitation facilitates the applications of FCS into biological systems (50; 64) especially thick tissues. Furthermore, two-photon techniques provide a wide excitation spectrum and a large emission separation thus it can be incorporated with FCCS using a single laser line to study molecular complex formation (65; 66).

TIR-FCS Other optical imaging schemes were incorporated into the FCS setup. Total internal reflection (TIR) fluorescence microscopy is a technique able to illuminate a thin layer (~ 100nm) near a glass surface, and it is widely used for membrane surface imaging in cell biology. Therefore, the combination of TIR and FCS was proposed to measure the membrane surface dynamics including diffusion, local concentration, and binding rate (67; 68).

Scanning FCS Since traditional point FCS is more suitable for fast-diffusing molecules, in case of slow-diffusing or immobile molecules, scanning FCS was proposed in order to avoid photobleaching due to the long dwelling time of fluorescent molecules in the focal volume. This technique was initially used for protein aggregation on cell membranes (69; 70), and was extended later for other applications including slow-diffusing molecules (71; 72), protein-membrane interaction (73) and flow direction by circular scan (74), slow membrane dynamics (75) and flow direction by line scan (46).

ICS Image (cross) correlation spectroscopy (ICS or ICCS) is an extension of scanning FCS which describes a spatial autocorrelation function of pixel intensities from a microscope image using a 2D Fourier transform algorithm (76; 77). ICS can be used to extract information about the number and size of protein aggregates with very slow dynamics. This method has been further extended to temporal image stack analysis (78) for diffusion and flow velocity, and the improvement of its temporal resolution gives rise to the invention of raster image correlation spectroscopy (RICS) (79).

PCH Photon counting histogram (PCH), also known as fluorescence intensity distribution analysis (FIDA) is a complementary method to FCS used for molecular brightness analysis (80; 81). The data of individual photon arrival time obtained for FCS

can be used as well for PCH by calculating a histogram of emission photon counts in a given period of time. The method is helpful in distinguishing these molecules with similar structures and molecular weight according to their brightness, which is independent of the molecular concentration. Dual-color PCH provides further discrimination of species by color differences (82).

2.1.3 Instrumentation

FCS was initially performed on a traditional fluorescence microscope setup without a pinhole until the confocal scheme was introduced to improve the signal-to-noise ratio (27; 28). To create a sub-diffraction-limited volume, TIR excitation was adapted to FCS (67) for the confinement in Z direction and the volume dimension could be further reduced in XY plane by a zero-mode waveguides (83). Another scheme for this purpose is stimulated emission depletion (STED) which was demonstrated to have fivefold decrease of the detection volume (84). Conventional FCS has a single focus which provides high spatial resolution but lacks the measurement efficiency over a large image area. Simultaneous two-foci excitation (62) is one of the solutions for FCS and FCCS, which is improved by a four-foci scheme using a diffractive optical fan-out element (85).

Regarding the detectors for emission light, an optical fiber array is capable of multicolor detection (60; 86) by a diffraction prism or gratings. However, in this configuration a single photon counting avalanche photodiodes (APD) was still required. Recently, a complementary metal oxide semiconductor (CMOS) single photon 2×2 detector array was used to measure four points simultaneously by using a diffractive optical element to achieve multifocal excitation (87), and its performance is compa-

rable to that of APD. Alternatively, novel CCD cameras that are sufficiently fast and sensitive are used for temporal FCS analysis, such as determination of diffusion coefficient of molecules in viscous solution and proteins on cell membrane, and microfluidic flow velocity using single focus excitation (88). Two-foci FCS by a CCD camera was also capable of multiplex FCS measurements (88; 89). Due to the imaging ability of a CCD camera, it is possible to map a large number of measurement points to the image area. Spinning disk FCS (90) and CCD based TIR-FCS (91) have been demonstrated to measure FCS parameters at many image pixels simultaneously. The confocal and TIR setups reduce cross-talk phenomenon among the neighboring pixels.

2.2 Theory and Setup

2.2.1 Focal Volume

In a typical confocal microscope setup, a laser beam is focused by an infinity-corrected objective into a diffraction-limited spot, and the spatial power distribution of the focused laser beam $I_{ex}(\vec{r})$ has a Gaussian-Gaussian-Lorentzian profile with a maximum amplitude I_0. The emitted fluorescence light is collected by the same objective and out-of-focus light is rejected by a pinhole in the image plane. In this case, a small observation focal volume is realized by the confocal detection of the objective-pinhole combination. A term, collection efficiency function (CEF), is thus introduced to describe its inherent spatial collection efficiency (28).

$$CEF(r',z) = \frac{1}{\Delta}\int T(r)PSF(r,r',z)dr \tag{2.1}$$

A cylindrical coordinate system is applied as the image plane is the XY plane and the optical axis is the Z axis. Where Δ is a normalization factor, $T(r)$ is the transmission function of the pinhole, and $PSF(r, r', z)$ is the point spread function of the microscope that describes the response of the optical imaging system to a point source located at position (r', z). Therefore, the convolution of $I_{ex}(\vec{r})$ and $CEF(\vec{r})$ gives a dimensionless function $W(\vec{r})$ which represents the optical distribution of emitted light from the focal volume. This can be approximated by a 3D Gaussian profile with a lateral waist r_0 and an axial height z_0 where $W(\vec{r})$ decreases by a factor of e^{-2} compared to the central maximum amplitude.

$$\begin{aligned} W(\vec{r}) &= I_{ex}(\vec{r}) * CEF(\vec{r}) \\ &= I_0\, e^{-2\frac{x^2+y^2}{r_0^2}}\, e^{-2\frac{z^2}{z_0^2}} \end{aligned} \tag{2.2}$$

When fluorophores pass through the focal volume $W(\vec{r})$, the molecules will be excited from the ground state to the excited state by the focused laser. The emitted fluorescence $F(t)$ due to the relaxation process from the excited state to the ground state can be written as

$$F(t) = \eta \int W(\vec{r}) C(\vec{r}, t) d\vec{r} \tag{2.3}$$

where the integration is taken over the 3D space of laser focal volume. Here the symbol η represents the fluorescence yield that characterizes the detected photon count rate per molecule, it is directly related to the absorption cross section σ, the quantum yield ϕ of a particular fluorophore, and the detection efficiency κ of the optical system. Briefly the expression can be written as: $\eta = \sigma \cdot \phi \cdot \kappa$. In the equation 2.3 we make the assumption that the fluorescence yield η of a fluorophore is constant and independent on

the position $\vec{r}$ and time t, while the local concentration of molecules $C(\vec{r},t)$ varies with position and time. The fluorescence fluctuation $\delta F(t)$ is defined as the deviation of fluorescence signal from its temporal average. Assuming that the excitation laser power I_0 and the emitted light distribution $W(\vec{r})$ do not change during the measurement time, the fluctuations $\delta F(t)$ from the molecules are only caused by the local concentration variation $\delta C(\vec{r},t)$ in the focal volume, which could be due to the dynamic motion of molecules through or within the volume.

$$\begin{aligned} \delta F(t) &= F(t) - \langle F(t) \rangle \\ &= \eta \int W(\vec{r})\, \delta C(\vec{r},t) d\vec{r} \end{aligned} \tag{2.4}$$

2.2.2 Autocorrelation Analysis

The fluorescence fluctuation $\delta F(t)$ can be used to characterize the dynamics of single molecule in the focal volume, e.g. the diffusion by Brownian motion. The width of each fluctuation in this case contains the information regarding the molecular dwelling time, a measurement of the fluctuation widths and their averaging directly gives the dynamics of molecules. However, this method has to scan through all the fluctuations in the time domain and thus is quite time-consuming. A mathematical analysis called autocorrelation is then introduced as a fast and robust algorithm, which is a measure of how a time-domain signal fits with its time-shifted version, as a function of the time shift τ. Normally the autocorrelation function of $f(t)$ is defined as

$$R_f(\tau) \equiv \lim_{T\to\infty} \frac{1}{2T} \int_{-T}^{T} f(t) f(t+\tau) dt \tag{2.5}$$

In the case of fluorescence $F(t)$, it can be considered as unchanged when the molecules stay in the focal volume, although the 3D Gaussian profile of $W(\vec{r})$ should be taken into account for the derivation of theoretical models. Therefore, the autocorrelation analysis is suitable to extract the characterization time of single fluorescent molecule dynamics. Substituting $F(t)$ into the equation 2.5, an autocorrelation function of $F(t)$ can be obtained as

$$\begin{aligned} R_F(\tau) &= \lim_{T\to\infty} \frac{1}{2T} \int_{-T}^{T} F(t)F(t+\tau)dt \\ &= \Big\langle F(t)F(t+\tau) \Big\rangle \end{aligned} \tag{2.6}$$

where $\langle\rangle$ is the operator of time averaging. Typically, the autocorrelation function is normalized over the square of average intensity, which gives a normalized autocorrelation function (ACF) of $F(t)$ as expressed below

$$\begin{aligned} G(\tau) &= \frac{\Big\langle F(t)F(t+\tau) \Big\rangle}{\Big\langle F(t) \Big\rangle^2} \\ &= \frac{\Big\langle \Big[\Big\langle F(t) \Big\rangle \delta F(t+\tau) + \Big\langle F(t+\tau) \Big\rangle \delta F(t) \Big] \Big\rangle}{\Big\langle F(t) \Big\rangle^2} \\ &\quad + \frac{\Big\langle \Big[\Big\langle F(t) \Big\rangle \Big\langle F(t+\tau) \Big\rangle + \delta F(t) \delta F(t+\tau) \Big] \Big\rangle}{\Big\langle F(t) \Big\rangle^2} \\ &= \frac{\Big\langle \delta F(t)\, \delta F(t+\tau) \Big\rangle}{\Big\langle F(t) \Big\rangle^2} + 1 \end{aligned} \tag{2.7}$$

with

$$\Big\langle \delta F(t) \Big\rangle = 0 \tag{2.8}$$

Substituting the equation 2.4 into 2.7 it gives

$$G(\tau) = \frac{\iint W(\vec{r})W(\vec{r}\,')\left\langle \delta C(\vec{r},t)\,\delta C(\vec{r}\,',t+\tau)\right\rangle d\vec{r}d\vec{r}'}{\left[\int W(\vec{r})\left\langle C(\vec{r},t)\right\rangle d\vec{r}\right]^2} + 1 \tag{2.9}$$

In order to calculate the integral, the factor related to δC has to be solved first as follows. We make a concentration correlation function

$$\begin{aligned} g(\vec{r},\vec{r}\,',\tau) &= \left\langle \delta C(\vec{r},t)\delta C(\vec{r}\,',t+\tau)\right\rangle \\ &= \left\langle \delta C(\vec{r},0)\delta C(\vec{r}\,',\tau)\right\rangle \end{aligned} \tag{2.10}$$

In the case that all the molecules are separate and independent, the correlation is with a maximum amplitude at the time ($\tau = 0$) and without position shift ($\vec{r} = \vec{r}\,'$). It can be written as

$$g(\vec{r},\vec{r}\,',0) = \langle C\rangle\,\delta(\vec{r}-\vec{r}\,') \tag{2.11}$$

here the correlation function is the product of a Dirac delta function and the mean square fluctuation $\langle C\rangle$ based on Poisson statistics. When only diffusion occurs in an open volume, the local concentration changes with respect to time. Assuming the diffusion coefficient D is a constant, the diffusion equation based on Fick's second law is derived as

$$\frac{\partial\,\delta C(\vec{r},t)}{\partial t} = D\,\nabla^2\delta C(\vec{r},t) \tag{2.12}$$

taking the Fourier transform on both sides of the equation, it gives

$$\frac{\partial\,\tilde{C}(\vec{\nu},t)}{\partial t} = -D\,\nu^2\tilde{C}(\vec{\nu},t) \tag{2.13}$$

where $\tilde{C}$ is the Fourier transform of δC. Here F is the symbol for Fourier transform, and F^{-1} represents the inverse Fourier transform.

$$\tilde{C}(\vec{\nu}, t) = F_{\nu}\left[\,\delta C(\vec{r}, t)\,\right] \tag{2.14}$$

the solution for the equation 2.13 is

$$\tilde{C}(\vec{\nu}, t) = \tilde{C}(\vec{\nu}, 0)e^{-D\nu^2 t} \tag{2.15}$$

the substitution of the equation 2.15 into the equation 2.10 produces the solution for concentration correlation function

$$\begin{aligned}
g(\vec{r}, \vec{r}\,', \tau) &= \left\langle \delta C(\vec{r}, 0)\delta C(\vec{r}\,', \tau)\right\rangle = \left\langle \delta C(\vec{r}, 0)\, F^{-1}_{\vec{r}\,'}[\tilde{C}(\vec{\nu}, \tau)]\right\rangle \\
&= F^{-1}_{\vec{r}\,'}\left[\left\langle \delta C(\vec{r}, 0)\, \tilde{C}(\vec{\nu}, 0)e^{-D\nu^2\tau}\right\rangle\right] \\
&= F^{-1}_{\vec{r}\,'}\left[F_{\nu}\left[\left\langle \delta C(\vec{r}, 0)\delta C(\vec{r}\,', 0)\right\rangle\right] e^{-D\nu^2\tau}\right] \\
&= F^{-1}_{\vec{r}\,'}\left[F_{\nu}\left[\langle C\rangle \delta(\vec{r} - \vec{r}\,')\right] e^{-D\nu^2\tau}\right] \\
&= F^{-1}_{\vec{r}\,'}\left[\langle C\rangle e^{i\vec{\nu}\vec{r}\,'} e^{-D\nu^2\tau}\right] \\
&= \langle C\rangle \left(\frac{1}{2\sqrt{\pi D\tau}}\right)^3 e^{-\frac{(\vec{r}-\vec{r}\,')^2}{4D\tau}} \\
\because \quad F^{-1}_{\vec{r}\,'}\left[e^{-a\nu^2}\right] &= \frac{1}{2\pi}\sqrt{\frac{\pi}{a}}\, e^{-\vec{r}\,'^2/4a}
\end{aligned} \tag{2.16}$$

Inserting the equation 2.16 into the equation 2.9, the analytical solution of $G(\tau)$ for 3D diffusion is obtained

$$G(\tau) = \frac{\iint W(\vec{r})W(\vec{r}\,')g(\vec{r}, \vec{r}\,', \tau)\, d\vec{r}d\vec{r}\,'}{\left[\langle C\rangle \int W(\vec{r})\, d\vec{r}\right]^2} + 1$$

$$
\begin{aligned}
&= \frac{1}{\langle C\rangle (4\pi D\tau)^{\frac{3}{2}}} \frac{\iint W(\vec{r})W(\vec{r}\,')\, e^{-\frac{(\vec{r}-\vec{r}\,')^2}{4D\tau}} d\vec{r}\, d\vec{r}\,'}{\left[\langle C\rangle \int W(\vec{r})\, d\vec{r}\right]^2} + 1 \\
&= \frac{1}{\langle C\rangle (4\pi D\tau)^{\frac{3}{2}}} \frac{\frac{\pi\sqrt{D\tau}\, r_0}{\sqrt{1+\frac{4D\tau}{r_0^2}}} \frac{\pi\sqrt{D\tau}\, r_0}{\sqrt{1+\frac{4D\tau}{r_0^2}}} \frac{\pi\sqrt{D\tau}\, z_0}{\sqrt{1+\frac{4D\tau}{z_0^2}}}}{(r_0^4 z_0^3 \pi^3)/8} + 1 \\
&= \frac{1}{\langle C\rangle \pi^{\frac{3}{2}} r_0^2 z_0} \frac{1}{\sqrt{1+\frac{4D\tau}{r_0^2}}} \frac{1}{\sqrt{1+\frac{4D\tau}{r_0^2}}} \frac{1}{\sqrt{1+\frac{4D\tau}{z_0^2}}} + 1 \\
&= \frac{1}{\langle C\rangle \mathrm{V_{eff}}} \frac{1}{1+\frac{\tau}{\tau_d}} \frac{1}{\sqrt{1+\left(\frac{r_0}{z_0}\right)^2 \frac{\tau}{\tau_d}}} + 1
\end{aligned}
\tag{2.17}
$$

Here $\mathrm{V_{eff}} = \pi^{\frac{3}{2}} r_0^2 z_0$ is the effective focal volume for fluorescence detection, while $\mathrm{N} = \mathrm{V_{eff}}\langle C\rangle$ is the average number of molecules staying in the volume. The diffusion time τ_d of molecules through the focal volume is defined as, $\tau_d = r_0^2/(4D)$. r_0 and z_0 are defined in the equation 2.2. There are some common integrals used in the above derivation as listed below.

$$
\begin{aligned}
\int e^{-x^2} dx &= \sqrt{\pi} \\
\iint e^{-a(x^2+bxy+y^2)}\, dxdy &= \frac{\pi}{a\sqrt{1-b^2/4}} \\
\iint e^{-\frac{2x^2}{r_0^2}} e^{-\frac{2x'^2}{r_0^2}} e^{-\frac{(x-x')^2}{4D\tau}} dxdx &= \iint e^{-\left(\frac{2}{r_0^2}+\frac{1}{4D\tau}\right)\left(x^2 - \frac{\frac{1}{2D\tau}}{\frac{2}{r_0^2}+\frac{1}{4D\tau}} xx' + x'^2\right)} dxdx' = \frac{\pi\sqrt{D\tau}\, r_0}{\sqrt{1+\frac{4D\tau}{r_0^2}}} \\
\iint e^{-\frac{2y^2}{r_0^2}} e^{-\frac{2y'^2}{r_0^2}} e^{-\frac{(y-y')^2}{4D\tau}} dydy' &= \frac{\pi\sqrt{D\tau}\, r_0}{\sqrt{1+\frac{4D\tau}{r_0^2}}} \\
\iint e^{-\frac{2z^2}{r_0^2}} e^{-\frac{2z'^2}{r_0^2}} e^{-\frac{(z-z')^2}{4D\tau}} dzdz' &= \frac{\pi\sqrt{D\tau}\, z_0}{\sqrt{1+\frac{4D\tau}{z_0^2}}}
\end{aligned}
$$

In the equation 2.3 the assumption of the unchanged fluorescence property η of a particular fluorophore may not be true because during the fluorescence process of electron relaxation from the excited state to the ground state, the electron could undergo an intersystem crossing to a triplet state. The transition from the triplet state to ground state is quantum mechanically "forbidden" but still occurs at a slower time scale (μs) compared with that of fluorescence lifetime (ns). However, one still can consider this phenomenon as an independent event which is coupled to the molecular kinetic. So the ACF with triplet state can be written as (92)

$$G_{\text{total}}(\tau) = g_{\text{t}}(\tau) \cdot G(\tau) \tag{2.18}$$

with

$$g_{\text{t}}(\tau) = \frac{F_{\text{trip}}}{1 - F_{\text{trip}}} \exp\left(-\frac{\tau}{\tau_{\text{trip}}}\right) + 1 \tag{2.19}$$

where τ_{trip} is the relaxation time from triplet state; and F_{trip} is the number fraction of molecules in the triplet state. Therefore, the ACF for 3D diffusing single particle (equation 2.17) can be modified as

$$G(\tau) = g_{\text{t}}(\tau)\frac{1}{N}\frac{1}{1 + \frac{\tau}{\tau_{\text{d}}}}\frac{1}{\sqrt{1 + \frac{\tau}{K^2\tau_{\text{d}}}}} + 1 \tag{2.20}$$

where $K = z_0/r_0$ is the structural factor characterized by the optical system setup and alignment.

2.2.3 Microfluidic Flow

When there is active transport such as laminar flow present in the dynamic system, the diffusion equation 2.12 is not only dominated by thermal kinetics but also the transport velocity V_f

$$\frac{\partial\,\delta C(\vec{r},t)}{\partial t} = D\,\nabla^2\delta C(\vec{r},t) - \vec{V}\cdot\nabla\delta C(\vec{r},t) \tag{2.21}$$

and its Fourier transform

$$\frac{\partial\,\tilde{C}(\vec{\nu},t)}{\partial t} = -D\,\nu^2\tilde{C}(\vec{\nu},t) - i\nu\vec{V}\cdot\tilde{C}(\vec{\nu},t) \tag{2.22}$$

to solve the partial differential equation

$$\tilde{C}(\vec{\nu},t) = \tilde{C}(\vec{\nu},0)e^{-\left(D\nu^2+i\vec{\nu}\vec{V}\right)t} \tag{2.23}$$

consequently, the concentration correlation function is calculated as

$$g_f(\vec{r},\vec{r}',\tau) = \langle C\rangle\left(\frac{1}{2\sqrt{\pi D\tau}}\right)^3 e^{-\frac{(\vec{r}'-\vec{r}+\vec{V}\tau)^2}{4D\tau}} \tag{2.24}$$

making the assumption that the laminar flow is limited in a plane perpendicular to the optical axis and its direction is along the x axis, i.e. $\vec{V} = V_x\hat{x}$. Therefore, the substitution of the above equation to 2.9 gives

$$\begin{aligned} G_f(\tau) &= \frac{1}{\langle C\rangle(4\pi D\tau)^{\frac{3}{2}}}\frac{\iint W(\vec{r})W(\vec{r}')\,e^{-\frac{(\vec{r}-\vec{r}'-\vec{V}\tau)^2}{4D\tau}}d\vec{r}d\vec{r}'}{\left[\langle C\rangle\int W(\vec{r})\,d\vec{r}\right]^2} + 1 \\ &= \frac{1}{\langle C\rangle V_{\text{eff}}}\frac{1}{\sqrt{1+\frac{4D\tau}{r_0^2}}}e^{-\frac{\left(\frac{\tau}{r_0/V_x}\right)^2}{1+\frac{4D\tau}{r_0^2}}}\frac{1}{\sqrt{1+\frac{4D\tau}{r_0^2}}}\frac{1}{\sqrt{1+\frac{4D\tau}{z_0^2}}} + 1 \end{aligned}$$

$$= \frac{1}{\langle C \rangle V_{\text{eff}}} \frac{1}{1+\frac{\tau}{\tau_d}} \frac{1}{\sqrt{1+\left(\frac{r_0}{z_0}\right)^2 \frac{\tau}{\tau_d}}} e^{-\frac{\left(\frac{\tau}{\tau_f}\right)^2}{1+\frac{\tau}{\tau_d}}} + 1 \tag{2.25}$$

here $\tau_f = r_0/V_x$ is the flowing time for the molecules through the focal volume. As seen, the flow ACF can be developed from the diffusion ACF by coupling an exponential term. Considering the triplet effect, the ACF for flow can be finally written as

$$G_f(\tau) = g_t(\tau) \frac{1}{N} \frac{1}{1+\frac{\tau}{\tau_d}} \frac{1}{\sqrt{1+\frac{\tau}{K^2 \tau_d}}} \exp\left[-\left(\frac{\tau}{\tau_f}\right)^2 \frac{1}{1+\frac{\tau}{\tau_d}} \right] + 1 \tag{2.26}$$

2.2.4 Cross Correlation

Cross correlation is a term used to describe the similarity of two signals, in this case, the autocorrelation of a signal is actually a measure of cross correlation with itself.

$$C_{fg}(\tau) \equiv \lim_{T \to \infty} \frac{1}{2T} \int_{-T}^{T} f(t) g(t+\tau) dt \tag{2.27}$$

In experiments, the similarity of detected fluorescence from two different kinds of molecules in the focal volume implies the close relation of the two which could be binding, aggregation or interaction. The cross correlation function (CCF) for two fluorescence signals is defined as

$$G_x(\tau) = \frac{\left\langle F_1(t) F_2(t+\tau) \right\rangle}{\left\langle F_1(t) \right\rangle \left\langle F_2(t) \right\rangle} \tag{2.28}$$

where $F_1(t)$ and $F_2(t)$ are the fluorescence intensities from channel 1 and 2, which could originate from the same focal volume but with different colors or from two nearby foci with the same color.

2.2.5 Two-Photon Excitation

Two-photon excitation (TPE) is a process in which two photons of near-infrared light (e.g. 800nm) are simultaneously ($\sim 10^{-15}s$) absorbed by a fluorescent molecule that is promoted to an excited state and then emits a single photon. In a simplified term, the resultant fluorescence emission is similar to that by one-photon excitation (OPE) process when the molecules are excited by a single photon (e.g. 400nm). As noted, the wavelength required in TPE is almost twice that used in OPE. The excitation probability of molecules by TPE depends on the square of the exciting laser intensity, while that of molecules by OPE is linear with the excitation light. The same principle applies to emission fluorescence intensity, when referring to the equation 2.2 and equation 2.3, we have the following relationship. For OPE,

$$F(t) \propto W(\vec{r}) \tag{2.29}$$

for TPE, we have

$$F(t) \propto W^2(\vec{r}) \tag{2.30}$$

The fact that the probability of TPE drops off dramatically from the focal point enables a tiny three-dimensionally excited sample volume. Therefore, the TPE setup eliminates the introduction of a pinhole which is required in a typical confocal microscopy configuration. TPE laser scanning fluorescence microscopy (63) has been demonstrated to be a powerful and promising research tool for living cells and tissues with the advantages of reduced light scattering, reduced autofluorescence and photobleaching. Furthermore, the development of FCS benefits from TPE technology, TPE-FCS has been shown to measure molecular dynamics in living cells and can substantially im-

prove signal-to-noise level in deep tissues (50). The autocorrelation function (ACF) for TPE is similar to that for OPE, when introducing the relationship 2.30 to the equation 2.17, we can obtain the same ACF as shown in the last line of equation 2.17, but the diffusion time τ_d of molecules through the focal volume is defined as,

$$\tau_d = \frac{r_0^2}{8D} \tag{2.31}$$

As noted, the difference between OPE and TPE is due to a squared Gaussian distribution of $W(\vec{r})$. Therefore, we can use the same fitting model for TPE FCS measurements.

2.2.6 Typical FCS Setup

The confocal scheme was introduced to FCS in the 1990s to increase the signal-to-noise ratio of the optical system. Confocal means ”having the same foci”. In the microscope, the field diaphragm in front of the light source, the specimen plane, and the detector image plane are optically conjugated planes, which means any light in one conjugated image plane will be projected to the next plane. With an infinity-corrected objective, a parallel laser beam is focused into an illumination point, and a pinhole in the detector image plane is used to reject out-of-focus light. The two foci, the laser focus and the pinhole, are also optically conjugated. In other words, the signal (image) from the laser focus is projected to the pinhole position, and the superimposition of laser focus and pinhole is then projected to the detector. In this case only the signal passing through the pinhole can be detected by the detector.

In the experimental realization (Fig. 2.1), an Argon air or HeNe laser beam with a $1/e^2$ diameter about 1 μm is resized by a beam expander by a factor of 4 and reflected by a long pass dichroic mirror into the back aperture of an high NA objective which

the laser beam overfills, e.g. Zeiss C-Apochromat 63x/1.20 W Korr, C-Apochromat 40x/1.20 W Korr or Olympus UPLSAPO 60x/1.2 W. The fluorescence light from the focal point (width: $0.2 - 0.3\mu m$; height: $1.0 - 1.5\mu m$) is collected by the same objective and refocused by a tube lens ($f = 164.5mm$). Only the in-focus light, passing through a pinhole (diameter $50\mu m$), can be monitored by the sensitive detector working in single-photon-counting mode, such as an avalanche photodiode (APD) or photomultiplier tube (PMT). An imaging lens ($f = 60mm$) is used to align the projection of the pinhole into the detector active area (diameter $175\mu m$ for the APD). The correlation function is processed by online correlator using the intensity signal from the detector. FCS is a technique based on the detection of fluorescence signal in a single spot. The intensity measurement does not provide any information on either the location of measurement point or the morphology of object to be investigated. Therefore, almost all the commercial FCS products are provided with the capability of microscopic imaging. Since FCS uses the same confocal optical scheme as laser scanning microscope (LSM), in most cases, the commercial FCS product can perform both confocal imaging and FCS measurements. In the next chapter, a custom-built microscope system is described and its flexibility as an advantage for advanced FCS technique development is discussed.

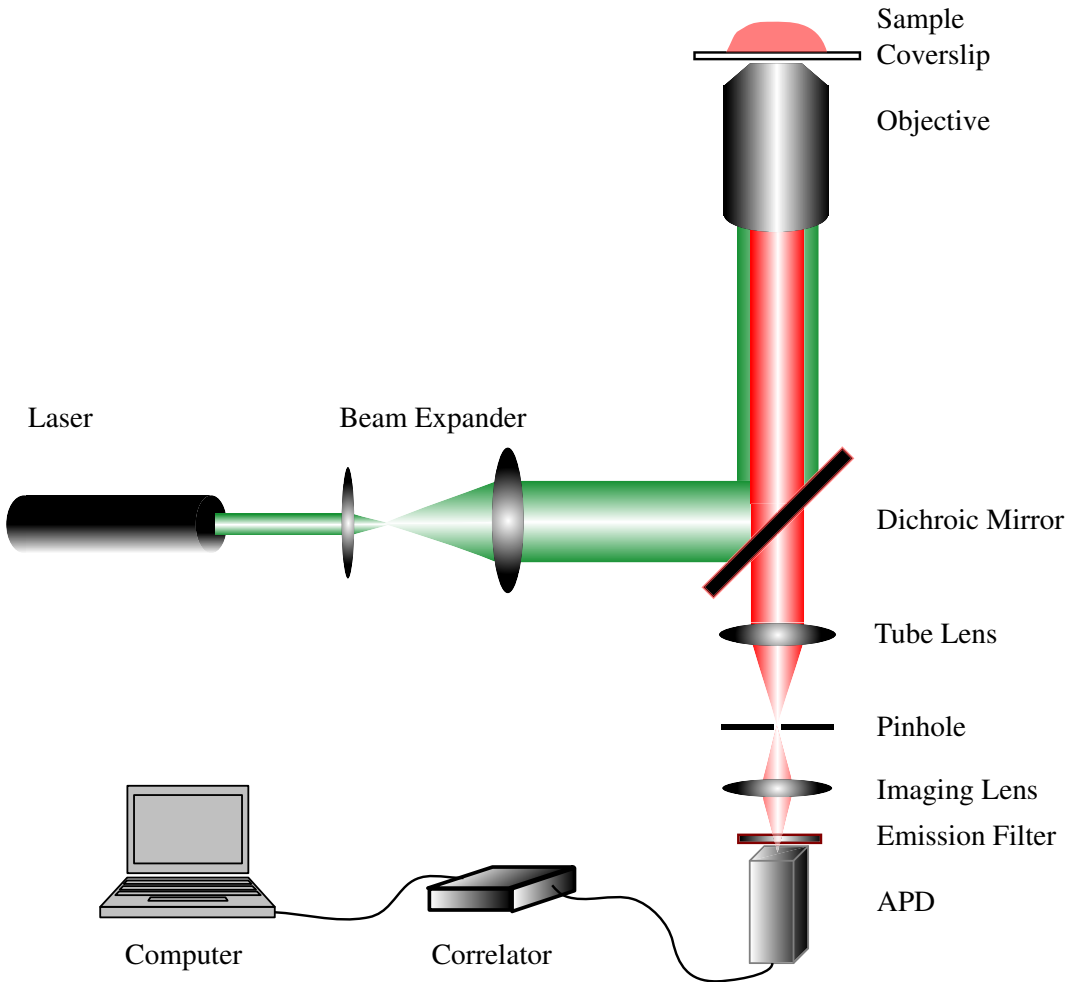

Figure 2.1: A typical setup for fluorescence correlation spectroscopy. The diagram is described in details in the text.

Chapter 3

Multifunctional Fluorescence Correlation Microscopy

3.1 Introduction

Due to its principle and the shape of focal volume, FCS is only able to do point measurement at any desired location by manual movement of the sample. However, biological systems are inherently heterogenous in terms of molecular interaction conditions in either the cytoplasm or the plasma membrane. Fluorescence correlation microscopy (FCM), a technique term first introduced in 1995 by Terry and coworkers (93) which combines imaging techniques with FCS, identified points of interest within a sample and subsequently positioned FCS observation volume and measurement at these points (94). A CCD camera was used to guide the precise FCS positioning in the intracellular environment. However, the optical pathways of imaging and FCS in this case were different and had to be properly aligned. Another imaging tool is the confocal laser scanning microscope (CLSM) which is now a routine instrument for biologists to

obtain high resolution fluorescence images and sequentially reconstruct the 3D structure of specimens. The direct combination of CLSM and FCS resulted in a number of commercial systems in the market (95) and was also used for real-time FCS position readout (96). However, most instruments use separate pinholes for CLSM and FCS which makes it difficult to align and overlay the two focal volumes in three dimensions. In this work, I built a custom combination system, i.e. FCM using a single pinhole (97) to ensure the accurate 3D positioning of the FCS observation volume. The single pinhole scheme is used as well in both the Leica TCS SP2 AOBS FCS microscope system and the new Zeiss LSM710 ConfoCor3. However, the setup of FCM described in this chapter can be achieved by simple modifications on a commercial CLSM instrument (FV300, Olympus).

The presented FCM system has the capability to position the FCS observation volume at any point within the field of view and allows scanning of the laser beam during FCS acquisition to perform, for instance, flow profile measurements. Equipped with two single-photon-counting modules (SPCM), rotational FCS (98) and single wavelength dual color fluorescence cross correlation spectroscopy (SW-FCCS) (59; 60) can be conducted to determine protein dynamics and molecular interactions. The use of two SPCMs in combination with a 50:50 non-polarizing beamsplitter allows the cross correlation measurement of SPCM signals eliminating the effect of afterpulsing and detector deadtime (99). This makes the time range of 1-100 ns accessible (100) and allows the measurement of rotational diffusion times. Furthermore, spatial FCCS can be realized using the same optical scheme by an opposite lateral shift of the two SPCM detection sensitive elements thus detecting different regions of the same pinhole. This single pinhole spatial FCCS is an alternative technique to characterize the flow profile

in microstructures compared to dual beam spatial FCCS (62). With the help of built-in scanner mirrors, scanning FCS can be realized on the instrument by performing line scans. The method is described later in chapter 4 to determine flow directions in both microchannels and small blood vessels. In the following section, the performance of the FCM system is characterized and several applications are shown including rotational and translational diffusion measurements of proteins in live cells, determination of translational diffusion on upper and lower membranes of CHO cells, and two-photon excitation FCS.

3.2 Materials and Methods

3.2.1 Theory

FCS is a sensitive tool used to measure the characteristic time of dynamic processes such as diffusion, flow and molecular binding which cause the temporal intensity fluctuations in a small volume defined by a high NA objective and a pinhole. The detailed derivation of the ACF can be found in chapter 2. The ACF for 3D diffusing single particle and microfluidic flow is described by equation 2.20 and 2.26 respectively. When the diffusion of molecules is restricted to 2D which is usually the case for transmembrane protein dynamics, the ACF can be modified as

$$G_{2D}(\tau) = g_t(\tau)\frac{1}{N}\frac{1}{1+\frac{\tau}{\tau_d}} + 1 \tag{3.1}$$

Additionally, rotational diffusion of these proteins in the plasma membrane can be characterized by the following model (30; 101)

$$G_{2Dr}(\tau) = g_r(\tau)\, g_t(\tau)\frac{1}{N}\frac{1}{1+\frac{\tau}{\tau_d}} + 1 \tag{3.2}$$

$$g_r(\tau) = \frac{F_{rot}}{1-F_{rot}}\exp\left(-\frac{\tau}{\tau_{rot}}\right) + 1$$

τ_{rot}: rotational time; F_{rot}: fraction of molecules in the rotational status. Dual color single beam fluorescence cross correlation analysis is widely used for molecular binding measurements (58; 59), especially for the two proteins with similar diffusion coefficient (34). The amplitude of CCF is inversely proportional to the number of binding complexes.

$$G_x(\tau) = G_x(0)\frac{1}{1+\frac{\tau}{\tau_d}}\frac{1}{\sqrt{1+\frac{\tau}{K^2\tau_d}}} + 1 \tag{3.3}$$

$$G_x(0) = \frac{\langle C_{12}\rangle}{V_{eff}\left(\langle C_1\rangle + \langle C_{12}\rangle\right)\left(\langle C_2\rangle + \langle C_{12}\rangle\right)}$$

There is also a spatial cross correlation analysis known as single color dual beam FCCS developed for the characterization of microfluidic flow profiles (62). The CCF in this case is calculated on the intensities from two spatially separate observation volumes and can be written as

$$G_{xf}(\tau) = \frac{1}{N}\frac{1}{1+\frac{\tau}{\tau_d}}\frac{1}{\sqrt{1+\frac{\tau}{K^2\tau_d}}}\exp\left[-R^2\left(\frac{\tau^2+\tau_{xf}^2-2\,\tau\,\tau_{xf}\cos(\alpha)}{\tau_{xf}^2}\right)\frac{1}{1+\frac{\tau}{\tau_d}}\right] \tag{3.4}$$

with the assumption that there is no flow in Z direction. R: length ratio of distance between the centers of two detection volumes over the radius of one focal volume;

τ_{xf}: flowing time of molecules from one focus to the other in the XY plane; α: angle between the flow axis and the connecting line of two foci. Furthermore, for the proposed single pinhole spatial FCCS, pure cross correlation functions for microfluidic flow were calculated as the difference of the backward and forward CCFs, where the forward CCF is the cross correlation in the flow direction and the backward CCF represents the cross correlation in the opposite direction. The two halves of the detection volume defined by two detectors are close to each other, therefore, there is a high probability that the photons from one half will be detected by the other detector thus a pseudoautocorrelation is present (62), but it can be eliminated by subtracting the backward CCF from the forward CCF. The detailed description about single pinhole spatial FCCS can be found in section 3.3.3.

3.2.2 Optical Setup

The FCM was composed of a CLSM (FV300, Olympus, Singapore) and a custom-built FCS detection module on top of the scanning unit (Fig. 3.1), all technical drawings and mounting distances are shown in Appendix A. The laser beam from an air-cooled Argon ion laser (488nm) or a Helium Neon laser (543nm and 633nm, Melles Griot) going through a linear polarizer was reflected by a long pass excitation dichroic mirror (488/543/633) and delivered into the scanning mirrors (G120DT, GSI Lumonics). A water immersion objective (60×, NA1.2, Olympus) focused the laser beam into a small volume in the specimen, and a confocal pinhole (150μm) was used to reject the out-of-focus emission light. Because there is a transfer lens complex (3x magnification) between the scan unit and the microscope, the pinhole size of 150μm is selected instead of 50μm which is commonly used in the typical FCS setup (see

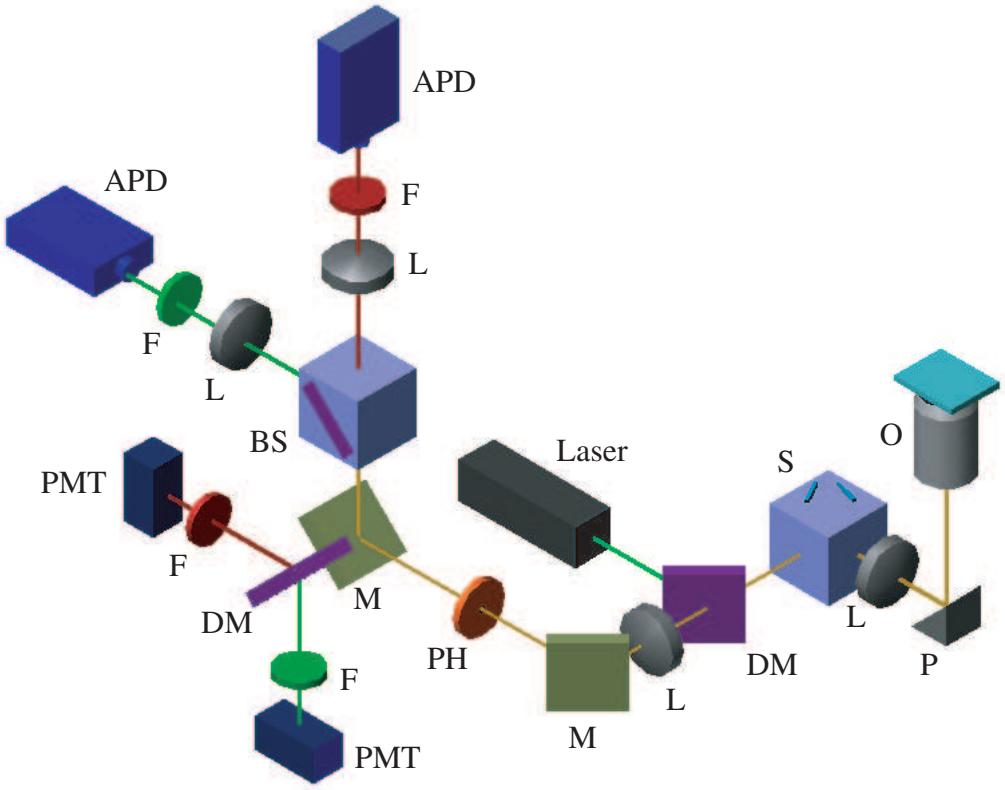

Figure 3.1: The schematic diagram of FCM. APD: avalanche photodiode, PMT: photomultiplier tube, F: emission filter, L: lens, BS: beamsplitter, M: mirror, DM: dichroic mirror, PH: pinhole, S: scanning mirrors, P: reflective prism, O: objective.

section 2.2.6). The signal through the pinhole was collected by either a photomultiplier tube (PMT) for laser scanning imaging or an avalanche photodiode (APD) for FCS measurements, which is switchable using a dichroic/mirror slider (Fig. 3.1). In the FCS detection part, the fluorescent beam was split into two channels and aligned by two lenses (Achromats, f=60mm, Linos, Goettingen, Germany). All the beamsplitters and emitters used in this work are listed in table 3.1. The TTL pulses from APDs (SPCM-AQR-14, Pacer Components, Berkshire, UK) were processed online by a hardware autocorrelator (Flex02-01D, correlator.com). The active area of detectors was 175 μm in diameter. The laser power and measurement time were 100 μW, 30 sec for solution and 25 μW, 10 sec for living cells, unless stated otherwise. FCS curve fitting was performed by a self-written program in Igor Pro (WaveMetrics). In another setup, an ultrafast Ti:Sapphire laser (250 mW, Chameleon-XR, Coherent) was coupled into the same optical pathway for two-photon excitation FCS except for a short pass excitation dichroic mirror (675dcsx, Chroma) and an IR blocking filter (e700sp-2p, Chroma, Rockingham, VT). A maximum pinhole size of 300 μm was chosen in this case for better photon collection efficiency compared with that of 150 μm. For single pinhole spatial FCCS, one pinhole was used to define a single observation volume as in the FCS setup, and the fluorescence light was split into two detectors by a 50:50 non-polarizing beamsplitter cube. However, through an opposite lateral shift of the two detectors only light from one half of the observation volume was projected into detector 1 and the other half into detector 2 (Fig. 3.4). In this case two effective detection volumes were created for cross correlation analysis to measure flow directions.

Table 3.1: Filter List for FCM

Measurement Type	Sample	Beamsplitter	Emitter 1	Emitter 2
Translational Diffusion	Atto 565	-	593/40[a]	-
	TMR	-	593/40	-
	Fluorescein	-	510AF23[b]	-
	R18	-	593/40	-
Rotational Diffusion	GFP	50:50 BS016[c]	510AF23[b]	510AF23[b]
SW-FCCS	SA-QR, BA488	595DRLP[b]	510AF23	695AF55[b]
Spatial FCCS	Atto 565	50:50 BS016[c]	593/40	593/40
TPE FCS	TMR	-	595AF60[b]	-

[a] Semrock, Rochester, NY.
[b] Omega, Brattleboro, VT.
[c] Thorlabs, Newton, NJ.

3.2.3 Chemicals and Cell Culture

Tetramethylrhodamine (TMR), Atto 565, streptavidin - Quantum red conjugate (SA-QR), and biotin - Atto 488 (BA488) conjugate were supplied by Sigma-Aldrich Singapore, while D-biotin by Amersham Biosciences Singapore. TMR and Atto 565 were then dissolved in dimethyl sulfoxide (DMSO) and diluted with deionized water. SA-QR, BA488 and D-biotin were dissolved and diluted with 1× phosphate buffered saline (PBS). SA-QR and BA488 were mixed and then incubated for 10 min before FCS measurements. The sensitivity of rotational diffusion measurement was verified by the binding of wild type green fluorescent protein (GFP) (USBiological, Biomed Diagnostics) to biotin conjugated monoclonal anti-GFP antibody (Rockland Immunochemicals, Inc). For cell culture, a cytosolic GFP vector (EGFP-N1) was purchased from Clontech. Plasma membrane target GFP (PMT-GFP) construct was made by subcloning a plasma membrane targeting sequence (102) to the amino-terminus of

EGFP gene by a two-step PCR. To make the EGFR-GFP construct, enhanced green fluorescent protein (EGFP, Clontech) was attached to the carboxyl terminus of human epidermal growth factor receptor (EGFR) by standard recombinant techniques. Plasmid DNA was prepared using EndoFree Plasmid Maxi Kit (Qiagen). Chinese hamster ovary (CHO-K1) cells (ATCC, Manassas, VA) were cultivated in F-12K supplemented with 10% FBS in T75 culture flasks until 70% confluency when cells were washed with 1× PBS and tripsinized. For each reaction 3-5×10^6 cells were mixed with 5 μg plasmid in 200 μL normal growth medium in 0.2 cm cuvette (Bio-Rad) and electroporated by the Genepulser Xcell (Bio-Rad, Hercules, CA) following the manufacture preset experimental parameters. Transfected cells were seeded on 30 mm circular coverslips (Lakeside, Monee, IL) in a 6-well plate and growing in culture medium for 2 days. Cells were starved with reduced-serum medium (0.2% serum in F-12K) for 4-8 hours to prevent endocytosis. The circular coverslip were mounted in a POC mini chamber (Carl Zeiss, Singapore) and the cells were immersed in 1×PBS for FCS measurements. More details of the setup can be found in this paper (103). In addition, octadecyl rhodamine B chloride (R18) (10nM, Invitrogen, Singapore) was used as an indicator for membrane diffusion. It was diluted in 1×PBS solution, added into the chamber and incubated 10 min for the following measurements.

3.3 Results and Discussions

3.3.1 Calibration

One of the main advantages of the FCM system constructed here is its versatility in terms of different applications and its capability to spectroscopically measure any point

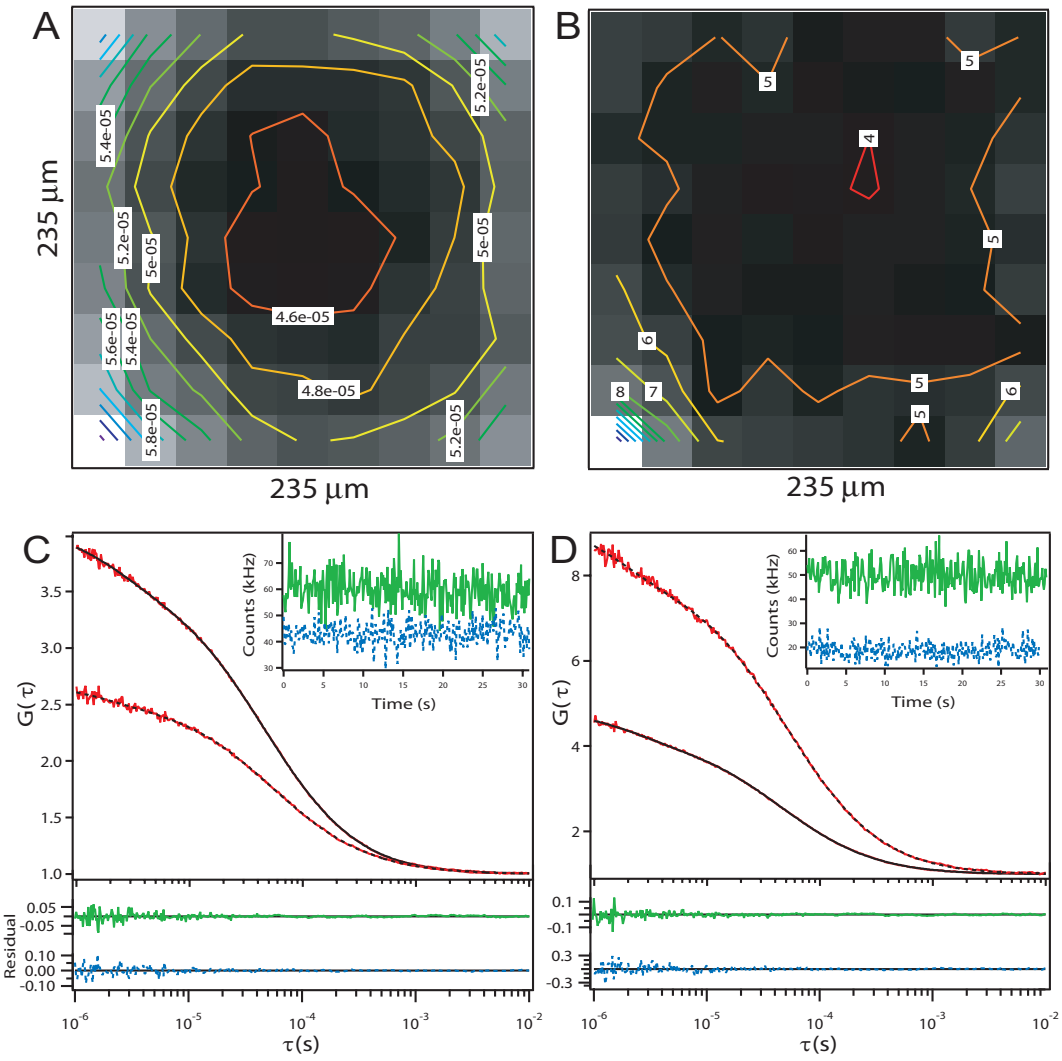

Figure 3.2: The contour maps of A) diffusion time, τ_d (sec) and B) structural factor, K measured in Atto 565 solution (1 nM) are shown in the CLSM image area. C) ACF curves at the center (solid black line) and the periphery (dashed line) of the image are compared. The respective count rates (inset) and fitting residuals are also shown. D) Atto 565 (solid line) and TMR (dashed line) were used at a concentration of 1 nM to calibrate the performance of FCM at the image center.

within the field of view. To determine whether the performance of the instrument is equally good at any point, I performed system calibration by measuring the ACFs over a grid of 9×9 points covering the full field of view. A 1 nM dye solution of Atto 565 was sealed in a chamber to prevent evaporation. All the ACF curves were fitted with equation 2.20 and two contour plots of the measured τ_d and structure factor K are shown in Fig. 3.2. The τ_d was found to be 45.1±0.2 μs in the center and up to 58 μs in the peripheral edges, leading to a circular contour pattern (Fig. 3.2A and C). A similar pattern of the structure factor K was measured with a minimum value of 4.0±0.1 in the center (Fig. 3.2B). The count rate per particle for Atto 565 was as high as 201 kHz at the central point while it decreased by a factor of 0.3 – 0.51 at the peripheral points. This result is consistent with the distribution patterns of τ_d and K. Ideally the values of τ_d, K and count rate per particle should be constant assuming that the laser focal volume does not change at different positions. However, optical aberrations lead to deviations when the laser focus was parked at a position other than the center. While these aberrations have a smaller effect in imaging, they have a stronger influence on the ACF due to the change of the confocal volume. These artifacts can lead to misinterpretations. Nevertheless, within the central area of 75 μm radius, representing 30% of the total area of the field of view, no difference can be seen in the ACFs. Furthermore, the error is less than 10% in an area with 100 μm radius, representing more than 60% of the field of view. The FCM system has 5 built-in pinhole sizes of 60, 100, 150, 200 and 300 μm diameter, which yield various count rates per particle 92, 161, 201, 195 and 174 kHz respectively for Atto 565. The optimal pinhole size 150 μm was chosen according to its best performance on count rate per particle for a particular dye. Additionally, FCS measurements at the central point produced very stable ACFs with high count rates per particle of 134 kHz for TMR (Fig. 3.2D) excited

at 543 nm and 11 kHz for fluorescein excited at 488 nm. The count rate per particle was as good as 13 kHz for TMR by two-photon excitation at 850 nm.

3.3.2 SW-FCCS

Dual color single beam FCCS was initially developed to detect the interaction of molecules with similar molecular weights (58). Two fluorescent molecules with minimal emission spectral overlap are typically used in order to minimize the cross-talk into the neighboring detectors. Furthermore, it requires two laser beams to be exactly focused into the same spot which prevents the wide application of this technique. An alternative source was two-photon excitation (64; 65) but a more expensive laser was needed. Single wavelength FCCS (SW-FCCS) using a CW laser was then proposed and verified for multicolor detection of molecular interactions in solution (59; 60) and has also been applied to protein-protein interaction in living cells (103; 104). The FCM in this case can be simply extended to perform SW-FCCS by selectively switching on one of the lasers and using a dichroic mirror to split the emission light and different band pass filters for the detectors (Table 3.1). SW-FCCS measurements were performed with the standard streptavidin-biotin system by using streptavidin-Quantum red (SA-QR, 1 nM) which is a streptavidin-phycoerythrin conjugate and a biotin-Atto 488 conjugate (BA488, 0.5-8 nM). As a negative control, excess D-biotin (200 nM) was added the solution of SA-QR (1 nM) to block all the binding sites of SA before BA488 (4 nM) was added. The CCF curves (Fig. 3.3) demonstrate that the amplitudes decreased with the increasing concentrations of BA488 which corresponded to the increasing number of bound complexes in the solution (Equation 3.3). The result is consistent with earlier published data (59). Most importantly, this work shows that

FCM can integrate SW-FCCS with the existing CLSM and thus allows the spatially precise measurement of molecular interactions in living cells using single laser line excitation.

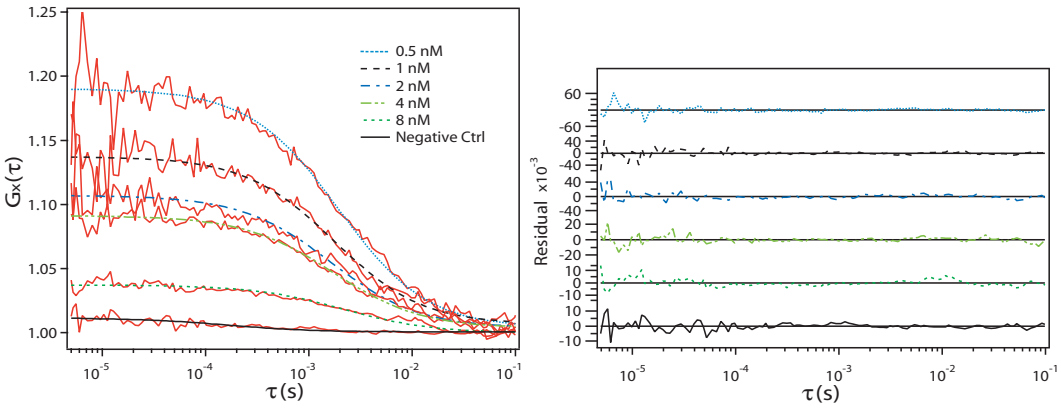

Figure 3.3: SW-FCCS was performed by the FCM. The amplitude of cross correlation curve decreases with the increasing concentration of BA488, which corresponds with the increasing number of bound complexes (SA-QR and BA488). The concentration of SA-QR was 1 nM. The curves were fit using equation 3.3 and the residuals are shown.

3.3.3 Single Pinhole Spatial FCCS for Flow Velocity Measurements

In the past decade microfluidic structures have been widely used in chemical analysis and biological sciences. An effective tool to characterize the fluid system is often required so as to optimize its performance in the particular research field. Particle imaging velocimetry (PIV) is among the most popular approaches to acquire microfluidic velocity profiles in microstructures (16). FCS was also demonstrated to measure flow in a microchannel at higher spatial resolution (32) compared with PIV but without any information about microfluidic flow directions. Therefore, several improved schemes were proposed to obtain flow directions including spatial dual beam FCCS (62) and asymmetric focal volume FCS (105). A simple method, line scan FCS per-

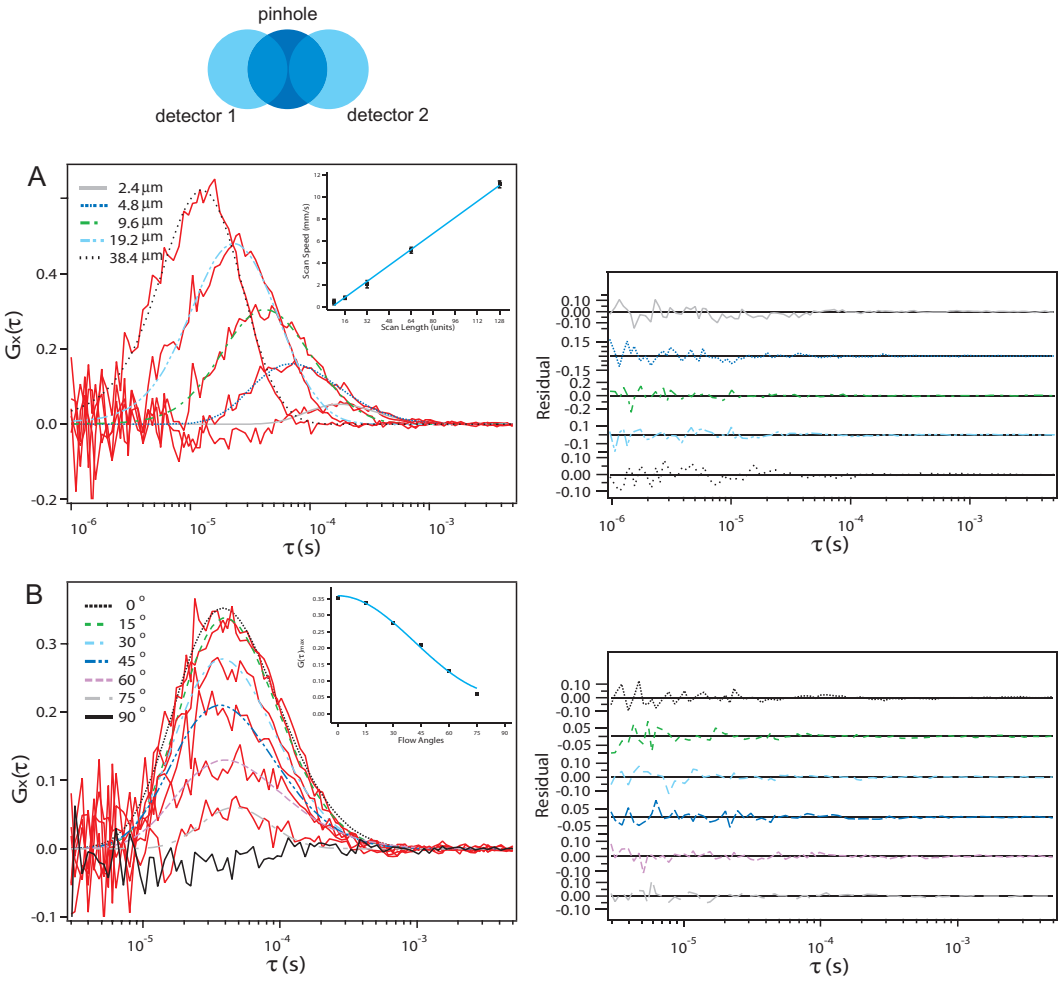

Figure 3.4: Single pinhole spatial FCCS was realized by the displacement of two detectors in a small distance. A) CCF curves for different line scan speeds and the linear dependence of measured ”flow” speeds on the scan lengths (inset); B) effect of flow angles on the cross correlation amplitudes, and the change of $G(\tau)_{max}$ with flow angles (inset).

formed on the FCM to characterize the flow direction in both microchannels and blood vessels of zebrafish embryo shall be described in chapter 4. The traditional dual beam FCCS setup is complicated which requires generation of two spatially separate laser beams with the same excitation profile and their precise 3D alignment. A simplified scheme was to use an extended excitation volume which contains two separate detection volumes defined by two different pinholes (106). However, this scheme sacrifices the spatial resolution of FCS and thus limits its applications. Here I present single pinhole spatial FCCS performed on the FCM for microfluidic flow as described in the optical setup. CCFs for intensities from the two effective detection volumes were obtained, and pure CCFs for flow were then calculated as described in theory. The ”flow” of solution in a close chamber was simulated by superimposed slow line scans and the flow velocity is proportional to the scan line length as shown later in chapter 4. Firstly, microfluidic flow velocity in the microchannel was measured by single pinhole spatial FCCS, and CCF curves with different flow velocities are shown (Fig. 3.4A). The amplitude of $G_{xf}(\tau)$ increases when the flow is fast. This is because the effect of diffusion is more significant when the flow is slower, which means fewer molecules flowing from one detection volume will be detected by the other volume. All the data were fitted to equation 3.4, and the respective fitting residuals are shown in Fig. 3.4A. From fitting results, it is found that $\tau_d = 2.2 \pm 0.4\mu s$, $R = 4.8 \pm 0.4$, and the distance between two detection volumes is calculated to $0.25 \pm 0.05\mu m$. As the two effective detection volumes exist within one excitation focal volume, this distance is close to the focal radius $0.22\mu m$ measured in the traditional FCS calibration. Additionally τ_{xf} was obtained from the data and the flow velocity was then calculated (Fig. 3.4A, inset). As shown in chapter 4, the measured flow velocity is linearly dependent on the length of scan line, which is proportional to the laser beam scan velocity. Secondly,

microfluidic flow directions can be characterized by single pinhole spatial FCCS. The length of scan line was set to 9.6μm. The flow axis was rotated at several angles of 0°, 15°, 30°, 45°, 60°, 75° and 90° with respect to the initial flow direction. All the pure CCF curves for flow are shown in Fig. 3.4B and fitted to equation 3.4 while τ_d and flow angle were fixed. The amplitude of the CCF curves started with a maximum at flow angle of 0° and ended with a minimum at 90° (Fig. 3.4B, inset) as expected from the equation 3.4. The reason is that the number of molecules entering volume 2 from volume 1 is decreasing when the flow direction is deviating from the connecting line of two effective detection volumes. The single pinhole scheme simplifies the optical setup of dual beam spatial FCCS for microfluidic flow and retains the imaging capability of optical systems if applicable, and it does not require extra scanning mirrors compared with the line scan FCS presented in chapter 4. The single pinhole spatial FCCS can provide direct yes/no answers to some special flow cases on microchips, such as the cross point of two microchannels (107). However, in practical applications one has to rotate either the sample or the detectors for a calibration to obtain the minimum and maximum amplitudes of CCFs. The unknown flow angle can then be calculated according to equation 3.4 when the CCF amplitude at the point is measured.

3.3.4 Diffusion on Cell Membranes

It has been reported that membrane defocusing and membrane inclination with respect to the focal plane can cause changes in diffusion time measured and leads to inaccurate diffusion coefficients (108; 109). However, this has not been confirmed on cell membranes. In this work, the diffusion of R18 on the upper and lower membranes was investigated (Fig. 3.5). R18 is an amphiphilic fluorescent membrane dye which

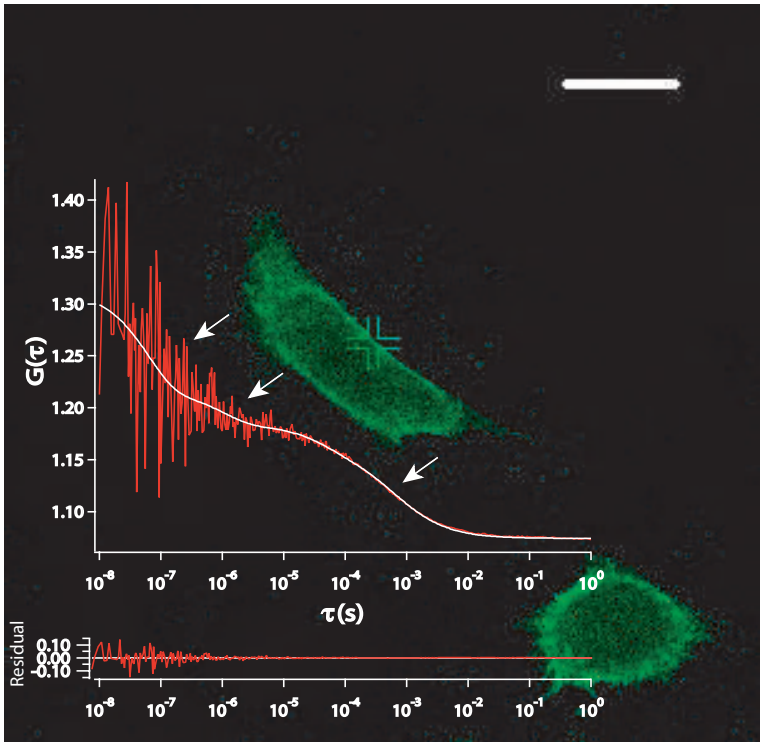

Figure 3.5: Translational and rotational diffusion on CHO cell membranes can be measured by the FCM. Cross: FCS measurement point; Arrows (from left to right): rotational diffusion in 10-100 ns time range, triplet state relaxation in 1 μs, translational diffusion in 1 ms. Bar: 20μm.

can be randomly inserted into the plasma membrane lipid bilayer driven by hydrophobic interactions. It does not have any large extracellular domain thus the interaction of R18 with other structures and proteins on the membrane was reduced. The use of R18 therefore isolated the effect contributed by the defocusing and inclination by reducing the effect due to the heterogeneity of membrane surface. The positions of upper and lower membrane were located by doing a z-scan at each point. Z-stack images of the cells were taken whenever possible to deduce the general inclination of the plasma membrane at various points of the cell. The average diffusion coefficients of R18 measured on the upper and lower membranes were $33.4 \pm 9.8 \times 10^{-9}$ (RSD: 29%) and $40.7 \pm 10.3 \times 10^{-9}$ (RSD: 25%) cm^2/s respectively, where RSD represents the relative standard deviation. There was a difference of less than 30% between the diffusion coefficients of R18 on the upper and lower membranes with small SD, which suggests that its diffusion on the membrane is not significantly affected by the cellular membrane topography. This is consistent with the earlier report that the contribution to errors in membrane diffusion measurements due to geometrical effects was significant only when the angle of inclination of the membrane was more than 50 degrees (108). Furthermore, the rotational diffusion of GFP on CHO cell membranes was investigated (Fig. 3.5) and the results are presented in the next section.

3.3.5 Rotational Diffusion of GFP

Table 3.2: Rotational diffusion of GFP

Sample	GFP_{PBS}	GFP-AB	GFP_{cyto}	PMT-GFP	EGFR-GFP
τ_{rot}(ns)	20.8±1.4	98.4±5.5	16±11	67±25	118±24

From the Stokes-Einstein equation $D = kT/6\pi R_h\eta$ and the equation $\omega_0^2 = 4D\tau_d$ for FCS, it is known that the translational diffusion time is proportional to cube root of molecular mass: $\tau_d \propto \sqrt[3]{M}$. While from the Stokes-Einstein-Debye (SED) equation $\tau_{rot} = \eta V/kT$, the rotational relaxation time is directly proportional to its molecular mass: $\tau_{rot} \propto M$. Thus the rotational time is more sensitive than translational diffusion time to the mass change of rotating molecules. Pure GFP and GFP-antibody (GFP-AB) binding complexes in buffer solution were investigated and their rotational times were measured as 20.8±1.4 and 98.4±5.5 ns respectively (Table 3.2). The full range curve of GFP rotational (Fig. 3.6A) and translational diffusion time (Fig. 3.6B) is also shown when the concentration of GFP-antibody increases. I observed an increase of both the translational (2.4×) and the rotational (4.7×) diffusion time for the binding of GFP with its monoclonal antibody. The ratio 4.7 for two rotational times was close to the mass ratio 6.4 for GFP (28 kDa) and GFP-AB (178 kDa) considering that the SED equation assumes a spherical molecule, while the translational diffusion time increase was approximate to cube root of the mass ratio. As expressed in living cells (CHO, N=10), the rotational dynamics of GFP in cytoplasm, on plasma membrane (PMT-GFP) and with receptor protein (EGFR-GFP) behaves differently. The rotational times of the GFPs are listed in Table 3.2. From the result, the rotational diffusion was about fourfold slower when GFP was attached to the cell membrane compared to freely diffusing GFP in the cytoplasm. The difference is due to the membrane viscosity which slows down the GFP rotation. I also compared PMT-GFP (~28 kDa) and EGFR-GFP (~ 198kDa) on the plasma membrane of CHO cells and found that the rotational time increased about twofold, which could be explained by the size increase of the protein residing in the plasma membrane.

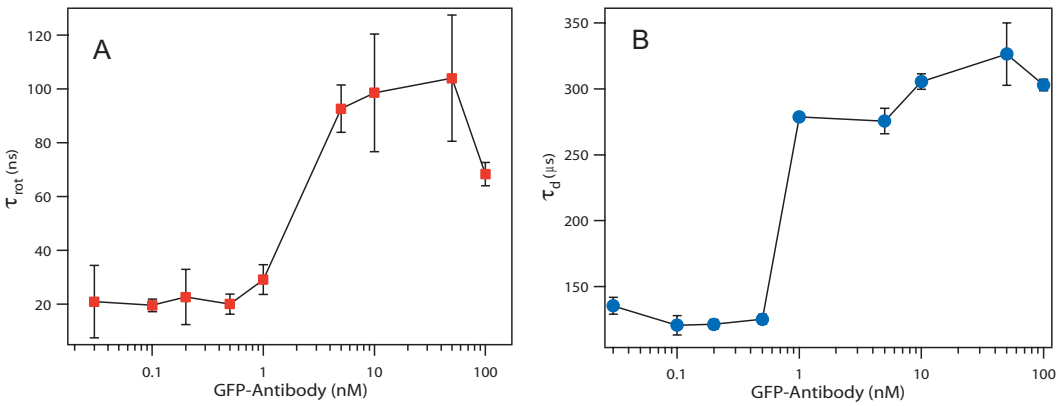

Figure 3.6: A) Rotational diffusion time of GFP (100 nM) when bound to its monoclonal antibody (3, 10, 20, 50, 100, 500 nM, 1, 5, and 10 μM) is compared with B) its translational diffusion time. The rotational diffusion is more sensitive to molecular mass change than the translational diffusion, which was reflected by a factor of 4.7 increase for rotation time and a factor of 2.4 for translational diffusion time.

3.3.6 Two-Photon Excitation FCS

The FCM facilitates wide applications of FCS in living cells and makes possible the accurate spatial positioning of the observation volume. However, quantitative microscopic measurements in living tissues require two-photon excitation which reduces light scattering, photodamage and autofluorescence, and increases optical penetration depth. Two-photon FCS has been characterized for intracellular applications (50) and flow analysis (107). Here I described the performance of two-photon FCS by the FCM. Different TMR concentrations (5, 10, 20, 50 and 100 nM) resulted in a decreasing amplitude of the ACF curve (Fig. 3.7A). Similar to one-photon FCS, a line scan scheme was used for two-photon FCS to simulate different ”flow” speeds in TMR solution (20 nM) which were reflected by the shorter flow time (Fig. 3.7B and C). One-photon line scan FCS can be used to measure flow direction with high spatial resolution as discussed in chapter 4, and it will be shown below that two-photon line scan FCS is also able to characterize the microfluidic flow direction with small measurement errors.

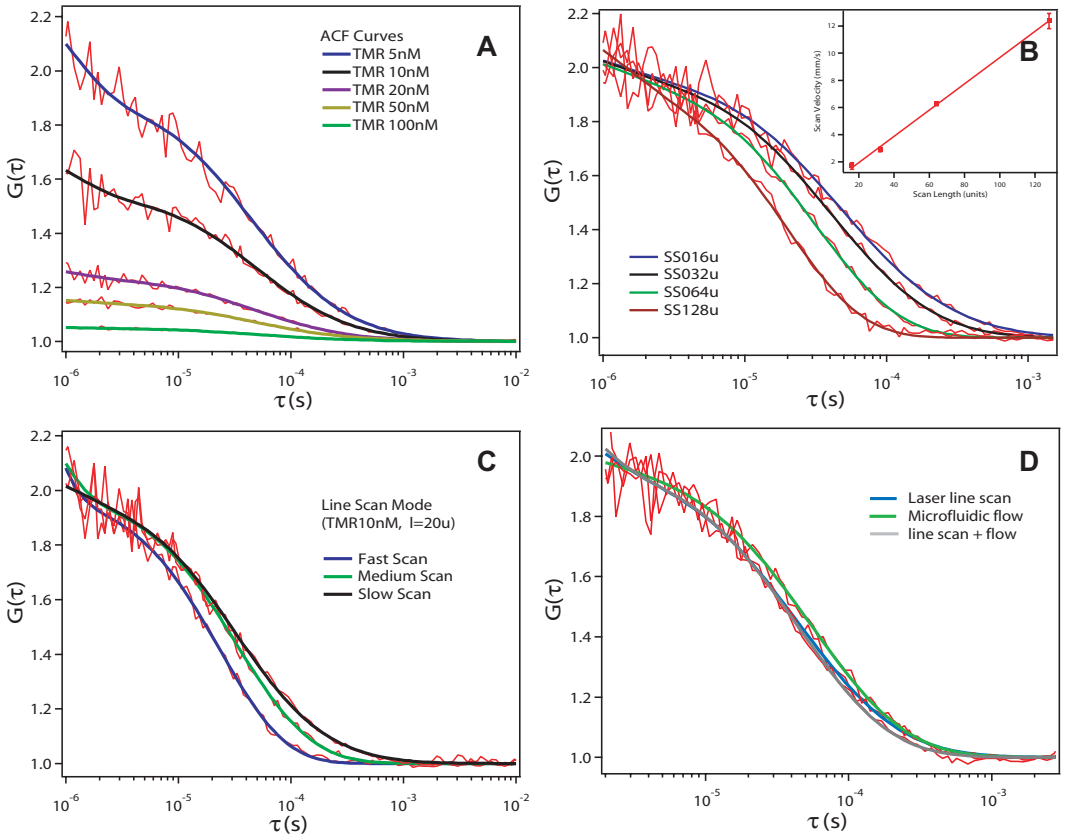

Figure 3.7: A) TPE FCS measurements in TMR solution (5nM, 10nM, 20nM, 50nM and 100nM); B) ACF curves of TPE line scan FCS with different scan lengths, inset: measured scan speed versus scan length; C) ACF curves of TPE line scan FCS in different scan modes; D) Two-photon excitation line scan FCS for flow direction measurements. ACF curves for laser line scan, microfluidic flow and net flow are plotted.

The basic principle of line scan FCS will be described in the next chapter (section 4.2). Briefly, an external ”flow” is superimposed onto the microfluidic flow when the laser beam is linearly scanning. The angle formed by these two flows can be calculated once the net velocity by the two flows are measured, finally the real microfluidic flow direction is obtained from the difference of the line scan angle and the angle calculated (46). The measurement was performed in a polydimethylsiloxane (PDMS) microchannel with flowing TMR solution (20 nM). The flow axis was manually aligned to 0° by eye and the line scan angle was set to 90° by the CLSM system. All the ACF curves are shown in Fig. 3.7D and fitted to equation 2.26. The line scan speed, the microfluidic flow speed and the net speed by above two flows were measured as 2.61 ± 0.01, 2.62 ± 0.16, 3.51 ± 0.03mm/s. The flow angle was thus obtained as 5.96 ± 0.77 ° that is close to the initially aligned flow angle. It shows that two-photon excitation line scan FCS can determine the flow angle in a microchannel with acceptable experimental errors. Therefore the application of line scan FCS to living tissue and small organisms could be expected due to the well known beneficial features of two-photon excitation microscopy in deep and thick tissues.

3.4 Conclusion

In this chapter I present a modification of FCM which ensures that the points measured by FCS are identical with those imaged by CLSM by using the same pinhole for imaging as well as for FCS measurements. By coupling a pulsed Ti-Sapphire laser source into the microscope two-photon FCS can be performed with the same modalities shown above. I demonstrated the use of the setup by measuring diffusion coefficients of R18 on the upper and lower membrane of cells as well as SW-FCCS for molecular

interactions. Spatial FCCS by a single pinhole scheme and two-photon excitation line scan FCS were introduced for the flow direction characterization. The good performance of the setup (count rates per particle > 100kHz) makes this FCM instrument a very reliable tool for biological measurements. Furthermore, recent developments in data treatment, which allow global analysis of FCS data (110) and use new search algorithms for fitting FCS data without the need of initial guesses (111), could be combined with this versatile system to make FCM a more commonly used tool in the life sciences.

With the flexible FCM system available, it is possible to extend its functionality to some special application. In the next chapters, the FCM system is used to perform line scan FCS in order to measure the microfluidic flow direction in 2D and 3D. The method can be applied to both microchannels and small blood vessels in living organisms.

Chapter 4

Two Dimensional Microfluidic Flow Direction

4.1 Introduction

It has been discussed in chapter 2 that FCS can measure the microfluidic flow speed in microstructures. This was done by positioning of the observation volume at a certain point. In addition to single point measurements, FCS has been extended to obtain flow profiles by positioning the observation volume point by point in a microfluidic channel (32) to acquire microfluid velocity images vertically and horizontally (112). However, the FCS probe volume is rotationally symmetric in the focal plane, thus no information about flow directions can be obtained. A rectangular or elliptical laser beam cross-section was used thus breaking the symmetry of the probe volume in the plane of focus (105). In these systems the traveling time of molecules through the observation volume depends on the structural extension of the focal volume in flow direction, it varies from a minimum when the flow is parallel to the short axis, and to a maximum when

the flow is along the long axis. However, the methods measure only different flowing times but not flow velocities because of the focal volume geometry. The flow direction is still ambiguous since opposite flows cannot be distinguished. Their applications in biological tissues are limited for these strategies because the focal geometry cannot be accurately characterized due to the refractive index distortion in biological specimens. The other improved schemes are dual-beam FCS (62), coupled with techniques of two-color cross-correlation (57) and time-delayed two-photon pulse excitation (107). But their drawbacks are low spatial resolution for directionality analysis because of two far-separate observation volumes and limited detection efficiency at large flow angles. No application of these two methods in practical microstructure systems for actual angle determination has been presented yet.

In this chapter, line scan FCS is proposed for the analysis of flow profiles in microchannels and even living tissues with high spatial resolution. Scanning FCS since its invention has been used for various biological applications (70; 113). Additionally, two-photon excitation improves its detection efficiency and accuracy (114). Recently, two kinds of scanning FCS techniques are reported to measure protein or molecule flow velocities, such as spatio-temporal image correlation spectroscopy (STICS) (78), and circular scan FCS (so-called position sensitive scanning FCS, PSFCS) (74). Here we present a modified confocal laser scanning microscope called FCM which allows FCS measurements and performs line scan FCS as one of its functions (see chapter 3). Under defined conditions, e.g. line scan time for one direction is much longer than that of the other direction, the line scans can be considered as quasi single directional for FCS analysis. Hence, by linearly scanning the probe volume through the sample one introduces an external single directional ”flow” into the microfluidic system without internal disruption. If the speeds of internal microfluid flow, external ”flow” and the

net flow are measured, the angles formed by external flow and internal microfluid flow can be calculated. Importantly, line scan FCS has an advantage that the scanning speed is not the key parameter to resolve flow directions, which is critical for the cases like tissue measurements when the focus geometry is unknown. This method is verified by the investigations of flow profiles in a center-obstructed microchannel and applied to the determination of blood flow angles in small blood vessels in an immobilized living zebrafish embryo.

4.2 Theory

4.2.1 FCS Measurements

FCS measures temporal intensity fluctuations of fluorescent molecules caused by their dynamic processes, such as diffusion or flow, within a small open volume which is defined by a focused laser beam. The autocorrelation function (ACF) of the fluorescence fluctuation signal for pure three dimensional diffusion is given by the following equation (22; 28; 92),

$$G(\tau) = \left(\frac{F_{trip}}{1+F_{trip}} e^{-\tau/\tau_{trip}} + 1\right) \frac{1}{N} \frac{1}{1+\tau/\tau_d} \frac{1}{\sqrt{1+\tau/(K^2\tau_d)}} \tag{4.1}$$

Where, N is the number of molecules; τ_d is the diffusion time of molecules through the focal volume; τ_{trip} is the relaxation time of the molecule from the triplet state to the ground state; F_{trip} is the fraction of the number of molecules in the triplet state; The structural parameter K is defined as z_0/ω_0, an important factor to characterize the optical alignment; ω_0 and z_0 are its radial and axial extensions, defined as the distance from the focal point where the intensity has decreased by a factor of e^{-2} compared to

the central intensity.

4.2.2 FCS Flow Analysis

Measurement of microfluid flow speeds by FCS was first described with the assumption that flow is uniform and single directional in a plane perpendicular to the optical axis. The normalized ACF in the case for a single flow component coupled with free diffusion results in a one-flow model,

$$G(\tau) = \left(\frac{F_{trip}}{1 + F_{trip}} e^{-\tau/\tau_{trip}} + 1 \right) \frac{1}{N} g(\tau) \, e^{-\left[(\tau/\tau_f)^2 \frac{1}{1+\tau/\tau_d} \right]} \tag{4.2}$$

with

$$g(\tau) = \frac{1}{1 + \tau/\tau_d} \frac{1}{\sqrt{1 + \tau/(K^2 \tau_d)}} \tag{4.3}$$

Here, τ_f is the traveling time of molecules through the focal volume. The flow speed is calculated as $V = \omega_0/\tau_f$. It should be noted that a single directional scan of the laser focus with constant velocity in a static solution will generate the same flow pattern (equation 4.2).

4.2.3 Laser Focus Bi-directional Scans

When two independent flow components are present in FCS measurements, the ACF can be expressed as a two-flow model (equation 4.4). This situation does usually only arise when the two flow components exist independently at different times as is the case in an organism with a heart beat, where systolic and diastolic flow is different, or any system in which the flow is alternated between two different flows. This is also the case when a CLSM is doing bi-directional scans with alternating forward and backward

scans of different scan speeds. Under the assumption that the scan times are larger than the diffusion time ($T_{forward} > \tau_d, T_{backward} > \tau_d$), the forward and backward scans can be treated as independent. Therefore, the resulting ACF for laser bi-directional scans is represented by a two-flow model.

$$\begin{aligned} G(\tau) &= \left(\frac{F_{trip}}{1+F_{trip}} e^{-\tau/\tau_{trip}} + 1\right) \frac{1}{N} g(\tau) \cdot \\ &\quad \left\{ F_{f1} \cdot e^{-\left[(\tau/\tau_{f1})^2 \frac{1}{1+\tau/\tau_d}\right]} + (1-F_{f1}) \cdot e^{-\left[(\tau/\tau_{f2})^2 \frac{1}{1+\tau/\tau_d}\right]} \right\} \end{aligned} \tag{4.4}$$

Here F_{f1} is the fraction of time the system experiences the flow with a characteristic flow time τ_{f1}, and $(1 - F_{f1})$ is the fraction of time the system experiences the flow with a characteristic flow time τ_{f2}. For the case of the bi-directional scans $F_{f1} = T_{forward}/(T_{forward} + T_{backward})$, where $T_{forward}$ and $T_{backward}$ represent the times the system experiences forward and backward scans.

4.2.4 Analysis of Flow Directions

As illustrated in figure 4.1A, the laser beam is scanned at an angle of θ with respect to the flow direction in the microchannel. By considering the scanning laser focus as a reference, and assuming a constant scan speed in one direction, a schematic diagram of relative velocities can be drawn (figure 4.1B), where V_n is the net velocity vector of the combined flows of V_{scan} and V_{flow}. The mathematical relationship of those three velocities can be defined by the equation as follows.

$$V_n^2 = V_{flow}^2 + V_{scan}^2 - 2 \cdot V_{flow} V_{scan} \cos(180 - \theta) \tag{4.5}$$

V_{scan} can be determined for a specific instrument by single point FCS flow analysis in a solution without flow, V_{flow} can be measured in the flowing sample solution with a stationary laser focus, and V_n is measured in the same flowing sample while linearly scanning the laser focus. With these three parameters known, the angle θ can be calculated.

$$\theta = 180 - \arccos\left(\frac{V_{flow}^2 + V_{scan}^2 - V_n^2}{2 \cdot V_{flow} V_{scan}}\right) \tag{4.6}$$

As long as the laser line scan direction is known, the flow angle can be determined as $\theta_{flow} = \theta_{scan} - \theta$. This is true under the assumption that flow speed and direction in the sample does not vary significantly over the scanning distance. In this case, the resolution of this method is limited by the length of the scan line.

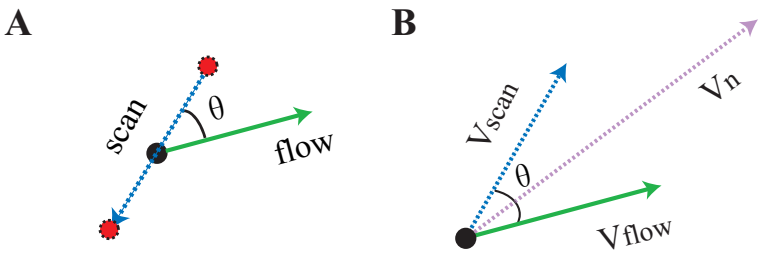

Figure 4.1: A) Single point FCS is implemented at the black spot, line scan FCS is performed along the dash line and the direction of microfluidic flow (V_{flow}) is indicated by an arrow. B) Schematic relationship of the laser beam scan (V_{scan}), V_{flow} and the net velocity (V_n) is described, taking the laser focal spot as a reference point.

4.3 Experimental Section

4.3.1 Selective Scan Length

The analog voltage, a saw tooth signal used to control the scanner to perform the line scan, was acquired and converted to a digital signal (DAQCard 1200, National Instru-

ments Singapore). A self-written program (LabView, National Instruments Singapore) was used to create a TTL output pulse for each minima of the saw tooth signal to synchronize the data acquisition with the line scan. The arrival times of these TTL pulses marking the start of a scan line and the signals from the APD were simultaneously recorded by a counter/timer device (PCI-6602, National Instruments Singapore). The synchronization of the fluorescence signal with the scanner allows the accurate selection of data acquired during any specific phase of the line scan. The ACF data calculation and curve fitting were completed by programming in Igor Pro.

4.3.2 Microchannels

Teflon is used to fabricate a microchannel mold with one inlet (figure 4.2A, a) and two outlets (figure 4.2A, b and c), its cross-section is a rectangle of 380 μm width and 300 μm height. Pre-polymer of polydimethylsiloxane (PDMS) (Sylgard 184, Dow-Corning, Midland, MI, USA) is poured over the molds and cured at 65^oC overnight before peeling off. The PDMS membrane is oxidized in oxygen plasma for 1 minute in order to be chemically bonded to a glass coverslip. In order to generate an obstruction flow pattern, a fiber with a radius of 100 μm is inserted into the center of a microchannel after the fabrication process (figure 4.2A, d). A syringe pump (KDS100, Fisher Scientific, Singapore) is employed for the perfusion of probe solution into the microchannels through tubing and connectors. Different flow velocities in the microchannel can be induced by varying the syringe pump rates.

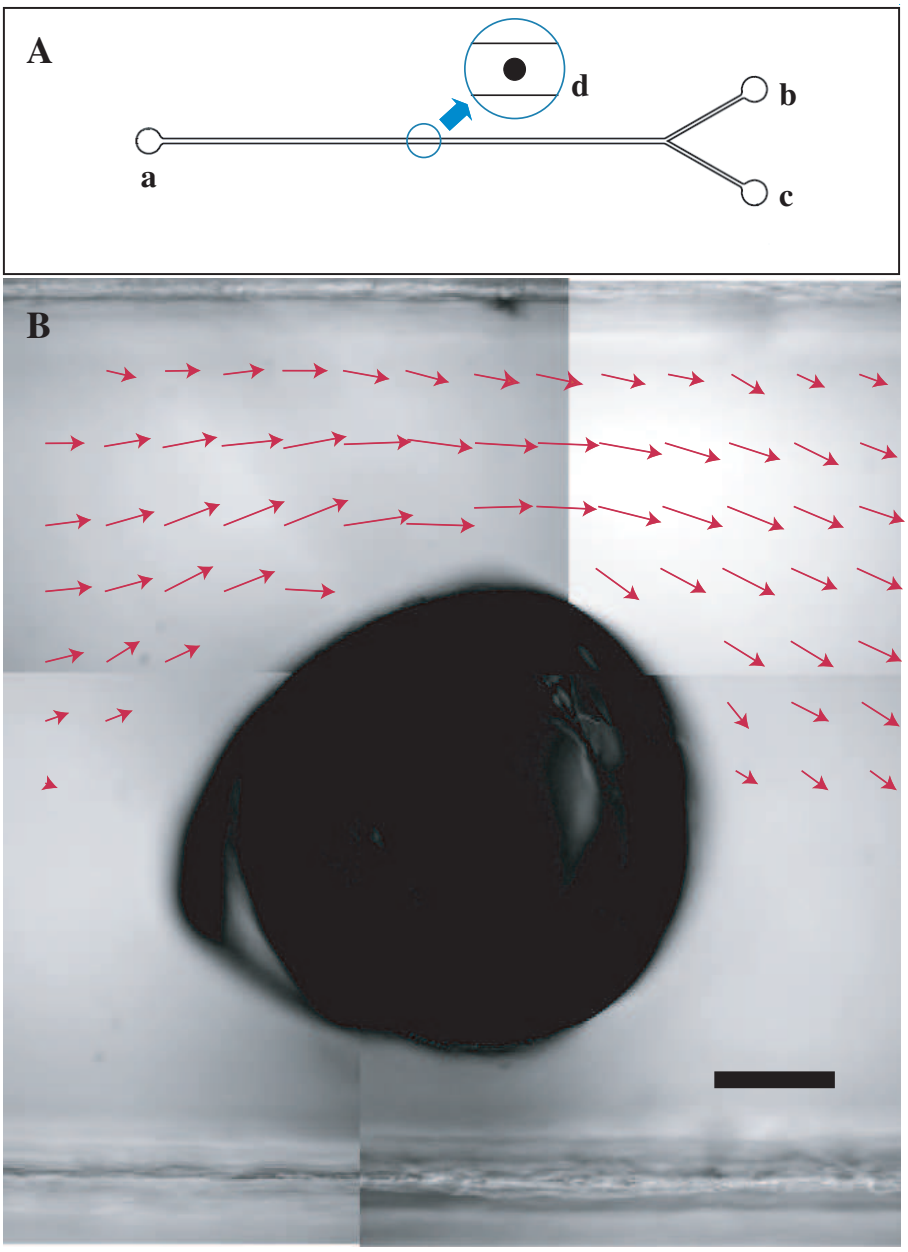

Figure 4.2: A) A PDMS-glass microchannel structure is depicted which has an inlet (a) and two outlets (b and c). An obstruction flow pattern is achieved by a fiber inserted in the center of the microchannel as shown in the inset (d). B) Flow velocity vectors measured by line scan FCS are plotted around an obstacle fiber in the microchannel. The length and arrow of those vectors represent the flow speed and direction. (Bar, 50μm)

4.3.3 Zebrafish

The maintenance of zebrafish was based on the protocols in the zebrafish book (115). Briefly, a pair of AB wild-type zebrafish was crossed and their embryos were collected the next morning. The embryos were then incubated in egg water ($60\mu g/ml$, Instant Ocean® Sea Salts (Aquarium Systems, Inc.)) at $28.5°C$ for the optimal development, and after 20 hours post fertilization (hpf) PTU (0.003% 1-phenyl-2-thiourea in 10% Hank's saline, Invitrogen, Singapore) was added to prevent pigmentation. Embryos were dechorionated at 55 hours and then anaesthetized by Tricaine (ethyl m-aminoboenzoate, Sigma, Singapore). The treated embryos were mounted in 0.5% low melting temperature agarose (Invitrogen, Singapore) in a WillCo-dish® glass bottom dishes (GW-3512, WillCo-Wells, The Netherlands) for the following measurements.

4.3.4 Procedures

A dye solution (1 nM, Atto565, Sigma, Singapore) was prepared in deionized water as a probe for all flow measurements. Excitation was at a power of $\sim 100\mu W$ just before the objective provided by a HeNe laser (543nm). Line scan speeds of different scan modes, such as fast, medium and slow, were calibrated and measured in a static dye solution; various flow speeds induced by a syringe pump were obtained by single point FCS measurements and the combined speeds of flow and scan were acquired by line scan FCS. As a compromise of the accuracy and resolution, a slow scan line of $3\mu m$, perpendicular to the channel wall, is selected for the applications of the method in flow velocity mapping in microchannels and zebrafish tissues. The acquisition time was 30 seconds for all measurements. The structural parameter K, extracted from a calibration measurement, was the only parameter to be fixed for the following data fitting.

4.4 Results and Discussion

4.4.1 Fit Models and Line Scans

Table 4.1: Key parameters obtained by fitting ACF curves of fast, medium, and slow line scan modes with a one-flow and a two-flow model; for the ratio of τ_{f1} over τ_{f2}, values in parenthesis were measured by oscilloscope

Modes	τ_f or τ_{f1} (μm)	τ_{f2} (μm)	τ_{f1}/τ_{f2}	F_{f1}	χ^2_ν	F Test
Fast	51.9 ± 0.2				3.13 ± 0.17	93.4%
	59.8 ± 1.1	25.0	2.39 (2.00)	0.81 ± 0.03	2.75 ± 0.17	
Medium	92.1 ± 0.9				1.25 ± 0.16	74.9%
	97.2 ± 2.4	26.9 ± 3.2	3.61 (3.27)	0.92 ± 0.05	1.18 ± 0.12	
Slow	16.2 ± 0.3				0.96 ± 0.11	81.1%
	16.8 ± 0.7	32.6 ± 5.6	5.15 (5.33)	0.92 ± 0.03	0.89 ± 0.11	

The FCM has three bi-directional line scan modes, namely fast, medium and slow. Time durations of these scan modes for one cycle ($T_{forward}$+$T_{backward}$) are 1.00+0.50ms, 1.80 + 0.55ms and 3.20 + 0.60ms respectively, regardless of the lengths of the scan line, as determined from the scanning mirror input voltages by an oscilloscope. Three normalized ACF curves of 3μm line scans in the modes of fast, medium and slow are shown (figure 4.3A). The shorter the scanning time, the faster will be the scan speeds, which is emphasized by a shorter decaying time in the ACF curve (τ_f, equation 4.2). Furthermore, the speed of a line scan is proportional to its length. The longer the line, the faster is the laser beam scan (figure 4.3B). In the experiment, we used both a one-flow model (equation 4.2) and a two-flow model (equation 4.4) to fit the data and fitting results are shown in table 4.1. From the values of χ^2_ν, which is a good indicator of difference between the fitting functions and raw data (116; 117), it can be seen that for the medium and fast bi-directional line scan modes the fits tend to deviate more from

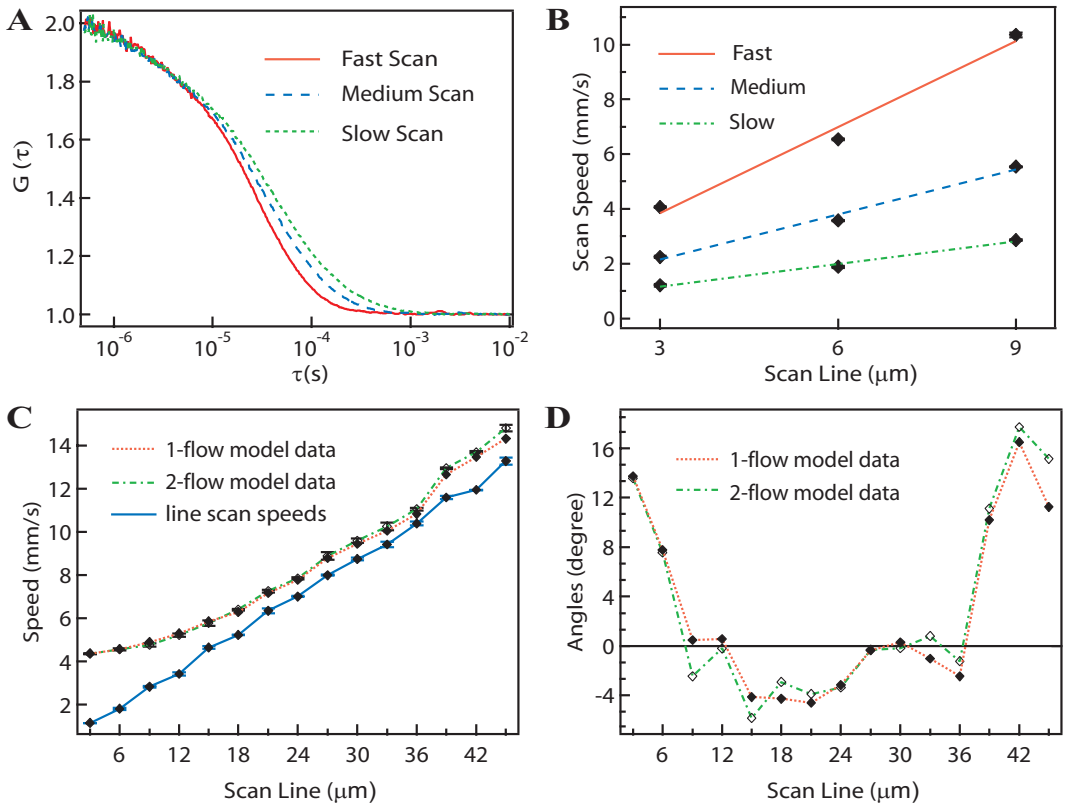

Figure 4.3: A) Three normalized ACF curves for a 3μm-line scan in different scan modes are shown. B) It shows the average line scan speeds of different lengths, such as 3μm, 6μm and 9μm, at different scan modes analyzed by the one-flow model. C) The forward line scan speeds obtained by the two-flow model, and the net speeds by both the one-flow and the two-flow fit model are plotted. D) Flow angles calculated by these three speeds are demonstrated with respect to the different lengths of scan lines.

the data. This is probably due to nonlinear behavior of the scan mirrors at the endpoints of the scan. Nevertheless, in all cases, the ratios of τ_{f1} and τ_{f2} are in good agreement with those of $T_{forward}$ and $T_{backward}$ for fast, medium and slow scan modes as measured by the oscilloscope (Table 1, parenthesis). Therefore, the scan speeds of forward (τ_{f1}) and backward (τ_{f2}) scans can be extracted by the two-flow fit model. To test which model is appropriate for a certain scan mode we calculated the level of significance that the two-flow model represents an actual improvement over the one-flow model by an F-test (34). For the fitting results shown in Table 1, the number of all data points is 550, and there are 6 free parameters for the one-flow fit model (equation 4.2) and 8 free parameters for the two-flow model (equation 4.4) because the structural parameter K was fixed in the fitting. P values from the F-test are calculated as 93.4% for fast, 74.9% for medium and 81.1% for slow scan mode. The fact that the P value is bigger than 90% indicates that the two-flow fit model is applicable for the fast scans. For the medium and slow scans the results show that the necessity of introducing the two-flow model is much less significant and the one-flow model is acceptable for data fitting. This is probably due to their relative large time ratios of forward scans over backward scans. In theory the two-flow model can be simplified into a one-flow model only if $\tau_{f1} \gg \tau_{f2}$, since for this case the temporal intensity fluctuations are mostly caused by τ_{f1}, i.e. by the forward scan. As an experimental verification, the Atto 565 (1 nM) solution was perfused into the microchannel at a pumping rate of 0.8 ml/hr, and the direction of the microchannel was manually adjusted to 0 degree. Slow scan lines perpendicular to the flow axis with different lengths from 3 μm to 45 μm with and without flow were used to measure the net speeds and the scan speeds (figure 4.3C). Flow angles determined by the one-flow and the two-flow models are plotted against the scan lengths (figure 4.3D). From the graph the net speeds obtained by the two-flow

model are almost the same as those by the one-flow model, and the results of flow angles by the two fit models overlap without great differences. This agrees with our previous assumption that the one-flow model is suitable for the scans in medium or slow modes. Therefore, in the following we assume to have only one scan speed for the slow line scans. Furthermore, as flow speeds differ greatly across the microchannel for a large distance, long scan lines (e.g. above 36 μm) yield large measurement errors. Short line scans may be influenced by the nonlinear behavior of the scan mirrors at the endpoints of a scan when the mirror changes scan directions, and the measured flow angles are affected. Lines from 9 μm to 36 μm resolve the flow directions best. The spatial resolution is important for the characterization of the flow velocity profile in a micron-size structure by line scan FCS. However, the accuracy of angle determination is deteriorating as the length of scan line decreases (figure 4.3D). As a compromise we choose a scan line of 3 μm for the optimal resolution and reasonable accuracy of flow profile measurements.

4.4.2 Flow Direction Analysis

For the optimization of line scan FCS, we investigated the influence of relative angles between microfluid flow directions and scan lines on the accuracy of analysis. However, it is demanding in practice to change the flow directions precisely in the microchannel for the current system. Alternatively, rotation of scan lines can be set through the FV300 software provided by Olympus. Slow line scans at 16 different angles between 0 and 360° are executed when the dye solution is stationary in the microchannel or flowing. Corresponding results of laser beam line scan speeds (figure 4.4A) and net speeds (figure 4.4B) are shown in polar graphs, where the length of

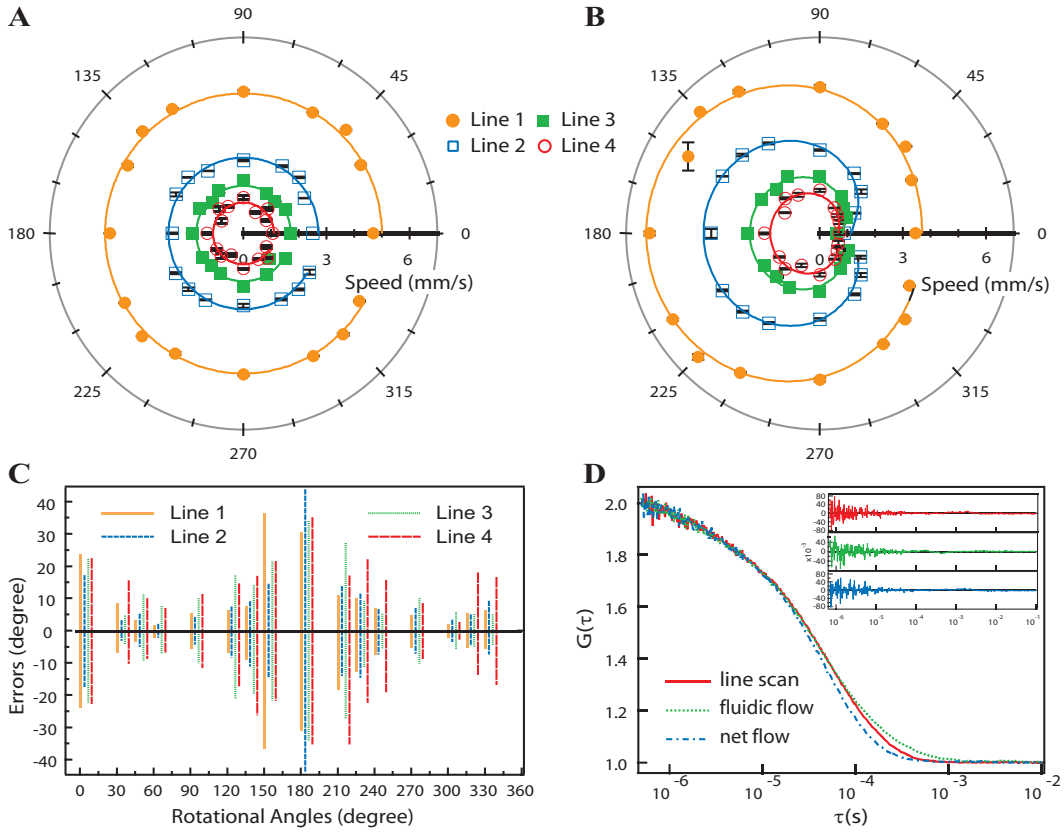

Figure 4.4: Calibrations of flow direction analysis by slow line scan FCS. A) The scanning speeds measured in a stationary sample, and B) the net speeds measured with the pumping rate of 1ml/hr are plotted at 16 rotation angles in the polar graphs for 4 different scan lines. The lengths of line 1, line 2, line 3 and line 4 are 3μm, 6μm, 12μm and 25μm respectively. C) Standard deviation of all measurements is presented. D) Experimental ACF curves of line scan, microfluidic flow and net flow are shown with their respective fitting residues (inset, from top to bottom).

scan line 1 is 3 μm, line 2 is 6 μm, line 3 is 12 μm, and line 4 is 25 μm. The standard deviation of flow directions determined by the 4 scan lines with different lengths in dependence of rotational angle is shown in figure 4.4C. An example of the ACF curves of the laser line scan, microfluidic flow without scanning, and microfluidic flow with line scan are shown in figure 4.4D and the goodness of the fits are confirmed by the residuals. In all measurements the standard deviation is large when the scan line is parallel to the flow axis, while it is relatively small in the range of scanning directions perpendicular to the flow axis.

4.4.3 Scan Length Reduction

In the current setup without access to the control of the scan mirrors, it is possible to acquire selected parts of the fluorescence signal during forward scans as described in Section 3.2. The lengths of scan lines were then effectively reduced from 3 μm to 1.5 μm, 1 μm and 0.5 μm, and the respective ACF curves are shown in figure 4.5. From the data fitting, the scan speed of 3 μm line scan was 0.98±0.07 mm/s, while that of 1.5 μm line scan was 1.22±0.03 mm/s, 1 μm line scan was 1.39±0.16 mm/s, and 0.5 μm line scan was 1.45±0.15 mm/s. The scan speed of the bi-directional line scan of 3 μm was slower than that of single directional line scan of 1.5 μm, which is due to the nonlinear scan effect at line endpoints in forward scans and also the small time fraction of backward scans for line 3 μm. The selection of signals from the central part of the forward scan reduce the influence of non-linear effects at the endpoints of the scan, remove the backward scan contribution, and reduce the scan line and thus increase the spatial resolution of the technique. However, the signal selection also reduces the measurement time and thus the signal collection since signals are only recorded during

a fraction of the total scan.

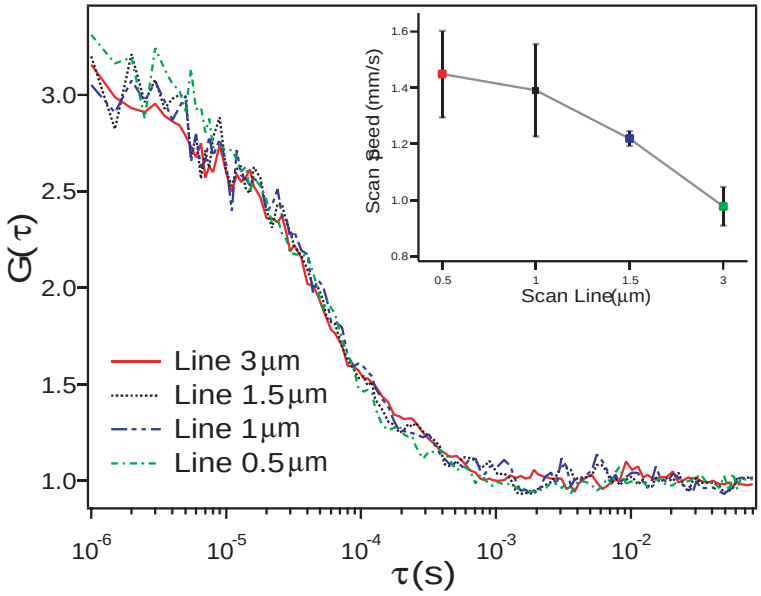

Figure 4.5: ACF curves of 4 scan lines with decreasing lengths (3 μm, 1.5 μm, 1 μm, and 0.5 μm) and the respective increasing line scan speeds (inset). The length of scan line was reduced by partial acquisition of fluorescence fluctuations in forward scans.

4.4.4 Applications

In order to examine the applications in different systems, slow line scans of 3 μm were performed to determine the microfluidic flow directions. We investigated a microchannel with a fiber obstructed in the center (figure 4.2A, d) and measured its flow velocity pattern. In the microchannel, flow around the fiber is constricted to the horizontal plane, which implies the formation of a 2D flow pattern inside. Line scan FCS measurements are performed at 7×14 positions surrounding the fiber with a step size of $30\mu m$ for the determination of the flow profile. Velocity vectors are then calculated and superimposed onto an image of the microchannel (figure 4.2B) where the length of the vector represents flow speed and its arrow indicates flow direction. The resul-

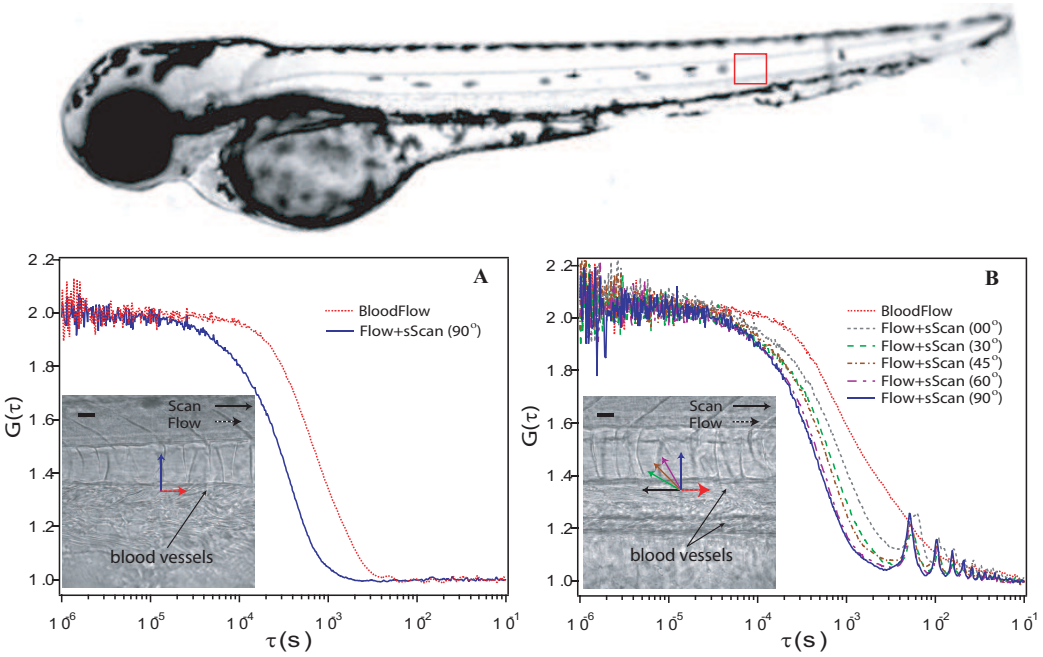

Figure 4.6: Overview of a zebrafish embryo, blood flow was measured by FCS in the trunk part of fish (red box). Normalized ACF curves of zebrafish blood flow and net flow when coupled with line scans at various angles. The respective vectors of scan and flow are shown in insets. A) a blood flow angle of 12.6° was obtained by line scan FCS at 90°; B) the interference of periodic line scan is shown as peaks in ACF curve for some special cases. The solid lines in the inset represent the effective scan vectors at different angles, from 0°, 30°, 45°, 60° to 90° (clockwise).

tant figure of the obstruction microfluid velocity profile is qualitatively consistent with that obtained by PIV (16). Another application of line scan FCS is realized in small blood vessels of living zebrafish tissue. Potentially this is a label-free method since the autofluorescence of flowing proteins and red blood cells in zebrafish blood provides sufficient signal fluctuations for FCS measurements. It should be noted that nanomolar concentrations of a fluorophore can be injected into zebrafish embryos in an early developmental stage (13) when no red blood cells exist in order to allow FCS measurements. This still has a strong advantage over PIV since small concentrations of fluorophores are unlikely to block small vessels. In the experiments, the blood vessel of immobilized zebrafish on the microscopic stage was aligned to be horizontal; the schematic vectors for blood flow and line scans are superimposed onto a transmitted image (figure 4.6A and B). Single point FCS and slow line scan (90°) FCS were performed and all the data were fit with the two-flow model. A two-flow model has to be used for adequate fitting since there are alternating slow and fast blood flows in the zebrafish cardiac cycle stemming from systolic and diastolic periods. In combination with the slow line scan, which can be treated as a single flow as shown earlier, this leads to two alternating flow patterns determined by the slow line scan overlaid with either the systolic or diastolic flow speed. The flow angle was calculated to 12.6° using the equation 5 (figure 4.6A). A problem arises for this method in cases where there are obstructions in the scanning path as for instance a blood vessel wall. For this case a periodic signal will be seen in the ACF and the fitting of the data is difficult or even impossible especially if the obstruction should have a slow movement itself. However, the scanning period is in the range of milliseconds or more, hence, on the timescale it will not contribute to the width of the ACF curve of the diffusion plus flow. Therefore by recording slow line scan FCS at different rotation angles (0°, 30°, 45°, 60°, and 90°)

the blood flow direction can still be determined (figure 4.6B). In this example the ACF possesses its greatest width at a scan angle of 0° indicating that the flow is horizontal as expected. Scanning in multiple directions thus allows measurements of flow profiles even in small blood vessels and close to obstructions and vessel walls. In addition, this approach is independent of the focal dimensions which can be strongly distorted in tissues. As a last point it should be noted that the measured ACFs contain as well periodic fluctuations in the second timescale due to the heart rate of the organisms (data not shown). While this is not of interest in the flow profile measurements it allows the accurate online monitoring of the heart beat frequency of the organism measured.

4.4.5 Discussion

The spatial resolution of line scan FCS was limited by the length of scan lines, and also affected by the inherent nonlinear behavior of scanning mirror mechanism at line endpoints. This problem could be solved as shown in the section 4.3.1 by using fluorescence signals collected during a specific phase of the line scan, although that reduces signal collection time and might increase the necessary measurement time. A critical drawback of the combined system lies in the fixed time ratios of forward and backward line scans as fixed by the commercial system FV300, which makes available a few line scan speeds. Optimized ratios, which minimize the deviation of the measurements from a one-flow model and have small nonlinearities at the scan end points, could be achieved by the direct control of the scanning mirrors. In that case, the spatial resolution of line scan FCS for characterization of flow profiles might be improved further. The advantage of FCS over other methods is that only a low concentration (~1 nM) and small size molecules is required, and thus clogging of channels and blood

vessels as can happen with PIV is not a problem. This means as well that this technique can be used in nanoscale channels too small to allow PIV measurements with microbeads. Importantly, the method works for the measurements in blood vessels when auto-fluorescence is high enough. Asymmetric focus FCS requires the distortion of the focal volume interfering with the imaging capabilities of the microscope and it is ambiguous since opposite flow directions cannot be resolved and difficult to be applied to tissue measurements. Dual-beam FCS requires the installation of an extra pinhole in the instrument. In contrast to these two techniques line scan FCS can be implemented on any commercial or custom-built confocal microscope system based on a simple modification without interference in the imaging capabilities. In addition by scanning the laser focus using a piezo actuator in the z-direction, the presented method can be extended for measurements of 3D microfluidic flow velocities (chapter 6). The combination system could thus allow 3D flow to be locally measured in the context of structural features which is important to easily correlate the flow environments with particular cells or tissue structures in small animal bodies. This feature also has a potential application in tissue engineering to optimize the fluidic culture system.

4.5 Conclusion

In this chapter, we performed line scan FCS experiments on the FCM and demonstrated its applications in the analysis of flow profiles in microchannels, and its feasibility of flow direction determination in living zebrafish blood vessels. The accuracy of line scan FCS was assessed in dependence of i) the angle between scanning direction and flow, ii) the scan speed, and iii) the scan length used in the experiments. We have chosen a line scan length of 3 μm as a compromise between spatial resolution and

measurement accuracy. However, the spatial resolution can be improved to 0.5 μm using the algorithm for selective scan length reduction. With current setup, measurement errors can be as low as $\pm 10^{\circ}$. Furthermore, the potential extension of the method for 3D microfluidic flow velocities will be addressed in chapter 6. Hence, line scan FCS is a good non-invasive alternative which minimizes disturbances of flow profile in many applications. The combination of imaging and spectroscopy tools also facilitates precise positioning of measurement points inside a microstructure with complicated geometry, such as fluidic microchannels, cell-culture microstructures and biological tissues. Thus, line scan FCS could be a very useful tool for the characterization of their flow profiles. In the next chapter, the application of line scan FCS in tissue engineering and developmental biology is discussed.

Chapter 5

Application in Tissue Engineering and Developmental Biology

5.1 Liver Tissue Engineering

5.1.1 Introduction

The liver is the largest gland and most important organ in the body, lying on the right side of the abdominal cavity beneath the diaphragm. It serves a variety of functions, such as vascular, metabolic, secretory and excretory. In metabolism, the liver plays a central role in energy homeostasis, nitrogen excretion, water regulation between the blood and tissues, and detoxification. Hepatic blood microcirculation plays an important role in the above functions (118). The blood of liver is supplied by both the hepatic artery and the portal vein. It empties into the inferior vena cava through the right, middle and left major hepatic veins. Portal veins and hepatic arteries run parallel in the portal canals, and the distributing portal veins repeatedly terminate in smaller

branches which connect with sinusoids (119). The whole liver has quite a large number of similar functional units, the classic hepatic lobule, which is a polygonal structure surrounded by small branches of hepatic artery and portal vein. The hepatic lobule is a complex heterogeneous network of sinusoids. Most blood enters into it from portal veins, through the sinusoids network, and then drains into the central veins, the central axis of hepatic lobule. Blood from central veins runs into the hepatic veins, and is finally collected by the inferior vena cava. Sinusoids are the specialized capillaries in the liver, with the diameters ranging from 6 μm to 16 μm (120). Sinusoids are composed of endothelial cells (SECs), Kupffer cells, Ito cells and ”Pit” cells. The sinusoid wall is lined with a sieve plate of endothelial cell fenestrae, most of which are 100 to 150 nm in diameter. Kupffer cells are macrophages anchored to the luminal surface of sinusoids, ”Pit” cells are immunoreactive cells in the sinusoidal lumen, while Ito cells are positioned in the space of Disse, under the endothelial lining plate, close to liver parenchymal cells (121). The hepatic sinusoid is the principal site where the exchange between the blood and parenchymal cells occurs, i.e. exchange of oxygen and nutrients with parenchyma, and removal of metabolites and waste products. The elastic red blood cells (RBCs) can move smoothly along the sinusoids unless the lumen is reduced to near zero (122). In this case, the velocity of RBCs could be a good indicator of the sinusoidal blood flow *in vivo*. Cells like SECs and Kupffer cells could locally produce some chemical factors. The sinusoidal lining cells have been reported to respond to these factors, followed by either their relaxation or contraction. The blood flow (acts as shear stress) in sinusoids has a significant impact on the functions of lining cells, which could influence the sinusoidal blood flow through some chemical factors. It has been reported that the sinusoidal endothelial cells experience more hemo-dynamic forces after liver partial hepatectomy. The increased blood flow will

induce the morphology change of lining endothelial cells (123). The shear stress imposed on SECs would additionally have molecular and ultrastructural effects on these cells by expressing molecular factors within minutes. Current studies suggest that NO induced by the shear stress is a trigger for the expression of genes participating in the liver regeneration (124). Vascular endothelial cell growth factor (VEGF) receptors (VEGFRs), affected by shear stress, are of great importance for liver regeneration. It has been observed that the numbers of VEGFR-1 and VEGFR-2 increase after liver resection (125). The shear stress promotes the formation of a complex of VEGFR-2, VE-cadherin and β-catenin, which is assumed to act as a shear stress receptor. A group of researchers have demonstrated that the shear stress on SECs in vitro increases the mRNA levels of VEGFR-2, VE-cadherin, and β-catenin. In conclusion, it has been shown that the blood flow, and consequently shear stress from both *in vivo* and *in vitro* sources has significant influence on morphology and functions of sinusoidal endothelial cells. Although the hepatocytes are not experiencing the blood flow directly, it has been shown that the functions, such as albumin and urea synthesis, of hepatocytes cocultured with 3T3-J2 fibroblasts in microchannels are greater when imposed to low shear stress compared to high shear stress (126).

The microfluidic flow is proved to be an important factor in liver tissue engineering as well. Well-known liver diseases including hepatitis, cirrhosis, haemochromatosis, and liver cancer are common diseases in the Asia Pacific region. Liver tissue engineering aims to restore liver functions *in vitro* in order to study the construct for liver regeneration and drug discovery. There are currently three liver *in vitro* models available for the scientists for research. The first one is the isolated perfused rat liver (IPRL) model which is used to investigate the physiology and pathophysiology of the rat liver (127); the second one is liver slice intra-tissue perfusion system which is simple and easy to

maintain in tissue culture (128; 129); followed by the 3D liver cell perfusion culture system in a complex microfluidic channel which maintains the 3D cellular morphology, interaction and functionality (8). All the three perfusion models are developed to study the viability and functionality of liver cells. Therefore, it is necessary to optimize the performance of perfusion systems. The microfluidic flow velocity is one of most important parameters which affects the shear stress applied to the cells in the perfusion system. The IPRL *in vitro* model provides access to the cellular injury and liver functions close to the *in vivo* model. The concept of IPRL is to perfuse the culture medium through the portal vein into the whole sinusoid network of the liver, in order to maintain its viability in the long term. This model is similar to the *in vivo* environment and does not break the internal cellular structure of liver which is supposed to maintain the original functionality of liver outside the animal body. This is a good research platform for liver transplantation and additionally helpful for liver tissue engineering which aims to re-establish the liver function in an engineered environment.

The liver slice perfusion system was started in 1923 by Otto Warburg and is currently carried out with a great variety of methods (128). Its concept is to use a precision slice-cutting machine to prepare tissue slices with reproducible thickness and culture them in medium. However, most of these methods are limited because of insufficient oxygen diffusion and mass transfer to the slices. Therefore, a novel intra-tissue perfusion (ITP) system was proposed by Khong and Yu to increase the delivery of medium into the liver tissue and improve the even distribution of medium throughout the tissue (129). Microfluidic channels are used for the multiplexing of drug testing platforms due to the efficient and high throughput cellular analysis (130). However, most of the cellular microfluidic systems are limited to 2D cell culture and lack the 3D environment for cell-cell and cell-matrix interactions. Our collaborator (Toh and Yu) has de-

veloped a novel 3D mammalian cell perfusion-culture system in microfluidic channels for maximal cell-cell interaction (8). In the above three perfusion culture models, flow velocity is a key parameter to understand the mechanical effect of perfusion medium on the viability of cells. The mechanical forces induced by the shear stress regulates the morphology of growing cells and their functionality. In this section, point FCS and line scan FCS are implemented to measure the flow velocities in the three perfusion systems. The results will eventually help to optimize and improve the perfusion performance.

5.1.2 Materials and Methods

5.1.2.1 Isolated Rat Liver and Its Perfusion

Male Wistar rats (weight of approximately 250 - 300g) were kept in the Animal Holding Unit at the National University of Singapore (NUS). They were anaesthetized using pentabarbitone sodium (0.1mL/100g, Nembutal®, Abbott Laboratories, Parramatta, NSW, Australia) during the surgery and injected with 0.5mL heparin (Leo Pharmaceuticals, Ballerup, Denmark). In order to fix the whole liver for precision-cut, the rat livers were perfused with sterile 1x PBS solution after the chest-opening for 10 minutes. Subsequently, they were isolated from the rat body cautiously, and were perfused with 4% PFA for 15 minutes for fixation. A liver lobule with smaller size was chosen and cut out for the isolated liver perfusion.

5.1.2.2 Rat Liver Slice Perfusion

Male Wistar rats (weight of approximately 250 - 300 g) were obtained from Animal Holding Unit of the the National University of Singapore and were anaesthetized using

pentobarbitone sodium (0.1 mL / 100 g, Nembutal®, Abbott Laboratories, Parramatta, NSW, Australia) and injected with 0.5 mL heparin (Leo Pharmaceuticals, Ballerup, Denmark). Livers were perfused with 4°C UW solution (Viaspan, Bristol-Myers-Squibb, Princeton, NJ, USA) for live culture or 3.7% para-formaldehyde at 37°C for 1 hr and excised. Tissue cylinders from liver samples were prepared using an 8 mm diameter coring-tool on a motor-driven tissue coring-device (Alabama Research and Development, Bad Homburg, Germany). Liver slices were precision-cut to the desired thickness: 300 μm using a Krumdieck slicer (Krumdieck et al, 1980) (Alabama Research and Development, Bad Homburg, Germany) or 2 mm (or 1.6 mm livers slices used for live culture due to tissue swelling after cutting) using a vibratome (DTK-1000, Pelco International, Redding, USA) in 4°C oxygenated UW solution. More details of experimental setup can be found in this paper (129).

5.1.2.3 3D Microfluidic Channel-based Cell Culture System

Microfluidic channels with micropillar array were designed using AutoCAD (Autodesk, USA) and L-Edit v10.20 (Tanner Research, USA). The dimensions of the microfluidic channel were 1 cm (length) $\times$ 600 μm (width) $\times$ 100 μm (height) and had 3 inlets and 3 outlets. An array of 30 $\mu m \times 50$ μm elliptical micropillars with a 20 μm gap size was situated in the middle of the microfluidic channel, bounding a cell residence volume that was 200 μm wide. Silicon templates were fabricated by standard deep reactive ion etching (DRIE) process19 (Oxford Instruments Plc, UK). The microfluidic channels were then obtained by replica molding polydimethylsiloxane (PDMS) (Dow Corning, USA) on the silicon templates. The PDMS structures were oxidized in oxygen plasma for 1 minute (125 W, 13.5 MHz, 50 sccm, and 40 millitorr) for irreversible chemical bonding to glass coverslips before connecting to fluidic components

(Upchurch, USA). The center inlet of the microfluidic channel was connected to a cell reservoir, which comprised of a 4-way valve with 3 Luer connections (Cole-Palmer, USA) coupled to a 25G stainless steel hypodermic tubing (Becton-Dickinson, USA), to permit the independent introduction of cell suspension and polyelectrolytes via the center inlet. The entire set-up was sterilized by autoclaving at 105 °C for 30 minutes. Cell immobilization was initiated by withdrawing the cell suspension from the cell reservoir, via the 2 side outlets, using a withdrawal syringe pump (Cole-Parmer, USA) with the center outlet kept closed. Laminar flow complex coacervation was implemented by simultaneously infusing a pair of polyelectrolytes via the center and 2 side outlets with syringe pumps. Upon the formation of the 3D complex coacervated matrix, excess polyelectrolytes were displaced by culture medium infused from the side inlets. All 3 outlets were opened during perfusion culture of cells. After the perfusion of cells into the microfluidic channel, the cells are fixed by 4% PFA for the measurement of flow velocity. More details of the setup can found in this paper (8).

5.1.3 Results and Discussion

5.1.3.1 Flow Measurement in an Isolated Perfused Liver

The isolated liver lobule was placed in a customized glass-bottom petri dish (60 mm). The syringe-pump based perfusion system was connected to the portal vein of liver lobule through a 30G needle (Figure 5.1). The liver lobule was covered in the petri dish so that its surface was close to the bottom glass for the better optical observation. The optical instrument for FCS flow measurement was described in the chapter 3. A confocal LSM image of autofluorescence from hepatocyte was first captured to locate the position of sinusoids (Figure 5.2). Then, a particular sinusoid was selected for

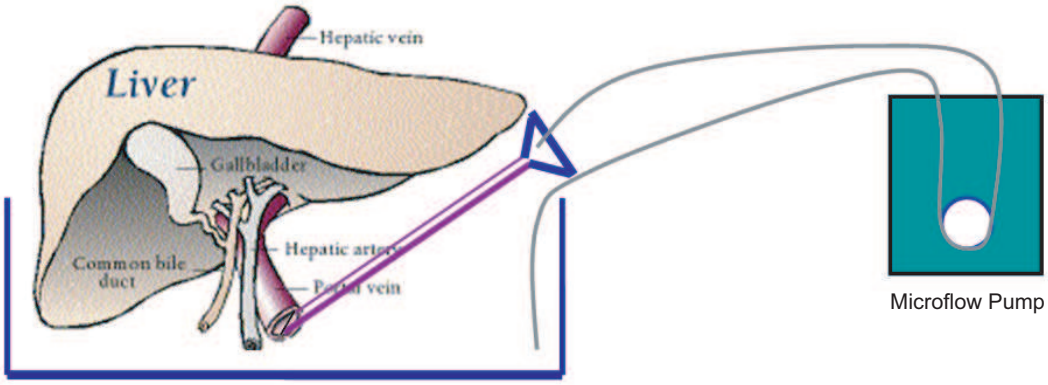

Figure 5.1: Schematic setup of a perfused isolated liver system

the flow measurement as the syringe pump stopped. The measurement was repeated at the same position as the syringe pump was running with the perfusion of Atto 565 (5 nM) solution. Therefore, two FCS flow measurements were recorded: the isolated liver lobule was not perfused in one case, and perfused in the other. As shown in figure 5.2, the ACF curve with perfusion has a left-shift effect compared with that without perfusion, which reflects the shorter dwelling time of Atto 565 molecules in the sinusoid. The result clearly shows that the solution perfusion within the isolated liver lobule can be detected by point FCS, although there exist strong autofluorescence signals from hepatocytes in the liver. The measurement implies the great potential application of point FCS for the optimization of isolated perfused liver model.

5.1.3.2 Perfusion Characterization of Isolated Liver Slices

An open intra-tissue perfusion system was designed and a 30G needle was inserted into the center of a 1.6 mm tissue block (Figure 5.3). A PDMS block with a open side and a perforated side was used as a tissue slice holder to support the needle in place for perfusion. The perfusion solution was 5nM Atto 565 in 1× PBS buffer.

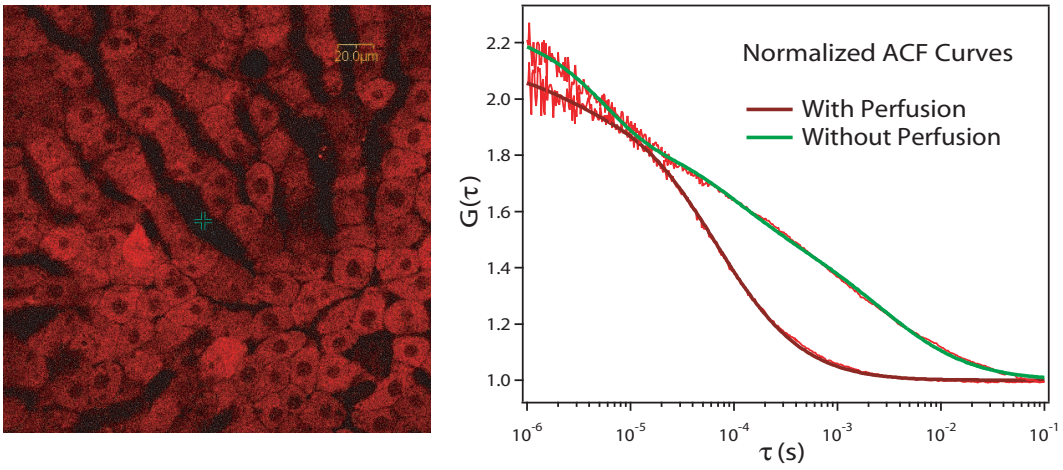

Figure 5.2: A confocal LSM image of isolated perfused liver, the signal is from the autofluorescence of hepatocytes. Additionally, the ACF curves of FCS flow measurements are shown when the perfusion is present and absent in the sinusoid network.

The position of FCS measurement point was determined in a sinusoid of liver slice with the reference of a confocal LSM image of hepatocytes (Figure 5.4A), and flow measurements were performed with and without perfusion. For a comparison, FCS measurement was additionally implemented when there was no perfusion but with line scans. The results of ACF curves were shown in figure 5.4 B and C. The flow of perfusion solution was measured by FCS as the ACF curve shifted to the left compared with that of no perfusion (Figure 5.4B). This result was verified by the measurement of fast and slow line scan FCS (Figure 5.4C). As discussed in the chapter 3, the line scan of confocal LSM system can be treated as artificial flow generated on the static solution. It confirms that the perfusion of a liver slice can be characterized by point FCS flow measurements.

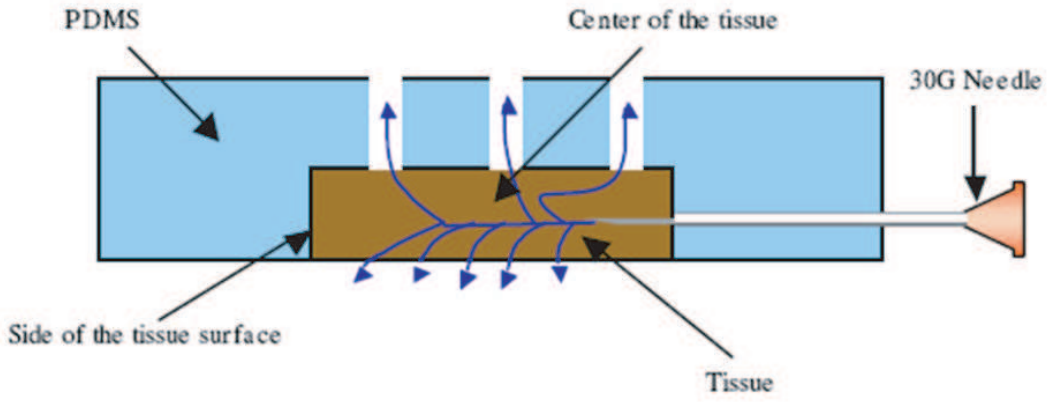

Figure 5.3: Schematic setup of a perfused liver slice system

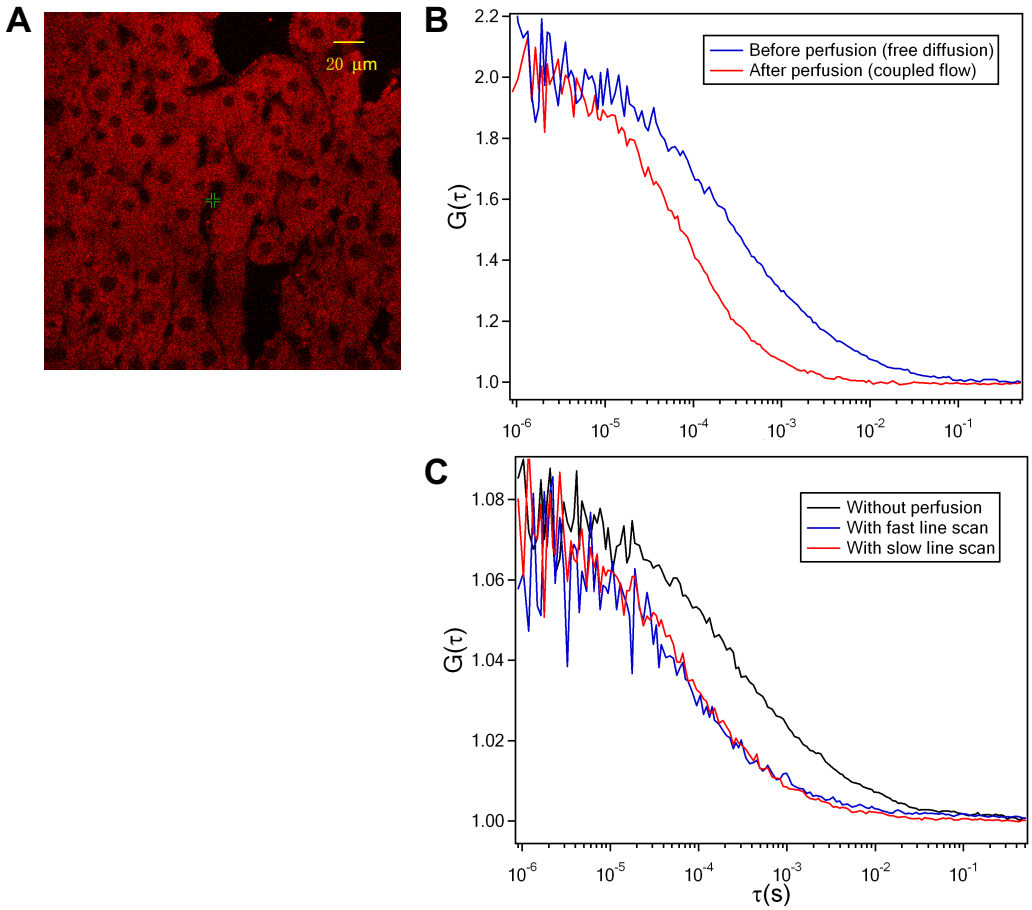

Figure 5.4: A) The CLSM image of autofluorescent liver slice; B) ACF curves of FCS flow measurements with and without perfusion; C) ACF curves of FCS flow measurements with fast and slow line scans and without line scan

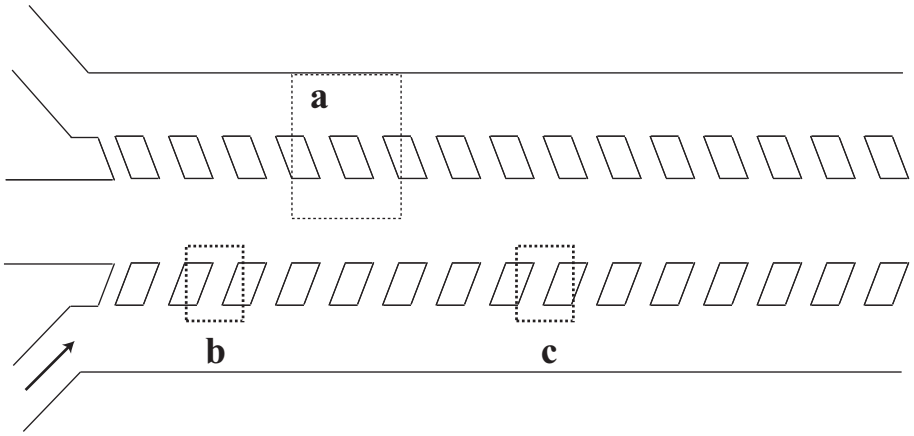

Figure 5.5: Schematic representation of a microfluidic channel with micropillars for cell culture. The center channel is used to immobilize the cells and the two side channels are mainly designed for culture medium perfusion.

5.1.3.3 3D Microfluidic Channel-based Cell Culture System

Line scan FCS was used to characterize the microfluidic flow properties in the complex microchannel with micropillars. This microfluidic model has three inlets, and solution is pumped into the microchannel through the bottom inlet with the top and central ones blocked (Figure 5.5, arrow). Measurements by single point FCS were implemented in a region near the center of the microchannel (Figure 5.5a) to acquire a profile of flow speeds (data not shown) based on 10×15 data points with spatial resolution of 10 μm. As expected, the flow speed reached a maximum in the center of each sub-microchannel, and became near zero around and in between the micropillars. However, the flow speed profile did not provide any information about flow directions around the micropillars, which was an important parameter to understand the microchannel structure and its behavior in microfluidics. Therefore, line scan FCS was applied to study the microfluidic flow. The micropillars did not extend over the full height of the microchannel and it was assumed that the solution between two mi-

cropillars will be guided along the direction of the micropillar long axis, while the fluid below the micropillar tips followed the perfusion direction. Hence, we measured the flow directions around the micropillars at different heights, H1 = 20 μm below the micropillars and H2 = 40 μm near the micropillar tips, taking the bottom glass surface of the microchannel as a zero position reference. Figure 5.6A shows measurement results in a near inlet area (Figure 5.5b) and figure 5.6B those in a central area (Figure 5.5c) with a step size of 10 μm. Microfluidic flow follows its perfusion direction at the height H1, and bends toward the direction of the channel when it approaches the micropillar tips at the height H2 (Figure 5.6A). Furthermore, the solution was observed to flow slowly and horizontally in the central region (Figure 5.5c) along the aligned microchannel, and the flow directions are not greatly influenced by the micropillars (Figure 5.6B). Additionally, the comparison of the microfluidic flow velocity near the inlet (Figure 5.5b) with that in the central part (Figure 5.5c) is shown in figure 5.6C for the height H1 (inset, asterisk), and in figure 5.6D for the height H2 (inset, asterisk). An interesting observation is that microfluidic flow slowed down between micropillars (Figure 5.6C). This phenomenon was more obvious in the central region (Figure 5.6D) of the microchannel. This lack of flow across the micropillar gaps might constitute a serious problem when, for instance, proper perfusion for cell cultures is needed.

The same measurement by line scan FCS was implemented in the microfluidic channel with hepatocytes culturing in the center channel. The objective of this work was to investigate the flow profile of regions close to the cells which might have induced mechanical effects on the growth of hepatocytes. As described previously, all the hepatocytes in the channel were fixed before the medium perfusion and FCS flow measurements. As shown in figure 5.7A, the medium was perfused into the microchannel through two inlets (arrows), and the hepatocytes were placed in the center channel.

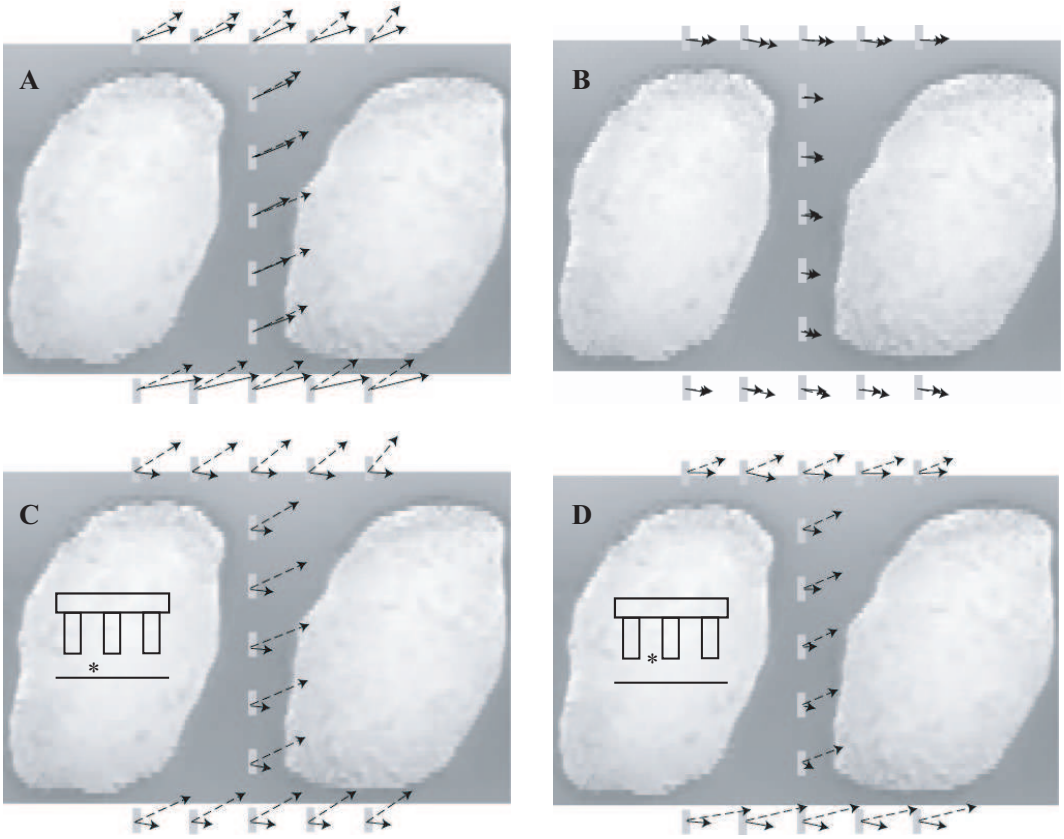

Figure 5.6: A) Velocity vectors measured at the height H1 (20 μm, dash line) and H2 (40 μm, solid line) are shown for the near inlet area; and B) Velocity vectors for the central region; C) Comparisons between velocities of the near inlet area (dash line) and the central region (solid line) are demonstrated at the height H1 (inset, asterisk); and D) the same comparison of velocities at the height H2 (inset, asterisk). (Gray bar: scan line)

The flow velocity measurement by point and line scan FCS was performed in a central region near the micropillars (Figure 5.7A, red dash box), the results of flow velocity vectors were superimposed on a CLSM image of the microfluidic channel with stained hepatocytes (Figure 5.7B). The length and direction of these vectors represents the amplitude and direction of flow velocity measured at that position. As shown, flow velocity is near zero (crossing in the figure) at the positions close to cells and near the micropillars, and increases when the measurement point is moved away from the micropillars until it is almost parallel to the direction of side channel. The result by line scan FCS suggests that the oxygen and mass transfer at the central region of microchannel is dominated by thermal diffusion, and independent on the flow rate of the perfusion medium. This measurement result has a significant impact on the further improvement of microfluidic channel perfusion system.

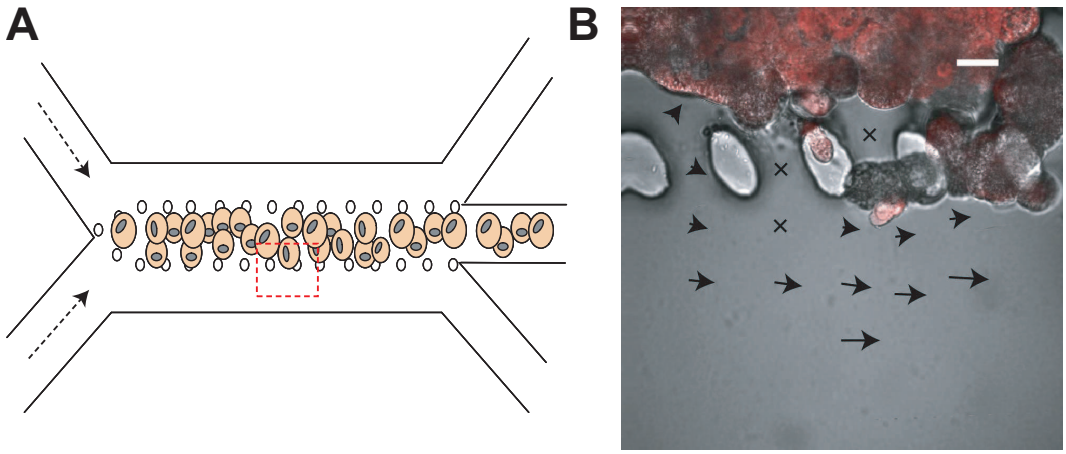

Figure 5.7: A) Schematic representation of a perfused microfluidic channel with micropillars, and hepatocytes are immobilized in the center channel; B) The flow velocity vectors measured by line scan FCS are presented with a CLSM image of the microchannel. Bar: 20μm.

5.1.4 Conclusion

There are three typical culture models in liver tissue engineering such as isolated perfused liver, perfused liver slice and microfluidic cell-culture channel. All the three models are related to medium perfusion for the purpose of cell culture. Therefore, it is important to understand the flow velocity property inside the microfluidic models. FCS is one of the non-invasive optical methods able to provide the information of microfluidic flow velocity in the liver organ, slice and microchannels. Additionally, line scan FCS measures the direction of flow velocity in the models which is an outstanding feature. The quantitative characterization of shear stress of microfluidic flow and the high spatial resolution demonstrated to be 0.5 μm in chapter 3 make line scan FCS a great tool for the flow measurement in cell biology and tissue engineering.

5.2 Developmental Biology

5.2.1 Introduction

The zebrafish *Danio rerio* is a widely accepted animal model to study the development and function of the vascular system (12). One of the reasons is that it shares genetic similarity to mammals. Furthermore, the small size and optical transparency of zebrafish allow to do experimental analysis of the vascular system at different development stages. Previously, normal pattern of vascular anatomy of developing zebrafish has been obtained using confocal microangiography (13). This can be used as a reference to detect mutations, genetic perturbation analysis, and cross-species comparison by observing severe abnormal morphology during development. However, it is still difficult to quantify the consequent functional defects in this case. A non-invasive

method is required to measure the difference of blood flow as a quantitative indicator, which can also serve as a good reference data for shear stress generated by the blood flow on the endothelial cells along the blood vessels. An optical-microscope-based technique like line scan CLSM was used to measure the cardiovascular blood flow in mice embryo (20) and zebrafish embryo (21). In these papers, CLSM images of flowing red blood cells (RBCs) through the vessels were acquired by continuous line scans and the displacement of RBCs were detected using software programs. The velocity of RBCs were then calculated based on the duration time and their displacements. The advantage of this method is the high temporal resolution of flow velocity profiles, but it is limited in the low spatial resolution which is a key factor to understand the local changes of blood flow in the vessels. FCS was demonstrated to measure blood flow in trunk blood vessel of zebrafish embryo with high spatial resolution of $0.5\mu m$ in the chapter 4.

The development of blood circulation system relies on a complex set of signals including genetic factors and mechanical forces. For example, the abnormality of cardiovascular systems in growth and development is one of a range of common birth defects (131). Additionally, both *in vitro* and *in vivo* experiments have implied that mechanical signal such as shear stress induced by blood flow is essential for normal circulation development (132; 133). However, a large gap exists between the regulated blood flow and a quantitative evaluation measurement. The information on blood flow collected by the method would benefit the research of blood circulation and assist the understanding of development of local blood circulation network such as liver sinusoid growth. Using the transgenic zebrafish line with GFP expressed in endothelial cells (fli1:GFP), the blood vessels of liver during development can be visualized by any fluorescence or confocal microscope. Liver vascular development has been ver-

ified by the formation of blood vessels at different development stages, but the time point when the blood circulation starts is yet to be shown. Therefore, an instrument with both capabilities of confocal imaging and flow measurement is essential for the study.

In this section, the FCM system was used to measure the blood flow in liver sinusoid network of zebrafish embryo at different development stages. The dependence of flow velocity on the diameter and penetrating depth of blood vessels was also demonstrated. Additionally, a spatial flow profile in the trunk blood vessel was shown by FCM which agrees with the theoretical simulated flow velocity profile in a cylinder tube. This suggests that FCS is a method with high spatial resolution especially for *in vivo* blood flow measurements in small blood vessels.

5.2.2 Materials and Methods

Zebrafish were maintained in the fish facilities at the Institute of Molecular and Cell Biology of Singapore according to established protocols (115) and in compliance with Institutional Animal Care and Use Committee (IACUC) guidelines. Developmental stages were presented in hours post fertilization (hpf), days post fertilization (dpf) or month post fertilization (mpf). Briefly, a pair of AB wild-type zebrafish was crossed and their embryos were collected the next morning. The embryos were then incubated in egg water ($60\mu g/ml$, Instant Ocean® Sea Salts (Aquarium Systems, Inc.)) at $28.5°C$ for the optimal development, and after 20 hpf PTU (0.003% 1-phenyl-2-thiourea in 10% Hank's saline, Invitrogen, Singapore) was added to prevent pigmentation. Embryos were dechorionated at the time of 55 hours and then anaesthetized by Tricaine (ethyl m-aminobenzoate, Sigma, Singapore). The treated embryos were

mounted in 0.5% low melting temperature agarose (Invitrogen, Singapore) in a WillCo-dish® glass bottom dishes (GW-3512, WillCo-Wells, The Netherlands) for the following measurements. It has been shown that in stable Tg(fli1:EGFP) zebrafish, the fli1 promoter is able to drive expression of enhanced green fluorescent protein (EGFP) in all blood vessels throughout embryogenesis (134). This zebrafish line is suitable for blood flow measurements as the location of blood vessels can be easily identified through CLSM images of GFP expressed at the positions (Figure 5.10).

5.2.3 Results and Discussion

5.2.3.1 Spatial Flow Profile in a Blood Vessel

A 3-day zebrafish embryo was mounted in the petri dish at lateral view. Blood flow measurement by FCS was implemented in the dorsal aorta and cardinal vein near the trunk of fish (see figure 4.6). As discussed in the chapter 3, the diastolic and systolic flow velocities in both artery and vein can be measured by FCS using a two-flow model (equation 4.4). Blood flow velocities were measured at different locations across the blood vessel with a step size of 3 μm. The flow profiles in the dorsal aorta and cardinal vein were then plotted in figure 5.8. A comparison of diastolic flow velocities in both dorsal aorta and cardinal vein is shown in figure 5.8 A and that of systolic flow velocities in figure 5.8 B. As demonstrated, the flow velocity is found to be its maximum in the center of blood vessels for both diastolic and systolic flow and the flow velocities are close to zero near the wall of blood vessels, which fits with the prediction from theoretical calculation in a cylindrical tube. The parabolic profile of blood flow is verified by the flow measurement by FCS. In the figures, it is found that the velocity of systolic flow is faster than that of diastolic flow in both blood vessels.

Furthermore, the velocity of either systolic and diastolic flow in dorsal aorta is faster than those in the cardinal vein. This is reasonable because the blood is pumping out from the heart, going through the artery network, and returning back to the heart from the vein network. The measurement of spatial flow profile in zebrafish blood vessels has a significant meaning in the characterization of local blood flow and its mechanical effect on the surrounding endothelial cells due to its high spatial resolution.

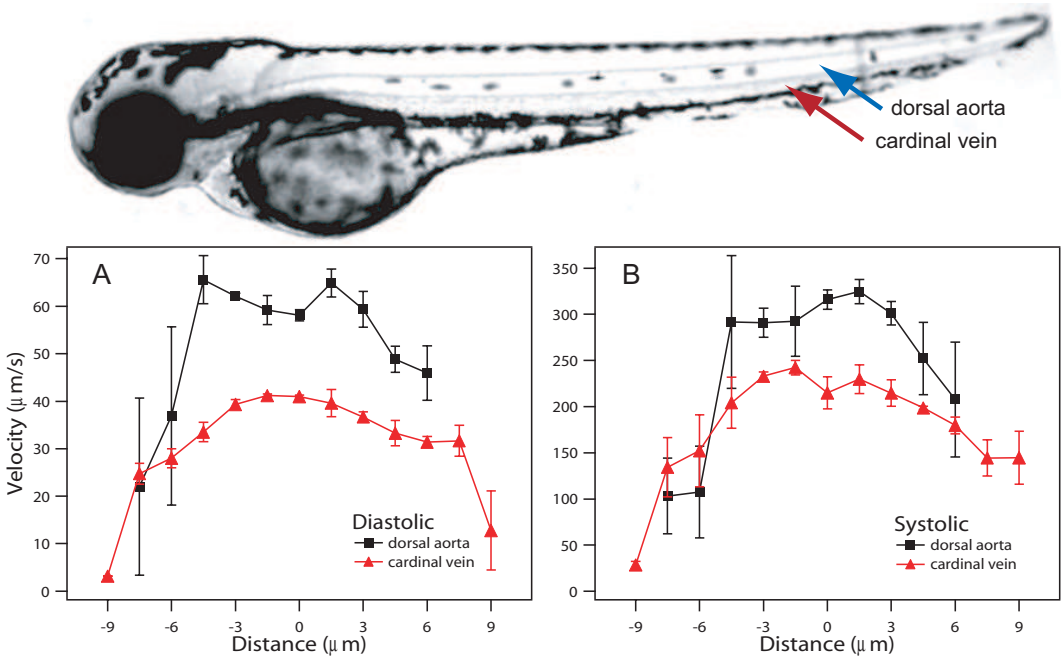

Figure 5.8: A) Blood flow velocity profile in a dorsal aorta (black) and a cardinal vein (red) at the heart diastolic period; B) Blood flow velocity profile in a dorsal aorta (black) and a cardinal vein (red) at the heart systolic period.

5.2.3.2 Velocity Measurement of Sinusoidal Blood Flow

The vascular development in liver is of great interest to liver development research. As is known, the sinusoid network is first formed as a few large blood vessels, which then penetrate into the whole lobules of liver during the development. The penetrating

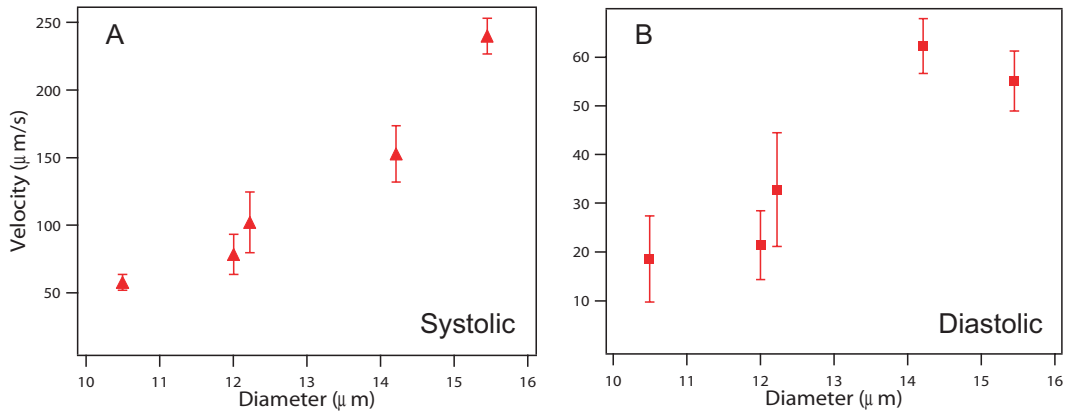

Figure 5.9: A) Systolic and B) Diastolic blood flow velocity is plotted against the diameter of blood vessels in the developing liver.

vessels are small in diameter and deep in position compared with the initial formed large vessels. The flow velocity in large vessels is believed to be faster than that in small vessels because the blood flow network is growing from large vessels to small ones. With the FCM instrument, it is feasible to locate the blood vessel position in the liver and measure its diameter. Meanwhile, the flow velocity was measured and its relationship with depth and diameter of blood vessels was investigated. In figure 5.9A, the measured systolic flow increased when the diameter of blood vessels get larger, similar results apply to the diastolic flow which was shown in figure 5.9B. This verifies the prediction of faster flow in larger vessels in a developing liver organ of zebrafish embryo. Additionally, the flow velocities of blood can be measured in blood vessels at 8 different penetrating depth of liver. All ACF curves and their fittings were shown in figure 5.10A, and the measured flow velocities were plotted in figure 5.10B. This is another verification of the dependence of flow velocity on the vessel diameter, because the deeper the blood vessels penetrates, the smaller its size. As shown in figure 5.10B, the blood flow velocity gradually decreases when the measurement position is deep inside the developing liver. The implication here is that during the initial development

stage of liver, a few blood vessels penetrate into the liver without any blood circulation, FCS in this case can be used to study the flow velocity difference so as to investigate the functionality of liver sinusoids.

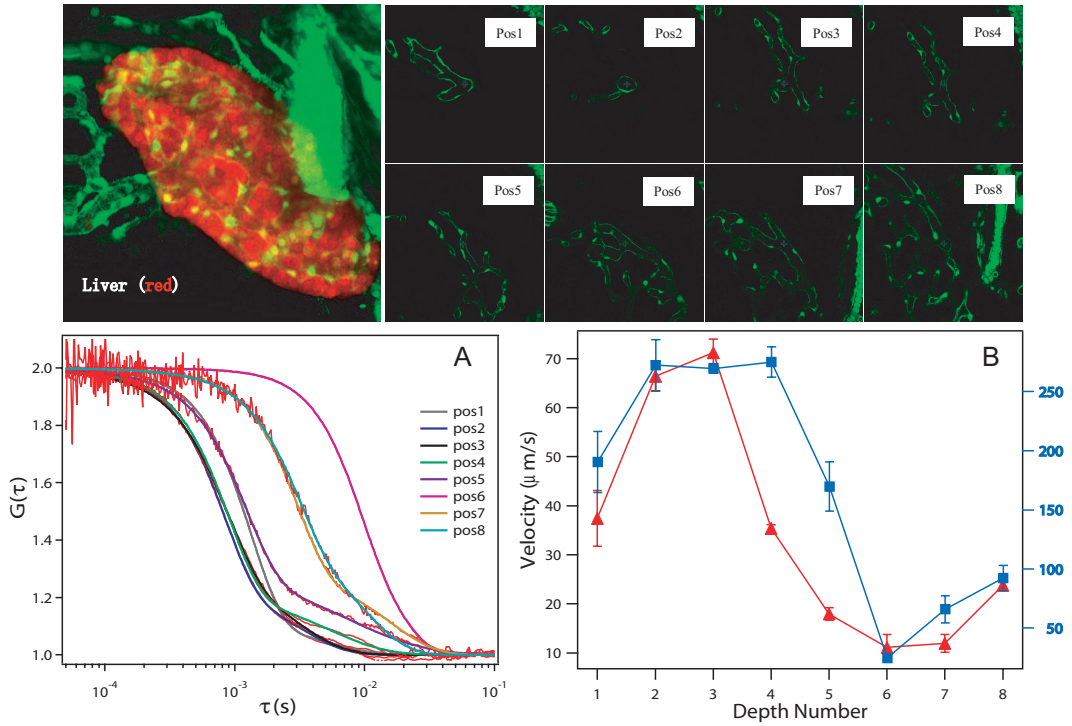

Figure 5.10: A) ACF curves and their fittings of blood flow in liver at 8 different depth positions (starting from 20μm to 100μm top from the liver surface cell layer); B) the corresponding systolic (blue) and diastolic (red) blood flow velocities calculated at the 8 positions.

5.2.3.3 Initiation of Blood Flow in Liver Revealed by FCS

Using the zebrafish transgenic line Tg(fli1:EGFP) it is possible to observe the growth morphology of first sinusoids in the developing liver. Although it is easier to identify the size increase of the sinusoids from the initial development time point up to 120 hpf, it is difficult to verify the exact time point the blood vessels develop the blood circulation inside the sinusoids. Therefore, FCS is applied for this purpose and can

provide flow measurements in liver sinusoids similar to those obtained in trunk vessels of zebrafish (chapter 4). This method allows the systolic and diastolic blood flow measurement in zebrafish liver sinusoids *in vivo* during development. Under the same experimental condition as described before, the blood flow was measured to exist in the trunk vessels at 55 hpf but it was absent in any sinusoids at different focal positions (from $0\mu m$ to $70\mu m$ top from the liver surface layer) at 55-65 hpf. At 72-75 hpf blood flow was measured to initialize in 3 of 7 points in the sinusoids of liver parenchyma located in dorso-lateral part of liver, the average velocity for systolic flow was 40.2 ± 12.7 $\mu m/s$, and that for diastolic flow was $7.2 \pm 2.4\,\mu m/s$. When the blood circulation started in the liver, sinusoidal mesh developed extremely fast and liver significantly increased in size during 84-120hpf. 3D confocal image visualization revealed a dense penetrating vascular network at 120hpf, and blood flow was detected in 8 of 10 measured points located at different confocal position (as deep as 70 μm) of both left and right liver lobes. The average velocity for systolic flow was $77.9 \pm 38.2\mu m/s$, and that for diastolic flow was $6.9 \pm 3.2\mu m/s$. Therefore, it suggests that at around 120hpf the liver becomes well vascularized and circulation is present in almost the entire liver (13). The results of blood flow measurement in sinusoids of zebrafish liver using FCS correlate with these of increasing size of sinusoids during 84-120 hpf and intensive expansion of organ during this time of liver growth. Confocal and histological study of liver vasculogenesis, together with FCS flow measurements which suggest the initiation of blood flow in liver sinusoids at around 72-75 hpf, suggests that liver vasculogenesis may be divided into three steps: the first is the contact of endothelial cells and hepatocytes at around 55-60 hpf; the second is the formation of first sinusoids at around 68-72 hpf; and the third, which starts at around 72 hpf, is the initiation of blood flow in first sinusoids and in the entire liver.

5.2.4 Conclusion

Taken together, the results show that FCS can be used to measure systolic and diastolic blood flow in the liver sinusoidal network during the liver development. Using a transgenic zebrafish line, the position of blood vessels was located within the fish body and also the developing liver. A spatial flow profile across the dorsal aorta in the trunk area was measured by FCS with high spatial resolution of 0.5 μm. Local blood flow changes within a single blood vessel, and the shear stress induced on the endothelial cells that may affect their growth, are therefore worth studying. The blood flow velocity was found to be dependent on the diameter and penetrating depth of sinusoids. The flow measurement by FCS in the study of zebrafish embryo showed that the blood circulation in sinusoids existed and become functional only after the formation of sinusoid vessel network. Furthermore, for both liver tissue engineering perfusion models and zebrafish embryo, there are some locations where 3D microfluidic flow exists. Line scan FCS in 2D has its own limitation to measure the 3D flow velocity vector. As discussed in chapter 4, line scan FCS can be extended to 3D flow measurements by using an additional scanner for the Z direction. The proposed method is discussed in details in the next chapter.

Chapter 6

Three Dimensional Microfluidic Flow Profile Measurement

6.1 Introduction

The measurement of microfluidic flow velocity is of great significance in the field of microchips and small blood vessels. The information obtained can be used to improve the performance of microfluidic chip system or collect physiological parameter from small animals for further experimental analysis. Currently there are several non-invasive optical methods developed for this purpose, including laser line scan velocimetry (20; 21), particle image velocimetry (PIV) (16), and fluorescence correlation spectroscopy (FCS) (23; 32). From the principles, most of these methods can be applied only to the situation when the flow axis is limited to a 2D plane. However, with the developed miniature fabrication techniques and the complicated biological organism, flows in microchannels or blood vessels are not limited to the 2D plane, but often extended in 3 dimensions. Therefore, it is pertinent to develop a non-invasive optical

method that can measure 3D microfluidic flow velocity vectors. Stereoscopic micro-PIV is one of the solutions for the measurement of three components of the velocity vector (135), it uses two cameras to capture PIV images at two different angles by a stereomicroscope. However, the spatial resolution is limited by a low N.A. stereo objective ($44 \times 44 \times 15\ \mu m^3$) used in the stereomicroscope, and it requires precise alignment of two focal planes through the objective in this case. The 'super-resolution' particle tracking velocimetry (PTV) is an alternative for 3D velocity measurement (136), but its low spatial resolution is still a disadvantage ($10 \times 10 \times 10\ \mu m^3$). In chapter 4, it has been demonstrated that line scan FCS has a higher spatial resolution of $0.5\ \mu m$ to resolve 2D flow velocity profiles. In this chapter, line scan FCS is extended to the measurement of 3D microfluidic flow velocity in both a microchannel and small blood vessel with spatial resolution of $0.5 \times 0.5 \times 0.5\ \mu m^3$ in 3D.

6.2 Theory

The principles of FCS for microfluidic flow and line scan FCS for 2D flow velocity have been discussed in chapter 2 and section 4.2 respectively. The laser line scan is performed in the XY plane only once as required for the measurement of a 2D flow velocity vector. However, to resolve a 3D velocity, two additional line scans have to be implemented, one in the same XY plane as the first line scan but perpendicular to the first line, and the other along the optical axis (Z direction). Simply, the three line scans are called x-scan, y-scan, and z-scan. Therefore, the three following velocity vector equations can be obtained, where V_n is the net flow, V_f is the microfluidic flow, and V_s is the line scan speed:

x-scan:

$$\overrightarrow{V_{nx}} = \overrightarrow{V_f} + \overrightarrow{V_{sx}} = \begin{pmatrix} V_{fx} + V_{sx} \\ V_{fy} \\ V_{fz} \end{pmatrix}$$

y-scan:

$$\overrightarrow{V_{ny}} = \overrightarrow{V_f} + \overrightarrow{V_{sy}} = \begin{pmatrix} V_{fx} \\ V_{fy} + V_{sy} \\ V_{fz} \end{pmatrix}$$

z-scan:

$$\overrightarrow{V_{nz}} = \overrightarrow{V_f} + \overrightarrow{V_{sz}} = \begin{pmatrix} V_{fx} \\ V_{fy} \\ V_{fz} + V_{sz} \end{pmatrix}$$

As is known, the net flow velocity vector is actually the combination of three velocity components. The mathematical equations regarding this relationship can be written as,

$$\begin{cases} V_{nx}^2 = (V_{fx} + V_{sx})^2 + V_{fy}^2 + V_{fz}^2 \\ V_{ny}^2 = V_{fx}^2 + (V_{fy} + V_{sy})^2 + V_{fz}^2 \\ V_{nz}^2 = V_{fx}^2 + V_{fy}^2 + (V_{fz} + V_{sz})^2 \end{cases} \tag{6.1}$$

In the list of three equations, the 3 unknowns of V_{fx}, V_{fy} and V_{fz} can be solved using the known values of V_{nx}, V_{ny}, V_{nz}, V_{sx}, V_{sy} and V_{sz}. During calibration the scan speeds V_{sx}, V_{sy} and V_{sz} can be obtained; the net flow velocities V_{nx}, V_{ny} and V_{nz} are measured using a one flow model (equation 4.2) described in chapter 4. Therefore, the angles of the flow velocity vector can be calculated based on the above known parameters. The schematic representation of a flow velocity vector is shown in figure 6.1. Here, two important angles of the flow vector are defined in the figure,

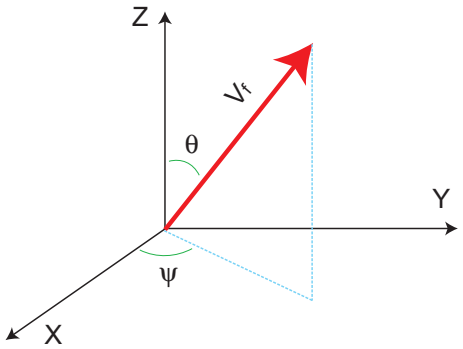

Figure 6.1: A 3D representation of flow velocity vector. Angle θ is the one formed between the flow vector and XY plane; angle ψ is the one between x axis and the projection of flow vector in XY plane.

$$\theta = \arcsin\left(\frac{V_{fz}}{V_f}\right) \tag{6.2}$$

$$\psi = \arctan\left(\frac{V_{fy}}{V_{fx}}\right) \tag{6.3}$$

6.3 Experimental Section

6.3.1 Z Piezo Scanner

The optical setup for FCM and XY line scan FCS has been described in details in section 3.2.2. In order to implement line scan in Z direction, an extra device with a piezo scanner (LISA NanoAutomation Actuator, P753.2CD, Physik Instrumente, Germany) is designed and mounted on the microscope mechanical stage (Figure 6.2). In the figure, the custom-made components of A, B and C are fixed on the microscope stage, while D, the sample mounting adapter, connects to the piezo drive scanner. In this design, when the piezo scanner vibrates vertically by applying a DC voltage, the sample

attached to the adapter is being scanned in Z direction at the same frequency as the scanner. Meanwhile, the mechanical stage and Z motor of the microscope are fixed at a position, and FCM performs point scan FCS at the desired position. Therefore, this is equivalent to line scan FCS in Z direction. A function generator (Fisher Scientific) is connected to the piezo actuator/scanner through a BNC cable. The frequency of sawtooth voltage wave applied to the scanner was set to 300 Hz, and the max voltage amplitude was set to 1.2 V which corresponded to a scan travel distance of 1.2 μm, the travel position of the scanner was linearly dependent on the applied DC voltage.

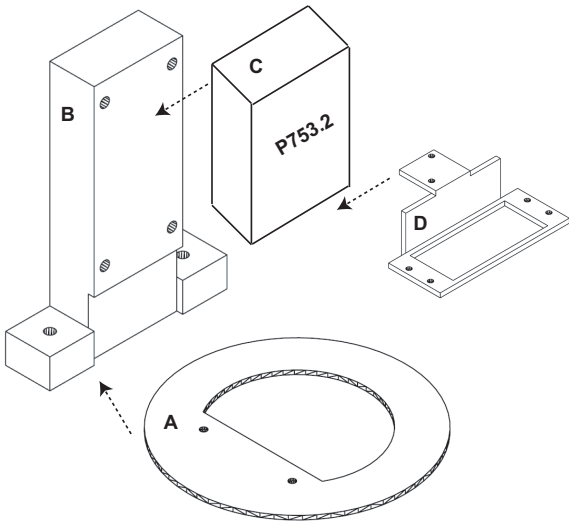

Figure 6.2: Schematic diagram of Z piezo scanner. A) customized microscope stage insert; B) support stand for the Z scanner; C) LISA NanoAutomation actuator (P753.2CD, Physik Instrumente); D) adapter for #1 coverslip (50×22 mm) with samples (either microchannel or mounted zebrafish embryo).

6.3.2 3D Microchannel

A PDMS microchannel was sealed on the glass coverslip, and its cross section was designed as a square of 100 μm side length. The fabrication process of PDMS mi-

crochannels and the setup of the microchannel perfusion system is described in section 4.3.2. For this work, the fabricated microchannel includes one inlet, one center channel, and one outlet (Figure 6.3). During the fabrication process, the inlet channel (Figure 6.3A) was placed at different angles in the XZ plane. In this case, it was 0° for the angle of θ when measured in the center channel (Figure 6.3B), 60° in the inlet and 90° in the outlet (Figure 6.3C). During the experiment, the center channel was manually placed at 45° for the angle ψ in order to minimize the measurement error as discussed in the section 4.4.2. Thus, a 3D microfluidic flow was generated when the dye solution (Atto 565) was perfused into the microchannel through the inlet.

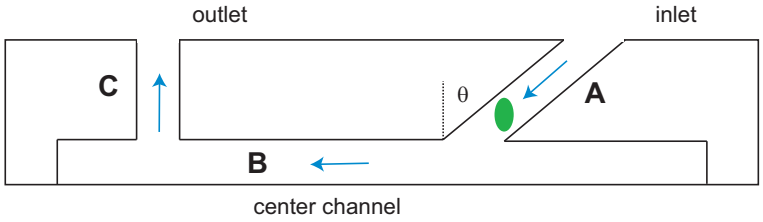

Figure 6.3: Schematic diagram representation of a PDMS microchannel structure including inlet, center channel and outlet. 3D microfluidic flow can be measured in the inlet, center channel or the outlet (green spot), namely at 60°, 90° and 0° for the angle of θ. The center channel is always placed at 45° for the angle of ψ.

6.3.3 Zebrafish Embryo

The maintenance of zebrafish was based on the protocols in the zebrafish book (115). Briefly, a pair of AB wild-type zebrafish was crossed and their embryos were collected the next morning. The embryos were then incubated in egg water ($60\mu g/ml$, Instant Ocean® Sea Salts (Aquarium Systems, Inc.)) at $28.5°C$ for the optimal development, and after 20 hpf (hours post fertilization) PTU (0.003% 1-phenyl-2-thiourea in 10% Hank's saline, Invitrogen, Singapore) was added to prevent pigmentation. Embryos

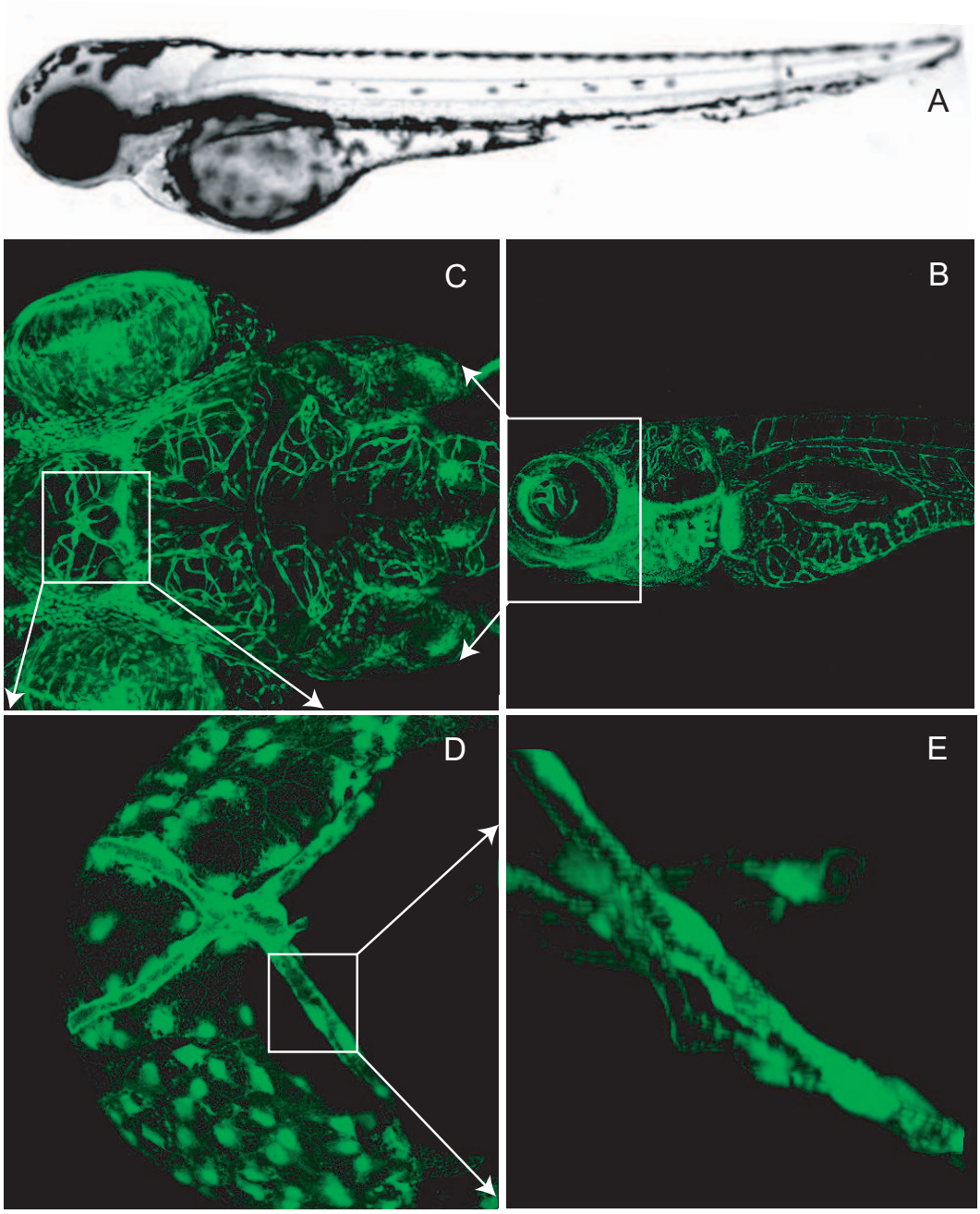

Figure 6.4: A) Overview of zebrafish embryo; B) Picture of GFP expressed in blood vessel endothelial cells; Zoom in from B (lateral view), C (dorsal view), D (dorsal view) to E (dorsal view) until a single blood vessel in 3D is identified.

were dechorionated at the time of 55 hours and then anaesthetized by Tricaine (ethyl m-aminoboenzoate, Sigma, Singapore). The treated embryos were mounted in 0.5% low melting temperature agarose (Invitrogen, Singapore) on a coverslip glass ($25 \times 75mm$) for the following measurements. The 3D organization of blood vessels in zebrafish embryos makes it a good model to study as 3D microfluidic flow in small animal blood vessels. Some of the small blood vessels in the embryo brain are naturally isolated from others, and are thus clearly visible. An overview of zebrafish embryo in bright field is shown in figure 6.4A (lateral view); all the blood vessels in the Fli line zebrafish embryo are expressed with GFP in endothelial cells (Figure 6.4B, lateral view). A region of interest is then identified in the embryo brain (Figure 6.4C, dorsal view) for 3D blood flow velocity measurement using line scan FCS. Furthermore, a single blood vessel organized in 3D (approx. $\theta = 45°$, $\psi = 45°$) is found using confocal LSM imaging technique (Figure 6.4D, dorsal view); a 3D projection from z-stack of the blood vessel is plotted (Figure 6.4E) and its orientation in 3D is observed.

6.4 Results and Discussions

6.4.1 Selective Scan Length in Z Direction

As discussed in section 4.3.1, the length of the scan line in X and Y directions can be reduced in order to improve the linear performance of scanner and additionally increase the spatial resolution of line scan FCS. In the X and Y direction, line scan FCS is implemented by the galvanometer scanning mirrors, the experiment of selective scan length is repeated in this case. The result of calculated ACF curves is shown in figure 6.5A, where the scan length was reduced from 2 μm, 1.5 μm, 1.0 μm to 0.5 μm.

The respective ACF curve is shifted to the left indicating the shorter dwelling time of molecules. The corresponding scan speeds from fitting data are shown in figure 6.5A inset. It is noted that the shorter the scan length, the faster the scan speed. The same principle and strategy from 2D line scan FCS applied to that in Z direction, which meant that the original photon counting data was recorded and the middle part of the line scan signal was selectively extracted and ACF curve was calculated. The original Z line scan length (travel distance) was 1.2 μm, it was selectively reduced down to 0.5 μm. As shown in figure 6.5B, the scan speed becomes faster when the selective length reduction algorithm was applied in order to shorten the scan length to 0.8 μm and 0.5 μm, which was represented by the left-shift of ACF curves and directly shown by the scan speed graph (Figure 6.5B inset).

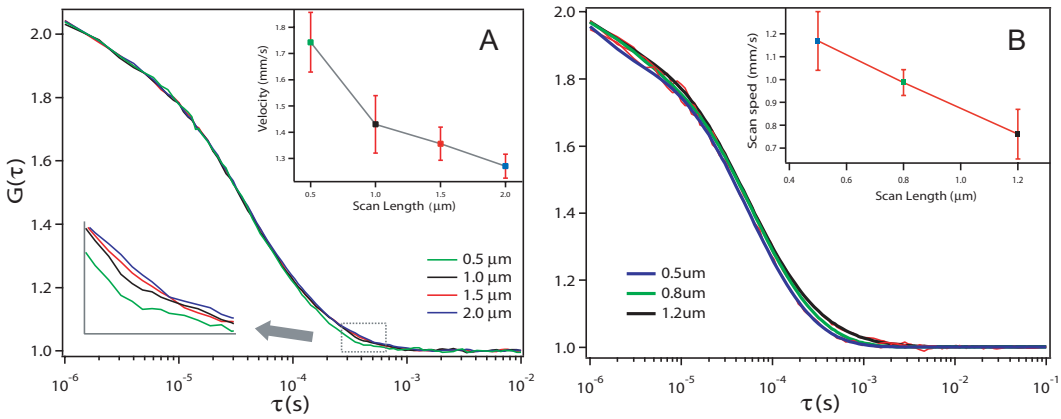

Figure 6.5: ACF curves calculated from extracted photon counting data and scan speed graph (inset) of XY scan (A) and Z scan (B) at different selective scan lengths.

6.4.2 3D Flow Angles in a Microchannel

The PDMS microchannel is a good model to study microfluidic flow because it is an optically transparent material and easy to manipulate for a variety of 3D microchannel

structures. Therefore, there have been a great number of applications of PDMS channels in the research field of miniaturized chips. For this work, a 3D microchannel was designed and perfused with Atto 565 solution (1 nM). Point FCS was first implemented to measure the absolute flow speed at a position in the microchannel (Figure 6.3, green spot), and line scan FCS was then performed at the same position in XY directions using the galvanometer scanning mirrors in the confocal LSM scan unit, and in Z direction using the piezo actuator scanner. The selective scan length reduction is additionally applied to line scan FCS in the XYZ directions to set the spatial resolution at the 3 axis to 0.5 μm. All ACF curves were fitted with the one-flow model (see equation 4.2). The calculated microfluidic flow velocities were used in equation 6.1. Thus the 3 components of flow velocity, V_{fx}, V_{fy} and V_{fz} were measured. The angles θ and ψ were then calculated using equation 6.2 and 6.3. The measurements were performed at different positions in one microchannel with inlet channel at 30° (Figure 6.3A, B and C) and the other microchannel with inlet channel at 60°. The result of 3D flow velocity angles is listed in table 6.1. As shown, the angles of ψ were measured as 46.5°, 54.7°, 39.4° and 51.1° which were close to the aligned channel angle of 45°. Considering the measurement and alignment errors, the line scan FCS can accurately measure the angle ψ for the 3D flow velocity vector with an error less than 10°. During the experiment, the x and y line scans are both at an angle of 45° respect to the flow axis, so the measurement error by line scan FCS is minimal. This is further demonstrated by the results of flow angle θ, which shows a large error (21.6°) at 0°, but smaller errors at 30°, 60° and 90° (3.6°, 5.7° and 12.4° respectively). The reason is that the Z scan line is parallel to the flow axis when the angle θ is 0°, the measurement error decreases when θ is close to 90°.

Table 6.1: Angles (θ and ψ) measured for 3D flow velocity vector compared to the aligned channel angles of inlet, center and outlet channels. (unit: degree)

Channel θ	0	30	60	90
Measured θ	21.6	26.4	54.3	77.6
Channel ψ	45	45	45	45
Measured ψ	46.5	54.7	39.4	51.1

6.4.3 3D Flow Angles in Blood Vessels of Zebrafish Embryo

The zebrafish embryo was mounted at dorsal view in agarose gel on a coverslip glass. After that, the coverslip was adapted to the z piezo scanner sitting on the microscopic mechanical stage. Using confocal LSM, a single blood vessel was identified in the brain of zebrafish embryo (Figure 6.4D and E). The orientation of the blood vessel was manually arranged at angles θ of 45° and ψ of 45°. Line scan FCS was performed in x and y direction using the galvanometer scan mirrors in slow scan mode with scan length of $3\mu m$, and Z direction using the stage piezo scanner at a frequency of 300 Hz with scan length of 1.2 μm. Furthermore, the spatial resolution of line scan FCS in XYZ directions was improved to 0.5 μm by the algorithm of selective scan length described previously. The result of selective scan length can be found in figure 6.5. The line scan speeds in XYZ directions were obtained during the system calibration (V_{sx} = V_{sy} = 1.60 mm/s, and V_{sz} = 0.93 mm/s), and all the ACF curves for blood flow coupled with line scan were fitted with the one-flow model (equation 4.2). From the fitting results, V_{nx}, V_{ny} and V_{nz} are measured as 1.59, 1.53 and 1.30 mm/s respectively. With the known parameters, the blood flow velocity in XYZ directions is calculated as V_{fx} = 0.88 mm/s, V_{fy} = 0.95 mm/s and V_{fz} = 1.06 mm/s using the equation 6.1, and the angles of θ and ψ were calculated as 43.1° and 39.3° respectively using the

equations 6.2 and 6.3. The result angles are quite close to the pre-aligned embryo orientation with small measurement errors. It demonstrates that line scan FCS can be extended to the Z direction for 3D flow velocity measurements in small animals. The spatial resolution of line scan FCS in 3D is kept to $0.5\mu m$, which is the same as that of 2D line scan FCS. Therefore, line scan FCS has a great potential applications in either tissue engineering or developmental biology as the two fields may require an accurate measurement of 3D microfluidic flow velocities so as to optimize or characterize the biological systems.

6.5 Conclusion

In this chapter, line scan FCS was extended to the third dimension to measure 3D microfluidic flow vectors with 3 line scans along the X, Y, and Z axes. The method and its accuracy were proven in both microchannels and zebrafish embryo brain blood vessels with 3D flow microstructures. With the development of selective scan length reduction, the spatial resolution of line scan FCS was improved to $0.5\mu m$ in all 3 directions. This is superior to all the other methods available for 3D microfluidic flow vector measurements. Due to its noninvasive property and successful demonstration of application in zebrafish embryo brain blood vessels, line scan FCS for 3D microfluidic flow velocity determination could assist in the system optimization of microelectromechanical systems (MEMS), microfluidic flow related tissue engineering, or blood flow physiological measurements in small animals.

Chapter 7

Conclusions and Outlook

7.1 Conclusions

The objective of this thesis is to develop a new extension technique of fluorescence correlation spectroscopy (FCS) for the measurement of 2D and 3D microfluidic flow velocity in both microchannels and small blood vessels. This was achieved by the proposed line scan FCS in X direction or XYZ directions performed on a custom-built fluorescence correlation microscope (FCM). The spatial resolution of line scan FCS at X, Y, and Z axes is about 0.5 μm, close to that of point FCS.

In chapter 1, the importance of microfluidic flow study was described and a comparison between different flow measurement techniques was shown. FCS was then highlighted as an alternative tool for microfluidic flow velocity measurement. FCS is well-known as an optical microcopy technique with single molecule sensitivity for the measurements like molecular interaction, protein binding, and solution concentrations. Additionally, FCS has been shown to measure microfluidic flow velocity in small structures using low concentration and small fluorescent probes. It is superior to

all the other methods like particle imaging velocimetry (PIV). Furthermore, the observation volume by FCS is less than 1 femtolitre, which makes the method suitable for applications which require high spatial resolution. In chapter 2, the basic principle of FCS was described and its common applications in biology were discussed. A typical FCS optical setup with confocal scheme was also presented. However, this point FCS is more suitable for solution measurements or other applications require no spatial information. In cell biology, to ensure the precise localization of FCS observation volume in the specimen, FCS is usually coupled with an imaging tool to position the observation volume accurately in the image area. Therefore, in chapter 3, FCS was combined with a confocal laser scanning microscope (CLSM), the positioning of FCS observation volume was guaranteed by the movement of the scan mirrors, this combination system is called FCM. The various applications of FCM were described in the chapter including single wavelength FCCS, single pinhole spatial FCCS, rotational diffusion by FCS, and two-photon excitation FCS and line scan FCS. With the FCM, in chapter 4, line scan FCS was demonstrated to measure 2D flow velocities in a microchannel and a small blood vessel in zebrafish embryos. The spatial resolution was improved by the selective scan length reduction algorithm from 3 μm to 0.5 μm. Since the galvanometer mirrors in CLSM are accessible for the control of focal volume in XY positions, it is possible to measure the microfluidic flow direction in the whole field of view. In chapter 5, line scan FCS in 2D is applied to liver tissue engineering and zebrafish developmental biology. The flow velocities of medium perfusion in the isolated liver organs, the perfused liver slices and the perfused cell-culture microchannels were measured by point FCS and their flow directions were characterized by line scan FCS. The dependency of blood flow velocity on vessels diameter and penetrating depth in the liver of zebrafish embryo was shown by FCS. Additionally, a parabolic

flow profile across a single blood vessel was obtained by the FCM. Furthermore, the initiation of blood circulation in the liver of zebrafish embryo was determined by point FCS flow measurements. However, line scan FCS for the above measurements was limited to a 2D flow velocity by either X or Y axis line scans. For microchannels and blood vessels, there are some situations when the microfluidic flow velocity is three dimensional. Thus, in chapter 6, line scan in Z direction was implemented on the FCM by using a piezo Z scanner mounted on the mechanical stage of microscope. When the piezo scanner with sample specimen vibrated in Z direction, the FCM was performing point FCS at a position. So relatively it is considered as line scan in Z axis. The feasibility and accuracy of line scan FCS in 3D was verified in a microchannel as well as a brain blood vessel in zebrafish embryos.

In conclusion, this thesis described a line scan FCS in XYZ axes for the measurement of 3D microfluidic flow velocity in microchannels, and extended its application in liver tissue engineering and zebrafish developmental biology. The method could have a significant impact in the research area of MEMS, microfluidic chips, small perfusion models and small animal embryos.

7.2 Outlook

Although it has high spatial resolution for the flow velocity measurements, line scan FCS is still limited at low temporal resolution due to its property of single focal volume. In order to map the flow velocities at several positions, sequential line scans have to be performed at the locations which consumes long time. However, according to the techniques available in the market, there could be two research directions which improve the capability of line scan FCS in biological applications.

As discussed in previous chapters, it is a clear trend that FCS goes in the direction that it will eventually merge with other imaging techniques. The image correlation spectroscopy (ICS) by pure CLSM is a very good example. However, the scan speed of commercial CLSMs is still limited to 100-1000 ms/frame, so it is possible to map the flow speeds in the whole field of view but limited to slow speeds. Therefore, the application of ICS in biology is typically constrained to slow-diffusing molecules or proteins. The situation is definitely worse for line scan FCS in a traditional confocal setup. In the market there are two optical techniques which could assist the application of line scan FCS. One is slit scan CLM such as Zeiss LSM5 LIVE, which scans a straight slit of light over the field. Theoretically it is feasible to scan the slit over a small distance at any position in the axis perpendicular to the slit, similar to scan single focus at any position in the field. In this case, the flow directions at all pixels along the slit are resolved; The other is multi-line scanning confocal, similar to the spinning disk confocal. Other than circular scanning the disk, the technique scans multi laser beams from the splitter. Theoretically it is possible to map the flow velocities in the pattern of laser beams by scanning them over a small distance. The difference between the two techniques is that slit scan confocal could map a line pattern of flow velocities, while multi-line scan confocal could map a laser beam pattern other than a straight line. Coupled with a piezo Z scanner, 3D flow velocities could be measured at multi positions simultaneously.

A drawback of FCM system is that the frame rate of traditional confocal systems is not fast enough to obtain the information from the whole field of view. Therefore, fast-speed CCD camera is an alternative to acheive this imaging capability. Electron-Multiply CCD cameras (EMCCD) are popular in single molecule imaging because of their high signal-to-noise ratio and high quantum efficiency. To measure the fast-

moving objects, a high-speed EMCCD camera is required to do FCS in the whole image area, compared with the slow-speed performance of ICS. EMCCD-FCS has been demonstrated in the scheme of single focus and TIRF illumnation (88; 91). Another possible scheme is spinning disk EMCCD-FCS which maintains the confocal property of biological images (90). Furthermore, it has been reported that EMCCD-FCS can be used to measure the direction of flow velocity in 2D by cross correlation of neighboring pixels (88). Although this method provides a solution for high temporal resolution of FCS to measure flow directions, it is still restricted to 2D measurements in principle without providing any information of flow velocity in 3D. As proposed and discussed in this thesis, line scan in Z direction is able to resolve the flow direction in 3D, which could be applicable in the scheme of EMCCD-FCS. The possible procedure could be that a configuration of EMCCD-FCS together with a Z piezo scanner enables fast image acquisition when doing Z scans. The obtained data set in this case contains flow information in XY and also Z axes. The correlation analysis can be performed between 3D neighboring pixels, which makes it possible to obtain the flow velocity in 3D. With the development of CCD and CMOS camera technique, it is foreseen in the near future that the camera can go to the frame rate of more than 1 million fps with sufficient quantum efficiency. Together with the fast piezo z-scan stage (e.g. ASI scientific) technology, a z-stack could be acquired within microsecond. CCD-FCS/CMOS-FCS is not far away from us with the assistance of other optical sectioning schemes such as confocal scan, spinning disk, and deconvolution algorithm.

Bibliography

[1] B. H. Weigl, R. L. Bardell, and C. R. Cabrera. "Lab-on-a-chip for drug development." *Adv. Drug Deliv. Rev.* **55**, 349–377 (2003). 1

[2] P. S. Dittrich and P. Schwille. "An integrated microfluidic system for reaction, high-sensitivity detection, and sorting of fluorescent cells and particles." *Anal. Chem.* **75**, 5767–5774 (2003). 0003-2700 Journal Article. 1

[3] M. Foquet, J. Korlach, W. Zipfel, W. W. Webb, and H. G. Craighead. "Dna fragment sizing by single molecule detection in submicrometer-sized closed fluidic channels." *Anal. Chem.* **74**, 1415–1422 (2002). 0003-2700 Journal Article. 1, 4

[4] M. U. Kopp, A. J. Mello, and A. Manz. "Chemical amplification: continuous-flow pcr on a chip." *Science* **280**, 1046 (1998). 1

[5] S. Kaihara, J. Borenstein, R. Koka, S. Lalan, E. R. Ochoa, M. Ravens, H. Pien, B. Cunningham, and J. P. Vacanti. "Silicon micromachining to tissue engineer branched vascular channels for liver fabrication." *Tissue Eng.* **6**, 105–117 (2000). 2

[6] M. J. Powers, K. Domansky, M. R. Kaazempur-Mofrad, A. Kalezi, A. Capitano, A. Upadhyaya, P. Kurzawski, K. E. Wack, D. B. Stolz, R. Kamm, and L. G. Griffith. "A microfabricated array bioreactor for perfused 3d liver culture." *Biotechnol. Bioeng.* **78**, 257–269 (2002). 0006-3592 (Print) Journal Article. 2

[7] Y.-C. Toh, S. Ng, Y. M. Khong, V. Samper, and H. Yu. "A configurable three-dimensional microenvironment in a microfluidic channel for primary hepatocyte culture." *Assay Drug Dev. Technol.* **3**, 169–176 (2005). 2

[8] Y.-C. Toh, C. Zhang, J. Zhang, Y. M. Khong, S. Chang, V. D. Samper, D. van Noort, D. W. Hutmacher, and H. Yu. "A novel 3d mammalian cell perfusion-culture system in microfluidic channels." *Lab Chip* **7**, 302–309 (2007). 2, 70, 71, 73

[9] A. M. Rollins, S. Yazdanfar, J. K. Barton, and J. A. Izatt. "Real-time in vivo color doppler optical coherence tomography." *J. Biomed. Opt.* **7**, 123–129 (2002). 2

[10] E. Nagel, T. Thouet, C. Klein, S. Schalla, A. Bornstedt, B. Schnackenburg, J. Hug, E. Wellnhofer, and E. Fleck. "Noninvasive determination of coronary blood flow velocity with cardiovascular magnetic resonance in patients after stent deployment." *Circulation* **107**, 1738–1743 (2003). 2

[11] M. L. Smith, D. S. Long, E. R. Damiano, and K. Ley. "Near-wall micro-piv reveals a hydrodynamically relevant endothelial surface layer in venules in vivo." *Biophys. J.* **85**, 637–645 (2003). 2

[12] J. Chen, P. Haffter, J. Odenthal, E. Vogelsang, M. Brand, F. va Eeden, M. Furutani-Seiki, M. Granato, C. Hammerschmidt, M. aand Heisenberg, Y. Jiang, D. Kane, R. Kelsh, M. Mullins, and C. Nusslein-Volhard. "Mutations affecting the cardiovascular system and other internal organs in zebrafish." *Development* **123**, 293–302 (1996). 2, 81

[13] S. Isogai, M. Horiguchi, and B. M. Weinstein. "The vascular anatomy of the developing zebrafish: an atlas of embryonic and early larval development." *Dev. Biol.* **230**, 278–301 (2001). 3, 63, 81, 88

[14] D. Stainier, W. B.M., D. H.W., Z. L.I., and F. M.C. "Cloche, an early acting zebrafish gene, is required by both the endothelial and hematopoietic lineages." *Development* **121**, 3141–3150 (1995). 3

[15] W. Liao, B. Bisgrove, H. Sawyer, B. Hug, B. Bell, K. Peters, D. Grunwald, and D. Stainier. "The zebrafish gene cloche acts upstream of a flk-1 homologue to regulate endothelial cell differentiation." *Development* **124**, 381–389 (1997). 3

[16] J. G. Santiago, S. T. Wereley, C. D. Meinhart, D. J. Beebe, and R. J. Adrian. "A particle image velocimetry system for microfluidics." *Exp. Fluids* **25**, 316–319 (1998). 3, 35, 63, 90

[17] H. Cheng, Q. Luo, S. Zeng, S. Chen, J. Cen, and H. Gong. "Modified laser speckle imaging method with improved spatial resolution." *J. Biomed. Opt.* **8**, 559–564 (2003). 3

[18] W. Wang, Y. Liu, G. J. Sonek, M. W. Berns, and R. A. Keller. "Optical trapping and fluorescence detection in laminar flow streams." *Appl. Phys. Lett.* **67**, 1057–1059 (1995). 3

[19] B. Manz, P. Stilbs, B. Jonsson, O. Sodeman, and P. T. Callaghan. "Nmr imaging of the time evolution of electroosmotic flow in a capillary." *J. Phys. Chem.* **99**, 11297–11301 (1995). 3

[20] E. A. V. Jones, M. H. Baron, S. E. Fraser, and M. E. Dickinson. "Measuring hemodynamic changes during mammalian development." *Am. J. Physiol. Heart Circ. Physiol.* **287**, H1561–H1569 (2004). 3, 82, 90

[21] M. H. Malone, N. Sciaky, L. Stalheim, K. M. Hahn, E. Linney, and G. L. Johnson. "Laser-scanning velocimetry: A confocal microscopy method for quantitative measurement of cardiovascular performance in zebrafish embryos and larvae." *BMC Biotechnology* **7**, 40 (2007). 3, 82, 90

[22] E. L. Elson and D. Magde. "Fluorescence correlation spectroscopy. i. conceptual basis and theory." *Biopolymers* **13**, 1–27 (1974). 4, 5, 48

[23] D. Magde, W. W. Webb, and E. L. Elson. "Fluorescence correlation spectroscopy. iii. uniform translation and laminar flow." *Biopolymers* **17**, 361–376 (1978). 4, 5, 90

[24] R. H. Köhler, P. Schwille, W. W. Webb, and M. R. Hanson. "Active protein transport through plastid tubules: velocity quantified by fluorescence correlation spectroscopy." *J. Cell. Sci.* **113 (Pt 22)**, 3921–3930 (2000). 4

[25] B. H. Kunst, A. Schots, and A. J. Visser. "Detection of flowing fluorescent particles in a microcapillary using fluorescence correlation spectroscopy." *Anal. Chem.* **74**, 5350–5357 (2002). 0003-2700 Journal Article. 4

[26] D. Magde, E. Elson, and W. W. Webb. "Thermodynamic fluctuations in a reacting system - measurement by fluorescence correlation spectroscopy." *Phys. Rev. Lett.* **29**, 705–708 (1972). 5

[27] H. Qian and E. L. Elson. "Analysis of confocal laser-microscope optics for 3-d fluorescence correlation spectroscopy." *Appl. Opt.* **30**, 1185–1195 (1991). 5, 8

[28] R. Rigler, Ü. Mets, J. Widengren, and P. Kask. "Fluorescence correlation spectroscopy with high count rate and low background: analysis of translational diffusion." *Eur. Biophys. J.* **22**, 169–175 (1993). 5, 8, 9, 48

[29] M. Eigen and R. Rigler. "Sorting single molecules: application to diagnostics and evolutionary biotechnology." *Proc. Natl. Acad. Sci. U S A* **91**, 5740–5747 (1994). 5

[30] M. Ehrenberg and R. Rigler. "Rotational brownian motion and fluorescence intensity fluctuations." *Chem. Phys.* **4**, 390–401 (1974). 5, 26

[31] M. Ehrenberg and R. Rigler. "Fluorescence correlation spectroscopy applied to rotational diffusion of macromolecules." *Q. Rev. Biophys.* **9**, 69–81 (1976). 5

[32] M. Gösch, H. Blom, J. Holm, T. Heino, and R. Rigler. "Hydrodynamic flow profiling in microchannel structures by single molecule fluorescence correlation spectroscopy." *Anal. Chem.* **72**, 3260–3265 (2000). 5, 35, 46, 90

[33] M. Kinjo and R. Rigler. "Ultrasensitive hybridization analysis using fluorescence correlation spectroscopy." *Nucleic Acids Res.* **23**, 1795–1799 (1995). 5

[34] U. Meseth, T. Wohland, R. Rigler, and H. Vogel. "Resolution of fluorescence correlation measurements." *Biophys. J.* **76**, 1619–1631 (1999). 5, 26, 57

[35] M. Börsch, P. Turina, C. Eggeling, J. Fries, C. Seidel, A. Labahn, and P. Graber. "Conformational changes of the h+-atpase from escherichia coli upon nucleotide binding detected by single molecule fluorescence." *FEBS Lett.* **437**, 251–4 (1998). 5

[36] P. F. Fahey and W. W. Webb. "Lateral diffusion in phospholipid bilayer membranes and multilamellar liquid crystals." *Biochemistry* **17**, 3046–3053 (1978). 5

[37] F. Delie, R. Gurny, and A. Zimmer. "Fluorescence correlation spectroscopy for the characterisation of drug delivery systems." *Biol. Chem.* **382**, 487–490 (2001). 6

[38] J. Donsmark, L. Jorgensen, S. Mollmann, S. Frokjaer, and C. Rischel. "Kinetics of insulin adsorption at the oil-water interface and diffusion properties of adsorbed layers monitored using fluorescence correlation spectroscopy." *Pharm. Res.* **23**, 148–155 (2006). 6

[39] J. P. Clamme, J. Azoulay, and Y. Mély. "Monitoring of the formation and dissociation of polyethylenimine/dna complexes by two photon fluorescence correlation spectroscopy." *Biophys. J.* **84**, 1960–1968 (2003). 6

[40] E. Dauty and A. S. Verkman. "Actin cytoskeleton as the principal determinant of size-dependent dna mobility in cytoplasm: a new barrier for non-viral gene delivery." *J. Biol. Chem.* **280**, 7823–7828 (2005). 6

[41] R. P. Kulkarni, D. D. Wu, M. E. Davis, and S. E. Fraser. "Quantitating intracellular transport of polyplexes by spatio-temporal image correlation spectroscopy." *Proc. Natl. Acad. Sci. U S A* **102**, 7523–7528 (2005). 6

[42] K. Remaut, B. Lucas, K. Braeckmans, N. N. Sanders, J. Demeester, and S. C. D. Smedt. "Delivery of phosphodiester oligonucleotides: can dotap/dope liposomes do the trick?" *Biochemistry* **45**, 1755–1764 (2006). 6

[43] P. W. Wiseman, F. Capani, J. A. Squier, and M. E. Martone. "Counting dendritic spines in brain tissue slices by image correlation spectroscopy analysis." *J. Microsc.* **205**, 177–186 (2002). 6

[44] G. Alexandrakis, E. B. Brown, R. T. Tong, T. D. McKee, R. B. Campbell, Y. Boucher, and R. K. Jain. "Two-photon fluorescence correlation microscopy reveals the two-phase nature of transport in tumors." *Nat. Med.* **10**, 203–207 (2004). 6

[45] S. A. Tatarkova, A. K. Verma, D. A. Berk, and C. J. Lloyd. "Quantitative fluorescence microscopy of macromolecules in gel and biological tissue." *Phys. Med. Biol.* **50**, 5759–5768 (2005). 6

[46] X. Pan, H. Yu, X. Shi, V. Korzh, and T. Wohland. "Characterization of flow direction in microchannels and zebrafish blood vessels by scanning fluorescence correlation spectroscopy." *J. Biomed. Opt.* **12**, 014034 (2007). 6, 7, 44

[47] P. Schwille, J. Korlach, and W. W. Webb. "Fluorescence correlation spectroscopy with single-molecule sensitivity on cell and model membranes." *Cytometry* **36**, 176–182 (1999). 6

[48] K. Bacia, D. Scherfeld, N. Kahya, and P. Schwille. "Fluorescence correlation spectroscopy relates rafts in model and native membranes." *Biophys. J.* **87**, 1034–1043 (2004). 6

[49] N. Kahya and P. Schwille. "Fluorescence correlation studies of lipid domains in model membranes." *Mol. Membr. Biol.* **23**, 29–39 (2006). 6

[50] P. Schwille, U. Haupts, S. Maiti, and W. W. Webb. "Molecular dynamics in living cells observed by fluorescence correlation spectroscopy with one- and two-photon excitation." *Biophys. J.* **77**, 2251–2265 (1999). 6, 20, 42

[51] P. Schwille. "Fluorescence correlation spectroscopy and its potential for intracellular applications." *Cell Biochem. Biophys.* **34**, 383–408 (2001). 6

[52] U. Haupts, S. Maiti, P. Schwille, and W. W. Webb. "Dynamics of fluorescence fluctuations in green fluorescent protein observed by fluorescence correlation spectroscopy." *Proc. Natl. Acad. Sci. U S A* **95**, 13573–13578 (1998). 6

[53] P. Schwille, S. Kummer, A. A. Heikal, W. E. Moerner, and W. W. Webb. "Fluorescence correlation spectroscopy reveals fast optical excitation-driven intramolecular dynamics of yellow fluorescent proteins." *Proc. Natl. Acad. Sci. USA* **97**, 151–156 (2000). 6

[54] Y. Chen, J. D. Müller, Q. Q. Ruan, and E. Gratton. "Molecular brightness characterization of egfp in vivo by fluorescence fluctuation spectroscopy." *Biophys. J.* **82**, 133–144 (2002). 6

[55] Z. Kam and R. Rigler. "Cross-correlation laser scattering." *Biophys. J.* **39**, 7–13 (1982). 6

[56] P. Tong, K. Q. Xia, and B. J. Ackerson. "Incoherent cross-correlation spectroscopy." *J. Chem. Phys.* **98**, 9256–9265 (1993). 6

[57] K. Q. Xia, Y. B. Xin, and P. Tong. "Dual-beam incoherent cross-correlation spectroscopy." *J. Opt. Soc. Am. A* **12**, 1571–1578 (1995). 6, 47

[58] P. Schwille, F. J. Meyer-Almes, and R. Rigler. "Dual-color fluorescence cross-correlation spectroscopy for multicomponent diffusional analysis in solution." *Biophys. J.* **72**, 1878–1886 (1997). 6, 26, 34

[59] L. C. Hwang and T. Wohland. "Dual-color fluorescence cross-correlation spectroscopy using single laser wavelength excitation." *ChemPhysChem* **5**, 549–551 (2004). 6, 24, 26, 34

[60] L. C. Hwang, M. Leutenegger, M. Gösch, T. Lasser, P. Rigler, W. Meier, and T. Wohland. "Prism-based multicolor fluorescence correlation spectrometer." *Opt. Lett.* **31**, 1310–1312 (2006). 6, 8, 24, 34

[61] M. Brinkmeier and R. Rigler. "Flow analysis by means of fluorescence correlation spectroscopy." *Exp. Techn. Phys.* **41**, 205–10 (1995). 6

[62] M. Brinkmeier, K. Doerre, J. Stephan, and M. Eigen. "Two-beam cross-correlation: a method to characterize transport phenomena in micrometer-sized structures." *Anal. Chem.* **71**, 609–616 (1999). 6, 8, 25, 26, 27, 35, 47

[63] W. Denk, J. H. Strickler, and W. W. Webb. "Two-photon laser scanning fluorescence microscopy." *Science* **248**, 73–76 (1990). 6, 19

[64] K. M. Berland, P. T. So, and E. Gratton. "Two-photon fluorescence correlation spectroscopy: method and application to the intracellular environment." *Biophys. J.* **68**, 694–701 (1995). 6, 34

[65] K. G. Heinze, A. Koltermann, and P. Schwille. "Simultaneous two-photon excitation of distinct labels for dual-color fluorescence crosscorrelation analysis." *Proc. Natl. Acad. Sci. U S A* **97**, 10377–10382 (2000). 6, 34

[66] K. G. Heinze, M. Jahnz, and P. Schwille. "Triple-color coincidence analysis: one step further in following higher order molecular complex formation." *Biophys. J.* **86**, 506–516 (2004). 0006-3495 Evaluation Studies Journal Article Validation Studies. 6

[67] N. L. Thompson and D. Axelrod. "Immunoglobulin surface-binding kinetics studied by total internal reflection with fluorescence correlation spectroscopy." *Biophys. J.* **43**, 103–114 (1983). 7, 8

[68] N. L. Thompson and B. L. Steele. "Total internal reflection with fluorescence correlation spectroscopy." *Nat. Protoc.* **2**, 878–890 (2007). 7

[69] N. O. Petersen. "Scanning fluorescence correlation spectroscopy. i. theory and simulation of aggregation measurements." *Biophys. J.* **49**, 809–815 (1986). 7

[70] N. O. Petersen, D. C. Johnson, and M. J. Schlesinger. "Scanning fluorescence correlation spectroscopy. ii. application to virus glycoprotein aggregation." *Biophys. J.* **49**, 817–820 (1986). 7, 47

[71] A. Amediek, E. Haustein, D. Scherfeld, and P. Schwille. "Scanning dual-color cross-correlation analysis for dynamic co-localization studies of immobile molecules." *Single Mol.* **3**, 201–210 (2002). 7

[72] Y. Xiao, V. Buschmann, and K. D. Weston. "Scanning fluorescence correlation spectroscopy: a tool for probing microsecond dynamics of surface-bound fluorescent species." *Anal. Chem.* **77**, 36–46 (2005). 7

[73] Q. Ruan, M. A. Cheng, M. Levi, E. Gratton, and W. W. Mantulin. "Spatial-temporal studies of membrane dynamics: scanning fluorescence correlation spectroscopy (sfcs)." *Biophys. J.* **87**, 1260–1267 (2004). 0006-3495 Evaluation Studies Journal Article. 7

[74] J. P. Skinner, Y. Chen, and J. D. Mller. "Position-sensitive scanning fluorescence correlation spectroscopy." *Biophys. J.* **89**, 1288–1301 (2005). 7, 47

[75] J. Ries and P. Schwille. "Studying slow membrane dynamics with continuous wave scanning fluorescence correlation spectroscopy." *Biophys. J.* **91**, 1915–1924 (2006). 7

[76] N. O. Petersen, P. L. Höddelius, P. W. Wiseman, O. Seger, and K. E. Magnusson. "Quantitation of membrane receptor distributions by image correlation spectroscopy: concept and application." *Biophys. J.* **65**, 1135–1146 (1993). 7

[77] P. W. Wiseman, J. A. Squier, M. H. Ellisman, and K. R. Wilson. "Two-photon image correlation spectroscopy and image cross-correlation spectroscopy." *J. Microsc.* **200**, 14–25 (2000). 7

[78] B. Hebert, S. Costantino, and P. W. Wiseman. "Spatiotemporal image correlation spectroscopy (stics) theory, verification, and application to protein velocity mapping in living cho cells." *Biophys. J.* **88**, 3601–3614 (2005). 7, 47

[79] M. A. Digman, C. M. Brown, P. Sengupta, P. W. Wiseman, A. R. Horwitz, and E. Gratton. "Measuring fast dynamics in solutions and cells with a laser scanning microscope." *Biophys. J.* **89**, 1317–1327 (2005). 7

[80] Y. Chen, J. D. Müller, P. T. So, and E. Gratton. "The photon counting histogram in fluorescence fluctuation spectroscopy." *Biophys. J.* **77**, 553–567 (1999). 7

[81] P. Kask, K. Palo, D. Ullmann, and K. Gall. "Fluorescence-intensity distribution analysis and its application in biomolecular detection technology." *Proc. Natl. Acad. Sci. U S A* **96**, 13756–13761 (1999). 7

[82] Y. Chen, M. Tekmen, L. Hillesheim, J. Skinner, B. Wu, and J. D. Müller. "Dual-color photon-counting histogram." *Biophys. J.* **88**, 2177–2192 (2005). 8

[83] M. J. Levene, J. Korlach, S. W. Turner, M. Foquet, H. G. Craighead, and W. W. Webb. "Zero-mode waveguides for single-molecule analysis at high concentrations." *Science* **299**, 682–686 (2003). 8

[84] L. Kastrup, H. Blom, C. Eggeling, and S. W. Hell. "Fluorescence fluctuation spectroscopy in subdiffraction focal volumes." *Phys. Rev. Lett.* **94**, 178104 (2005). 8

[85] H. Blom, M. Johansson, M. Gösch, T. Sigmundsson, J. Holm, S. Hard, and R. Rigler. "Parallel flow measurements in microstructures by use of a multifocal 4 x 1 diffractive optical fan-out element." *Appl. Opt.* **41**, 6614–6620 (2002). 0003-6935 Journal Article. 8

[86] M. Burkhardt, K. G. Heinze, and P. Schwille. "Four-color fluorescence correlation spectroscopy realized in a grating-based detection platform." *Opt. Lett.* **30**, 2266–2268 (2005). 8

[87] M. Gösch, A. Serov, T. Anhut, T. Lasser, A. Rochas, P.-A. Besse, R. S. Popovic, H. Blom, and R. Rigler. "Parallel single molecule detection with a fully integrated single-photon 2x2 cmos detector array." *J. Biomed. Opt.* **9**, 913–921 (2004). 8

[88] B. Kannan, J. Y. Har, P. Liu, I. Maruyama, J. L. Ding, and T. Wohland. "Electron multiplying charge-coupled device camera based fluorescence correlation spectroscopy." *Anal. Chem.* **78**, 3444–3451 (2006). 9, 106

[89] M. Burkhardt and P. Schwille. "Electron multiplying ccd based detection for spatially resolved fluorescence correlation spectroscopy." *Opt. Express* **14**, 5013–5020 (2006). 9

[90] D. R. Sisan, R. Arevalo, C. Graves, R. McAllister, and J. S. Urbach. "Spatially resolved fluorescence correlation spectroscopy using a spinning disk confocal microscope." *Biophys. J.* **91**, 4241–4252 (2006). 9, 106

[91] B. Kannan, L. Guo, T. Sudhaharan, S. Ahmed, I. Maruyama, and T. Wohland. "Spatially resolved total internal reflection fluorescence correlation microscopy using an electron multiplying charge-coupled device camera." *Anal. Chem.* **79**, 4463–4470 (2007). 9, 106

[92] J. Widengren, Ü. Mets, and R. Rigler. "Fluorescence correlation spectroscopy of triplet states in solution: a theoretical and experimental study." *J. Phys. Chem.* **99**, 13368–13379 (1995). 16, 48

[93] B. R. Terry, E. K. Matthews, and J. Haseloff. "Molecular characterization of recombinant green fluorescent protein by fluorescence correlation microscopy." *Biochem. Biophys. Res. Commun.* **217**, 21–27 (1995). 23

[94] R. Brock and T. M. Jovin. "Fluorescence correlation microscopy (fcm) - fluorescence correlation spectroscopy (fcs) taken into the cell." *Cell. Mol. Biol.* **44**, 847–856 (1998). 23

[95] T. Jankowski and R. Janka. "Confocor 2 – the second generation of fluorescence correlation microscopes." *In* E. L. Elson and R. Rigler, eds., "Fluorescence correlation spectroscopy. theory and applications," pages 331–345. Springer, Berlin (2001). 24

[96] S. K. Kaushalya, J. Balaji, K. Garai, and S. Maiti. "Fluorescence correlation microscopy with real-time alignment readout." *Appl. Opt.* **44**, 3262–3265 (2005). 24

[97] M. Wachsmuth, T. Weidemann, G. Müller, U. W. Hoffmann-Rohrer, T. A. Knoch, W. Waldeck, and J. Langowski. "Analyzing intracellular binding and diffusion with continuous fluorescence photobleaching." *Biophys. J.* **84**, 3353–3363 (2003). 24

[98] J. Widengren, Ü. Mets, and R. Rigler. "Photodynamic properties of green fluorescent proteins investigated by fluorescence correlation spectroscopy." *Chem. Phys.* **250**, 171–186 (1999). 24

[99] O. Krichevsky and G. Bonnet. "Fluorescence correlation spectroscopy: the technique and its applications." *Rep. Prog. Phys.* **65**, 251–297 (2002). 24

[100] G. Chirico and M. Gardella. "Photon cross-correlation spectroscopy to 10-ns resolution." *Appl. Opt.* **38**, 2059–2067 (1999). 24

[101] P. Kask, P. Piksarv, M. Pooga, Ü. Mets, and E. Lippmaa. "Separation of the rotational contribution in fluorescence correlation experiments." *Biophys. J.* **55**, 213–220 (1989). 26

[102] J. P. Chapple, A. J. Hardcastle, C. Grayson, K. R. Willison, and M. E. Cheetham. "Delineation of the plasma membrane targeting domain of the x-linked retinitis pigmentosa protein rp2." *Invest. Ophthalmol. Vis. Sci.* **43**, 2015–2020 (2002). 30

[103] P. Liu, T. Sudhaharan, R. M. L. Koh, L. C. Hwang, S. Ahmed, I. N. Maruyama, and T. Wohland. "Investigation of the dimerization of proteins from the epidermal growth factor receptor family by single wavelength fluorescence cross-correlation spectroscopy." *Biophys. J.* **93**, 684–698 (2007). 31, 34

[104] T. Kogure, S. Karasawa, T. Araki, K. Saito, M. Kinjo, and A. Miyawaki. "A fluorescent variant of a protein from the stony coral montipora facilitates dual-color single-laser fluorescence cross-correlation spectroscopy." *Nat. Biotechnol.* **24**, 577–581 (2006). 34

[105] P. F. Lenne, D. Colombo, H. Giovannini, and H. Rigneault. "Flow profiles and directionality in microcapillaries measured by fluorescence correlation spectroscopy." *Single Mol.* **3**, 194–200 (2002). 35, 46

[106] R. Jaffiol, Y. Blancquaert, A. Delon, and J. Derouard. "Spatial fluorescence cross-correlation spectroscopy." *Appl. Opt.* **45**, 1225–1235 (2006). 37

[107] P. S. Dittrich and P. Schwille. "Spatial two-photon fluorescence cross-correlation spectroscopy for controlling molecular transport in microfluidic structures." *Anal. Chem.* **74**, 4472–4479 (2002). 38, 42, 47

[108] S. Milon, R. Hovius, H. Vogel, and T. Wohland. "Factors influencing fluorescence correlation spectroscopy measurements on membranes: simulations and experiments." *Chem. Phys.* **288**, 171–186 (2003). 38, 40

[109] A. Benda, M. Benes, V. Marecek, A. Lhotsky, W. Hermens, and M. Hof. "How to determine diffusion coefficients in planar phospholipid systems by confocal fluorescence correlation spectroscopy." *Langmuir* **19**, 4120–4126 (2003). 38

[110] V. V. Skakun, M. A. Hink, A. V. Digris, R. Engel, E. G. Novikov, V. V. Apanasovich, and A. J. W. G. Visser. "Global analysis of fluorescence fluctuation data." *Eur. Biophys. J.* **34**, 323–334 (2005). 45

[111] R. Rao, R. Langoju, M. Gösch, P. Rigler, A. Serov, and T. Lasser. "Stochastic approach to data analysis in fluorescence correlation spectroscopy." *J. Phys. Chem. A* **110**, 10674–10682 (2006). 45

[112] K. K. Kuricheti, V. Buschmann, and K. D. Weston. "Application of fluorescence correlation spectroscopy for velocity imaging in microfluidic devices." *Appl. Spectrosc.* **58**, 1180–1186 (2004). 0003-7028 Journal Article. 46

[113] D. E. Koppel, F. Morgan, A. E. Cowan, and J. H. Carson. "Scanning concentration correlation spectroscopy using the confocal laser microscope." *Biophys. J.* **66**, 502–507 (1994). 47

[114] K. M. Berland, P. T. So, Y. Chen, W. W. Mantulin, and E. Gratton. "Scanning two-photon fluctuation correlation spectroscopy: particle counting measurements for detection of molecular aggregation." *Biophys. J.* **71**, 410–420 (1996). 47

[115] M. Westerfield. *The zebrafish book. A guide for the laboratory use of zebrafish (Danio rerio)*. 4th edition. University of Oregon Press (2000). 54, 83, 95

[116] D. E. Koppel. "Statistical accuracy in fluorescence correlation spectroscopy." *Phys. Rev. A* **10**, 1938–1945 (1974). 55

[117] T. Wohland, R. Rigler, and H. Vogel. "The standard deviation in fluorescence correlation spectroscopy." *Biophys. J.* **80**, 2987–2999 (2001). 0006-3495 Journal Article. 55

[118] R. McCuskey. "Hepatic microcirculation as a major determinant of hepatic function." *In* T. Kamada, ed., "Tissue perfusion and organ function: ischemia/reperfusion injury," Elsevier, New York (1996). 67

[119] J. Campra. "The hepatic circulation." *In* I. MA, ed., "The Liver: biology and pathobiology," Raven Press, New York (1988). 68

[120] K. Messmer and M. Menger. "Liver microcirculation and hepatobiliary function." *In* "11th Bodensee Symposium on Microcirculation," Bad Schachen (1992). 68

[121] A. LeBouton, ed. *Fat-storing cells in Molecular and cell biology of the liver*. CRC Press (1993). 68

[122] R. McCuskey. "Morphological mechanisms for regulating blood flow through hepatic sinusoids." *Liver* **20**, 3–7 (2000). 68

[123] F. Braet. "Liver sinusoidal endothelial cell modulation upon resection and shear stress in vitro." *Comp. Hepatol.* **3**, 7 (2004). 69

[124] J. Schoen. "Shear stressinduced nitric oxide release triggers the liver regeneration cascade." *Nitric Oxide* **5**, 453–464 (2001). 69

[125] M. Ross. "Spatiotemporal expression of angiogenesis growth factor receptors during the evascularization of regenerating rat liver." *Hepatology* **34**, 1135–1148 (2001). 69

[126] A. Tilles. "Effects of oxygenation and flow on the viability and function of rat hepatocytes cocultured in a microchannel flat-plate bioreactor." *Biotechnol. Bioeng.* **73**, 379–389 (2001). 69

[127] M. Bessems, N. A. 't Hart, R. Tolba, B. M. Doorschodt, H. G. D. Leuvenink, R. J. Ploeg, T. Minor, and T. M. van Gulik. "The isolated perfused rat liver: standardization of a time-honoured model." *Lab Anim* **40**, 236–246 (2006). 69

[128] P. Olinga, K. Groen, I. H. Hof, R. D. Kanter, H. J. Koster, W. R. Leeman, A. A. Rutten, K. V. Twillert, and G. M. Groothuis. "Comparison of five incubation systems for rat liver slices using functional and viability parameters." *J Pharmacol Toxicol Methods* **38**, 59–69 (1997). 70

[129] Y. M. Khong, J. Zhang, S. Zhou, C. Cheung, K. Doberstein, V. Samper, and H. Yu. "Novel intra-tissue perfusion system for culturing thick liver tissue." *Tissue Eng.* **13**, 2345–2356 (2007). 70, 72

[130] P. S. Dittrich and A. Manz. "Lab-on-a-chip: microfluidics in drug discovery." *Nat Rev Drug Discov* **5**, 210–218 (2006). 70

[131] E. N. Olson and D. Srivastava. "Molecular pathways controlling heart development." *Science* **272**, 671–676 (1996). 82

[132] L. Gan, M. Miocic, R. Doroudi, L. Selin-Sjgren, and S. Jern. "Distinct regulation of vascular endothelial growth factor in intact human conduit vessels exposed to laminar fluid shear stress and pressure." *Biochem Biophys Res Commun* **272**, 490–496 (2000). 82

[133] J. R. Hove, R. W. Kster, A. S. Forouhar, G. Acevedo-Bolton, S. E. Fraser, and M. Gharib. "Intracardiac fluid forces are an essential epigenetic factor for embryonic cardiogenesis." *Nature* **421**, 172–177 (2003). 82

[134] N. D. Lawson and B. M. Weinstein. "In vivo imaging of embryonic vascular development using transgenic zebrafish." *Dev. Biol.* **248**, 307–318 (2002). 84

[135] R. Lindken, J. Westerweel, and B. Wieneke. "Stereoscopic micro particle image velocimetry." *Exp. Fluids* **41**, 161–171 (2006). 91

[136] M. R. Bown, J. M. MacInnes, R. W. K. Allen, and W. B. J. Zimmerman. "Three-dimensional, three-component velocity measurements using stereoscopic micro-piv and ptv." *Meas. Sci. Technol.* **17**, 2175–2185 (2006). 91

Appendix A

Appendix: Technical Drawings of FCM Components

As described in chapter 3, the FCM was built on a modified commercial CLSM (FV300, Olympus). This system has two internal fluorescence channels using PMTs, the color separation is realized by a dichroic mirror mounted on a slider (Figure A.1). Due to limited space in the scan unit and the complexity of modification work, an alternative configuration is proposed to direct the fluorescence signal after the pinhole to the cover of scan unit, where the APDs are mounted for FCS detection (Figure A.2). Therefore, the dichroic mirror holder has to be modified to have such a position with a fully reflective mirror to direct the light towards the scan unit cover (Figure A.4). The modified cover thus has an opening at the respective position in order to mount the detection parts (Figure A.3. In the case of FCCS, a second dichroic mirror is used to separate the emission fluorescence signal after the pinhole, and a dichroic holder is specially designed for this purpose with a changeable dichroic mirror holder inset (Figure A.5. The last custom-built piece is a detector holder used to mount the APD,

which includes a narrow slot for a changeable emission filter mount (Figure A.6).

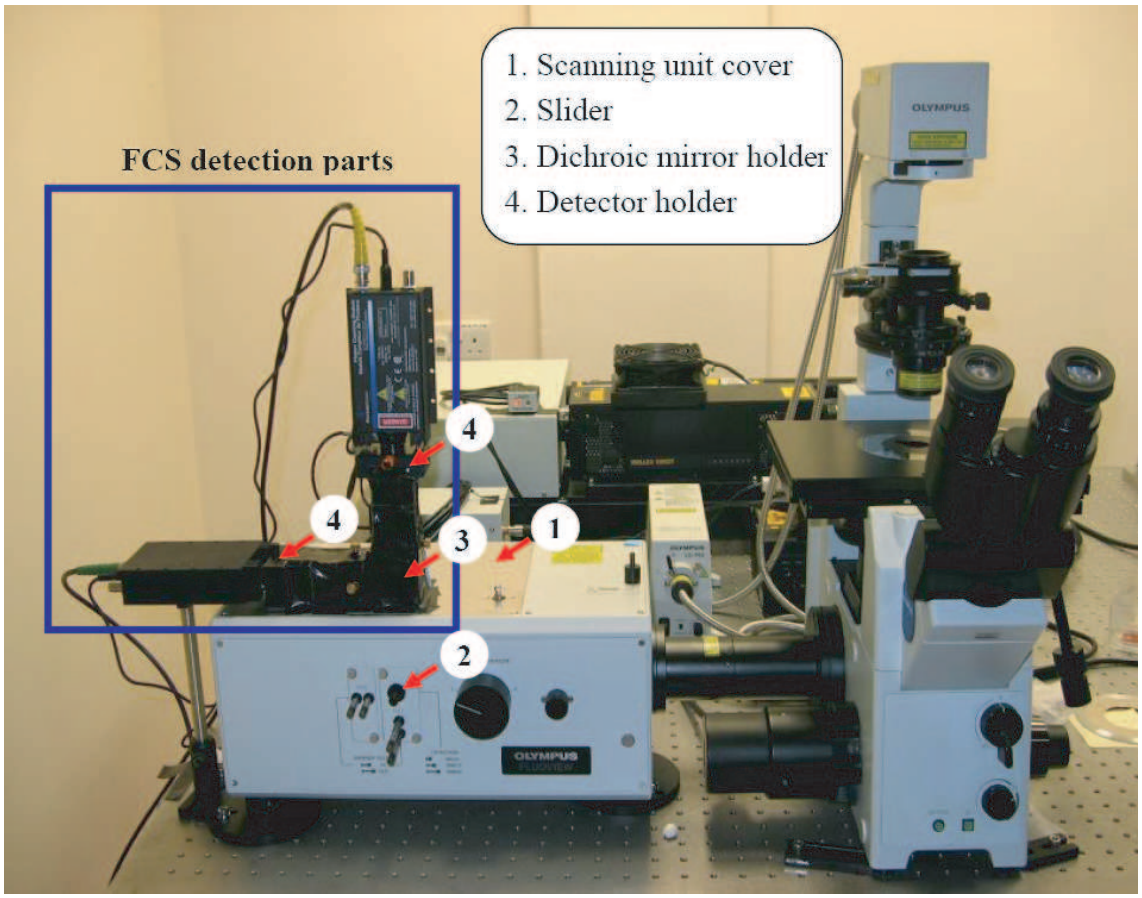

Figure A.1: Picture of custom-built FCM system

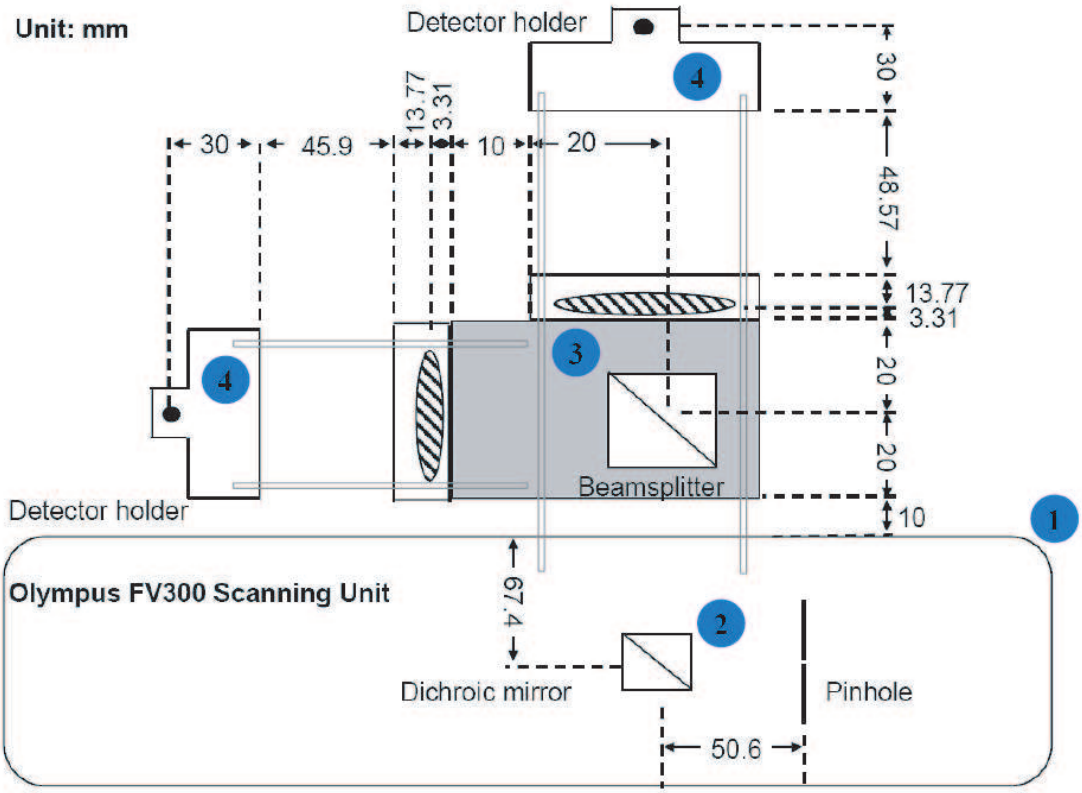

Figure A.2: Mounting distance of FCM components. 1) Scan unit cover; 2) Mirror slider; 3) Dichroic mirror holder; 4) Detector holder

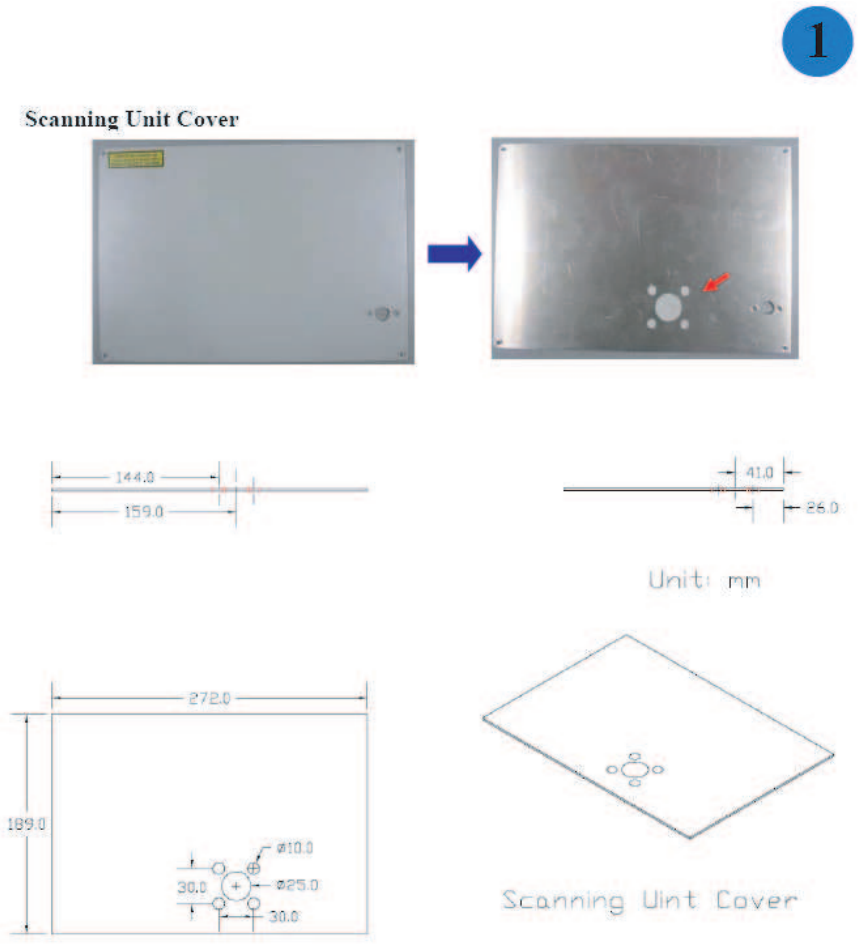

Figure A.3: Technical drawing of modified scan unit cover

Figure A.4: Comparison of original and modified mirror slider

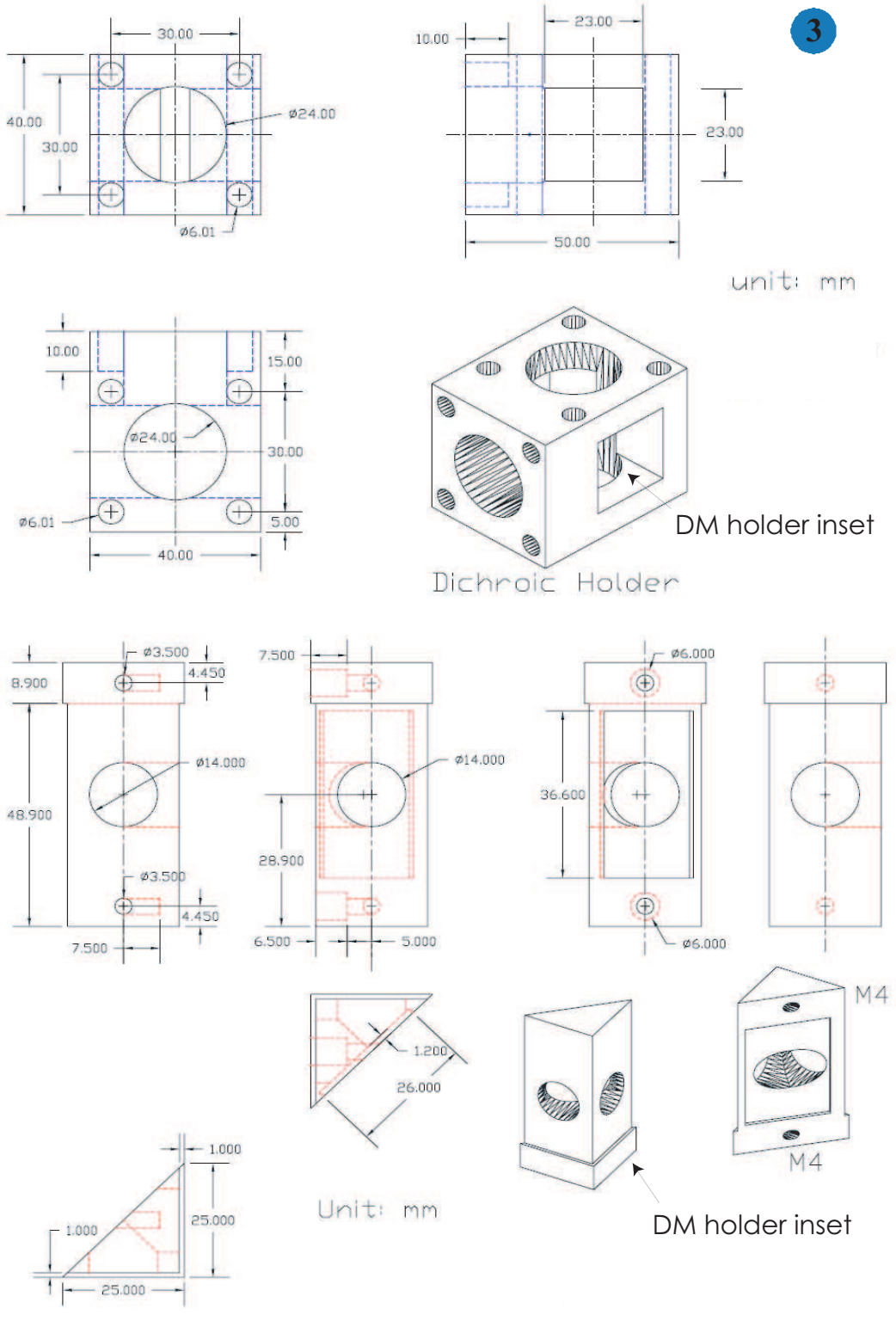

Figure A.5: Technical drawing of dichroic mirror holder and its inset

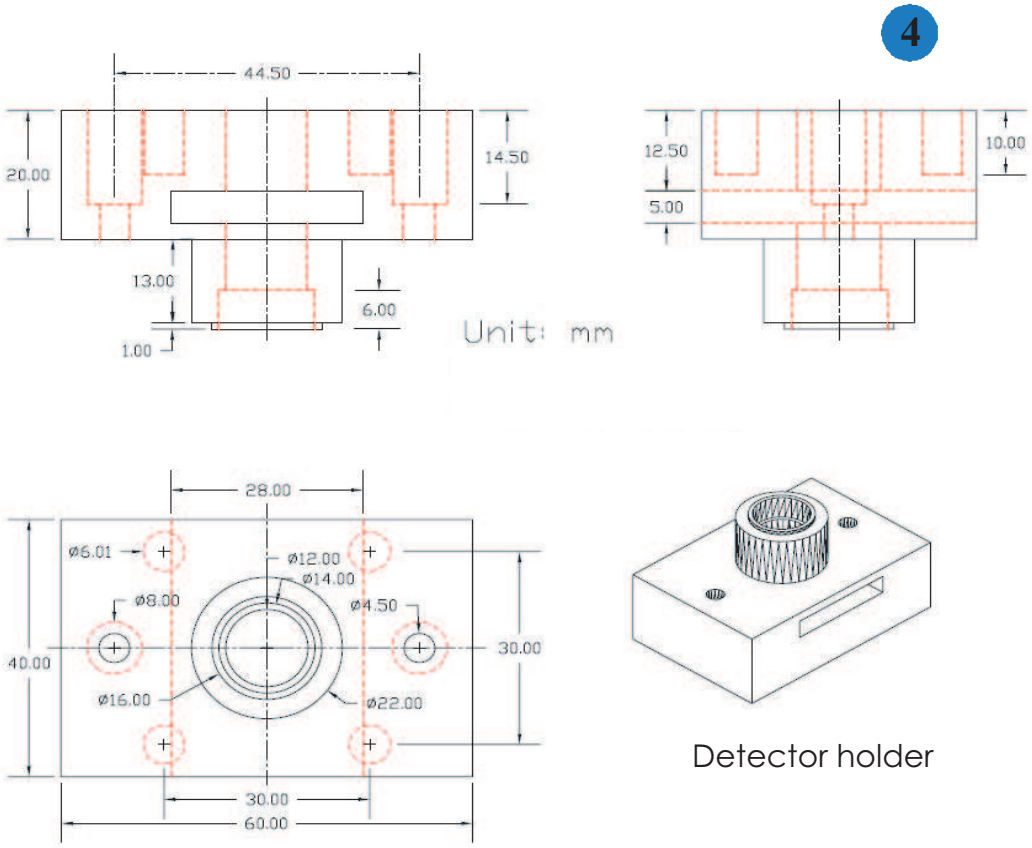

Figure A.6: Technical drawing of detector holder

Appendix B

Appendix: Programming Codes for Selective Scan Length Reduction

B.1 Igor Pro

B.1.1 Selective Length Reduction

```
Function CutACF(twave,startpnt,nameseq,scanperiod,backwardcut,cutlength)
    Wave twave
    Variable startpnt
    String nameseq
    Variable scanperiod
    Variable backwardcut
    Variable CutLength

    Variable i, j, k, cutindex=0, breakpnt=0
    String nwave = NameOfWave(twave)
    Variable npnts = numpnts(twave)
    String cutwname = nameseq + nwave
    Variable cutwnpnts = floor(twave(npnts-1)/scanperiod)

    Make/O/D/N=(npnts) $cutwname
    Wave CutWave = $cutwname
    CutWave = 0

    Duplicate/O twave, diff_twave
```

```
    diff_twave = diff_twave(p+1) - diff_twave(p)

    for (j=0; j<(cutwnpnts+1); j+=1)
        for (i=breakpnt; i<npnts; i+=1)
            if (twave(i) > (startpnt+ j*scanperiod+ backwardcut) )
                if (twave(i) < (startpnt+ j*scanperiod+ backwardcut
                    + CutLength))
                    CutWave[cutindex] = diff_twave(i)
                    cutindex+=1
                else
                    breakpnt = i
                    break;
                endif
            endif
        endfor
    endfor

    for (i=(npnts-1); i>0; i-=1)
        if (CutWave(i)!=0)
            break
        endif
    endfor
    Redimension/N=(i+1) CutWave

    Variable cutnpnts=numpnts(CutWave)
    for (i=1; i<cutnpnts; i+=1)
        CutWave[i] = CutWave[i] + CutWave[i-1]
    endfor

    KillWaves diff_twave
End
```

B.1.2 ACF Calculation from Raw Data

```
Function CalculateACF(twave, BinTime)
    WAVE twave
    Variable BinTime

    Variable k, i, v, npts, timestep, atmp, itmp1, itmp2, windex
    String waven = "acf_" + NameOfWave(twave)
    String lagtime = "lagT_" + NameOfWave(twave)
    npts=numpnts(twave)
    windex=0
    timestep=BinTime

    Make/O/D/N=144 wacftot=0
    Make/O/D/N=1 twave2
    Make/O/D/N=144 $lagtime
    Wave wlagtime = $lagtime
```

```
i=1
do
    wlagtime[i] = i*timestep
    i=i+1
while(i<=8)
i=1
do
    k=1
    do
        wlagtime[i*8+k] = (timestep*2^(i-1)*k+8*timestep
        +(2^i-2)*4*timestep)
        k=k+1
    while(k<=8)
    i=i+1
while(i<=17)

k=0
do
    i=0
    atmp=0
    itmp1=0
    itmp2=0
    do
        atmp=atmp+twave[i]*twave[i+k]
        itmp1=itmp1+twave[i]
        itmp2=itmp2+twave[i+k]
        i=i+1
    while(i<(npts-k))
    wacftot[windex]=atmp/(itmp1*itmp2)*(npts-k)
    windex=windex+1
    k=k+1
while(k<=15)

v=1
do
    if(v==1)
        Make/O/D/N=(npts) twave3=twave
    else
        Make/O/D/N=(npts) twave3=twave2
    endif
    npts=floor(npts/2)
    Make/O/D/N=(npts) twave2=twave3(2*p)+twave3(2*p+1)
    k=0

    do
        i=0
        atmp=0
        itmp1=0
```

```
            itmp2=0

            do
                atmp=atmp+twave2[i]*twave2[i+k+8]
                itmp1=itmp1+twave2[i]
                itmp2=itmp2+twave2[i+k+8]
                i=i+1
            while(i<(npts-k-8))

            wacftot[windex]=atmp/(itmp1*itmp2)*(npts-k-8)
            windex=windex+1
            k=k+1
        while(k<8)
        v=v+1
    while(v<=16)

    Make/O/D/N=(numpnts(wacftot)) $waven=wacftot
    KillWaves/Z twave2,twave3, wacftot
    KillWaves twave
End
```